STUDIES OF THE MICROWAVE INSTABILITY IN THE SMALL ISOCHRONOUS RING

By

Yingjie Li

A DISSERTATION

Submitted to
Michigan State University
in partial fulfillment of the requirements
for the degree of

Physics—Doctor of Philosophy

2015

ABSTRACT

STUDIES OF THE MICROWAVE INSTABILITY IN THE SMALL ISOCHRONOUS RING

By

Yingjie Li

This dissertation is devoted to deepening our knowledge and understanding of the hidden physics regarding the microwave instability of the space-charge dominated beams in the small isochronous ring, which was observed in our previous numerical and experimental studies.

The dissertation attempts to provide a further exploration and more accurate description of the microwave instability by focusing on the following topics:

(a) Derivations of the full-spectrum longitudinal space charge (LSC) impedance formula, which reflects the realistic configurations of the beam-chamber system more closely than the existing ones.

(b) Landau damping effect. A two-dimensional (2D) dispersion relation is derived in the dissertation, by which the microwave instability growth rates of a coasting beam with any energy spread and emittance in the isochronous regime can be predicted theoretically.

(c) Evolution of the beam profiles in the nonlinear regime of the microwave instability. For this purpose, various numerical, experimental and theoretical approaches have been employed in the research, including the simulation and measurement of the energy spread evolution, simulated corotation of the two-macroparticle and

two-bunch models together with their comparisons with the theoretical predictions.

The simulations, experiments and theoretical predictions on the above three topics all reach good agreements.

First, I would like to dedicate this doctoral dissertation to **my parents**. Your eager anticipation, lasting encouragements, selfless love and dedication without reservation were crucial for me to overcome the difficulties I met both in my academic study and daily life overseas. Without your careful nurturing and inculcation from the beginning of my life, it would have been impossible for me to finish this dissertation. Second, I would like to say a Big Thank You to the following people: **my elder brother**, **sister-in-law** and **cousin** for their constant support, encouragement, and generous financial help, as well as taking good care of my mother and my niece.

ACKNOWLEDGEMENTS

My gratitude to the people who helped my graduate study at MSU is beyond words.

First of all, I would like to express my sincere thankfulness to my thesis advisor Professor **Felix Marti**, who has provided great guidance on my research and trained me from a rookie in Beam Physics to grow towards a beam scientist. I really appreciate his patience and tolerance on my 'slow growth rate'. His perspective insight, prudence and strictness in the research work impressed me greatly. Without his long-term academic supervision and support, I would not have been able to finish this dissertation. I am particularly grateful to his constant and timely guidance even if his health condition was sometimes not very well.

I would like to convey my special gratitude to my co-advisor, Professor **Thomas Wangler** (LANL). It was a great honor for me to have had the precious opportunity to discuss problems and receive guidance from such a world-renowned accelerator expert. His suggestions and guidance on beam instability analysis and beam simulation are indispensable factors for my accomplishment of the research work.

I would like to thank my committee members Professors **Richard York**, **Michael Syphers**, **Vladimir Zelevinsky**, **Scott Pratt**, and former member Professor **Jack Baldwin** for their serving in my committee. Their suggestions and guidance on my graduate study played an important role in my academic progress.

I am greatly indebted to the following experienced researchers: Dr. **Gennady Stupakov** (SLAC), Professor **Alex Chao** (SLAC), Dr. **Lanfa Wang** (SLAC), Professor **S. Y. Lee** (Indiana University), Dr. **K. Y. Ng** (FermiLab), Dr. **Fanglei Lin** (JLab). Their

professional suggestions and discussions were crucial for me to avoid wrong directions and make further progress in my research; In particular, I would like to pay my special thanks to Dr. **Wang** and Dr. **Lin** for their excellent contributions to the journal papers collaborated between us, I did benefit and learn a lot from you on analysis methods and paper writing skills.

I would like to give my heartfelt thanks to my colleagues Dr. **Eduard Pozdeyev** and Dr. **Jose Alberto Rodriguez**. Dr. **Pozdeyev** often tailored the beam distributions for me and taught me how to modify the input files for CYCO; Dr. **Rodriguez** gave me patient explanations on the structure of SIR along with step-by-step instructions on running SIR and tuning the beam. Their kind help was important for my research work.

Thanks a lot for the generous help and constructive suggestions on the design and test of the SIR Energy Analyzer provided by Professor **Rami Kishek**, Dr. **Kai Tian** and Dr. **Chao Wu** of University of Maryland. Also many thanks for my colleagues **John Oliva**, **Renan Fontus** and Dr. **Guillaume Machicoane** of NSCL/MSU for their great work on the design, fabrication and test of the analyzer.

Special thanks to my colleagues of NSCL Dr. **Xiaoyu Wu**, Dr. **Yan Zhang**, Dr. **Qiang Zhao**, Professor **Jie Wei**, Professor **Betty Tsang** and Professor **Bill Lynch** for their nice help and useful advice on my graduate study.

I am much obliged to Professors **Phillip Duxbury**, **Wolfgang Bauer**, **Scott Pratt**, **Michael Thoennessen**, **S. D. Mahanti** of Department of Physics and Department Secretary Mrs. **Debbie Barratt** for their excellent management and coordination work.

I am so thankful for Mr. **Hersh Sisodia**, the International Student Advisor at OISS. Your useful and informative consultation was a great help for me.

Thanks to the Editor Dr. **William Barletta** and the **anonymous reviewers** of **Nuclear Instruments and Methods in Physics Research A,** as well as **staff of publisher Elseiver** for their great job in evaluating and publishing my manuscripts.

I will never forget my friend **Jack Wang** for his lasting encouragement and selfless support for my graduate study, as well as his invaluable advice on my career plan.

I would like to thank my friends **Weihai Liu** and his wife Dr**. Cuihong Jia**, Dr. **Weigang Geng**, Dr. **Dat Do** and his wife **Lisa,** Mr**. Dinh Pham** from the bottom of my heart for their generous financial help, encouragement for my study and concern for my daily life.

I am very grateful to my roommate Mr. **Ward Morris-Spidle** and the **Writing Center of MSU** for their careful proofreading, grammar corrections and polishing for my dissertation.

I would also like to express my pure-hearted gratitude for the useful advice, encouragement and support offered by my friends: Dr. **Jianjun Luo**, Dr. **Wei Chang**, Dr. **Chong Zhang**, Dr. **Liangting Sun**, Dr. **Yajun Guo**, Dr. **Xiyang Zhong**, Mr. **Xiaohong Guo**, Dr. **Qiang Nie**, Dr. **Yixing Wang**, Dr. **Jiebing Sun**, Dr. **Bin Guo**, Dr. **Weisheng Cao**, Mrs. **Huan Lian**, Mrs. **Li Li,** Dr. **Feng Shi**, and Mr. **Lixin Zhu**.

TABLE OF CONTENTS

LIST OF TABLES

LIST OF FIGURES

Chapter 1

INTRODUCTION

Isochronous cyclotron is an important family member of modern particle accelerators, with a relatively compact structure and ability of being operated in continuous wave (CW) mode. Using a fixed accelerating frequency, it can accelerate the high intensity hadron beams to medium energy efficiently, typically ranging from several tens of MeV to several hundred MeV. Now isochronous cyclotrons are widely used in various fields and applications, such as research in nuclear physics, medical imaging, radiation therapy and industry, etc.

Since the 1980's, the successful operation of the high power Ring Cyclotron (capable of producing a proton beam of 2.4 mA, 590 MeV with a power of 1.4 MW) at Paul Sherrer Institute (PSI) in Switzerland has greatly inspired the cyclotron community. Consequently, the possibility of design and operation of more powerful cyclotrons (typically, 1 GeV, 10 mA, 10 MW) have been discussed extensively and proposed in some new applications, such as accelerator driven subcritical reactors (ADSR), transmutation of nuclear waste and energy production, neutrino Physics [1-5], etc. M. Seidel provided an excellent review on cyclotrons for high intensity beams [6], their working principles, limitations in the design and operation were briefly introduced. This dissertation mainly discusses the microwave instability of low energy, high intensity beams in isochronous regime induced by space charge effects which is a key issue for the performance of high power cyclotrons.

1.1 Brief introduction to cyclotrons

The first classical cyclotron was proposed and designed by E. O. Lawrence in the early 1930s, in which charged particles move in a vertically uniform magnetic field with a constant revolution frequency (cyclotron frequency). An electric field with fixed radio frequency (RF), which is equal to the cyclotron frequency between two D-shaped electrodes (the Dees), is utilized to accelerate the particles multiple times resonantly to high energy. In order to overcome the energy limits posed by the phase slippage due to relativistic effects and vertical focusing, in 1938, L. H. Thomas proposed the concept of radial sector focusing isochronous cyclotron of which the radially increasing magnetic fields provide isochronism, and the azimuthally varying magnetic fields (AVF) provide vertical focusing (Thomas focusing). In addition, many modern isochronous cyclotrons adopt spiral-shaped sectors which may enhance the vertical focusing further. The accelerated beam can be extracted by some popular methods, such as resonance extraction, stripping extraction for H^- ions, etc.

1.2 Space charge effects in isochronous cyclotrons

When the beam intensity increases in isochronous cyclotrons, the collective effects of the repulsive Coulomb force among the charged particles, which are usually termed space charge effects, become vital factors for the highest intensity attainable in the machine. Refs. [6-7] provide enlightening reviews and discussions regarding the space charge effects in isochronous accelerators.

The space charge effects can be classified into two major categories: incoherent transverse effects and coherent radial-longitudinal ones.

1.2.1 The incoherent transverse space charge field

The incoherent transverse space charge field can decrease the vertical focusing resulting in negative incoherent tune shifts which are proportional to the beam current and $1/\beta^2\gamma^3$ [8], where β and γ are the relativistic speed and energy factors, respectively. Usually, in the central region of isochronous cyclotrons, the vertical focusing force provided by the azimuthally varying magnetic fields (Thomas force) is weaker, thus a beam of high intensity and low energy may have a large tune shift and vertical beam size. The vertical chamber size sets the upper limits for the beam intensity. Higher injection energy is preferred to mitigate the incoherent transverse space charge effects.

1.2.2 The coherent radial-longitudinal space charge field

Different from the incoherent transverse space charge effects which are common for all types of accelerators, the coherent radial-longitudinal space charge effects in isochronous cyclotrons demonstrate some characteristics that are unique in isochronous regime. The longitudinal space charge (LSC) fields within a bunch of finite length may induce energy spread among the charged particles. In isochronous regime, since the longitudinal motion is frozen, particles with higher (or lower) energy must have longer (or shorter) path lengths and larger (or smaller) gyroradii to maintain a constant revolution frequency. This may result in the vortex motion and an *S*-shaped beam, the narrowed turn separation makes clean extraction difficult. For higher power cyclotrons, considerable number of particles hitting the extraction deflectors may cause serious beam loss, overheating and activation of extraction device. The required low extraction loss rate is the limiting factor for the attainable beam intensity in high power isochronous cyclotrons.

More comprehensive knowledge and deeper understanding of space charge effects are crucial for the successful design and operation of high power isochronous cyclotrons. In the past decades, additional extensive studies on this topic have been done through numerical simulations, experiments and analytical models.

1.2.3 Vortex motion

Gordon is the first researcher who explained that the vortex motion in isochronous cyclotrons originates from the space charge force $e\vec{\boldsymbol{E}}_{\boldsymbol{sc}}$ [9], which is equal to half of the *Coriolis* force seen by a particle in a reference frame rotating with constant angular frequency $\vec{\omega}_c$ in the isochronous magnetic field $\vec{\boldsymbol{B}}$

$$m\vec{\omega}_c \times \vec{v} = q\vec{E}_{sc}, \tag{1.1}$$

where m and q are the mass and charge of the particle, respectively, $\vec{v}$ is the speed of particle in the rotating frame, and $\vec{E}_{sc}$ is the space charge field, $\vec{\omega}_c$ is the cyclotron frequency vector

$$\vec{\omega}_c = \frac{q\vec{B}}{m}. \tag{1.2}$$

Another half of the *Coriolis* force in the rotating frame cancels the centrifugal force and *Lorentz* force on the particle. Cerfon [10] interpreted the vortex motion in isochronous regime as nonlinear convection of beam density in the $\vec{\boldsymbol{E}}_{\boldsymbol{sc}} \times \vec{\boldsymbol{B}}$ velocity field

$$\vec{v} = \frac{\vec{E}_{sc} \times \vec{B}}{B^2}. \tag{1.3}$$

Since the cyclotron frequency vector $\vec{\omega}_c$ is proportional to the isochronous magnetic field vector $\vec{\boldsymbol{B}}$ as shown in Eq. (1.2), in fact, the two different interpretations of vortex

motion described in Eqs. (1.1) and (1.3) are equivalent to each other essentially. It can be verified easily by plugging Eqs. (1.2) and (1.3) into Eq. (1.1).

1.2.4 Space charge effects and stability of short circular bunch

By using a closed set of differential equations for the second-order moments of the phase space distribution functions, taking into account the space charge effects, neglecting the force from the image charges and neighboring turns, Kleeven [11] proved that a single free bunch with a circular horizontal cross-section is stationary in a AVF isochronous cyclotron; for a beam with non-circular horizontal initial cross-section, it will not be stable until it evolves to a circular one. This property has been verified and utilized in the successful operation of PSI Injector II, where a buncher is used to produce small round bunches with energy of 870 keV before they are injected into and accelerated in the Injector II. Because the shape of short bunches can barely change during acceleration, a large enough turn separation can be achieved at extraction energy of 72 MeV with high extraction rate (~99.98%). Cerfon [10] also verified and explained this phenomenon by both theory and simulations as discussed in Sect. 1.2.3.

1.2.5 Space charge effects of long coasting bunch

The simulation and experimental work done by Pozdeyev and Rodriguez [12-15] showed that, when a high intensity long bunch with initially uniform longitudinal charge distribution is injected into the Small Isochronous Ring, it may break up into some small clusters longitudinally after only several turns of coasting. Later those small clusters coalesce by consecutive binary cluster merging process. The fast clustering process

observed in simulations and experiments is just the microwave instability of a space-charge dominated beam.

1.2.6 Space charge effects between neighboring turns

For high intensity cyclotrons, the turn separation decreases at high energy. Consequently, the space charge effects contributed from the radially neighboring turns must be considered in the beam dynamics.

Using a 3D parallel Particle-In-Cell (PIC) simulation code OPAL-CYCL, a flavor of the Object Oriented Parallel Accelerator Library (OPAL) framework developed by Adelmann of PSI [17], the space charge effects between neighboring turns in the PSI 590 MeV Ring Cyclotron were simulated by Yang adopting a self-consistent algorithm [18]. The simulation results show that there is a considerable difference between single-bunch and multi-bunch dynamics. The space charge forces contributing from the radially neighboring turns may ‘squeeze’ the radial beam size to some extents and play a positive role in maintaining turn separation and reducing the energy spread.

From the above information, we can see it is challenging to design and operate a high intensity cyclotron keeping a low level of beam loss and activation. The effects of an incoherent transverse space charge field, a coherent radial-longitudinal space charge field and neighboring turns are crucial factors thus must be taken into account. This requires a better understanding and manipulation of the space charge effects in isochronous regime.

1.3 CYCO and Small Isochronous Ring

Usually it is difficult to study analytically the beam dynamics with space charge in

isochronous ring due to complex boundary conditions of the accelerator, nonlinear effects resulting from beam shape and distributions. Thus, the numerical method using simulation codes and experimental method utilizing a real isochronous accelerator are heavily relied upon in the research.

Since the beam dynamics of the existing simulation codes were then simplified in the treatment of space charge effects, Pozdeyev developed a novel 3D Particle-In-Cell simulation code named CYCO to study the beam dynamics with space charge in isochronous regime [12]. In the simulation, at first, an initial distribution of a number of macroparticles (typically 3×10^5) representing the real long ion bunch (typically 40 cm long) needs to be created either by the code with a default distribution or by users' self-definition. Using the classical 4^{th} order Runge-Kutta method, the code can numerically solve the complete and self-consistent system of six equations of motion of the charged macroparticles in a realistic 3D field map including the space charge fields. Because of the large aspect ratio between the vacuum chamber width and height of the storage ring, the code only includes the image charge effects in the vertical direction. The rectangular vacuum chamber is simplified as a pair of infinitely large, ideally conducting plates parallel to the median ring plane. The beam profiles can be output turn by turn for post-processing and analysis.

In order to validate the simulation code CYCO and study the space charge effects in the isochronous regime, a low energy, low beam intensity Small Isochronous Ring (SIR) was constructed during 2001-2004 at the National Superconducting Cyclotron Laboratory (NSCL) at Michigan State University (MSU). In addition, two graduate students Pozdeyev and Rodriguez conducted a thesis project and the SIR has been in operation

until 2010 [12-13]. According to the scaling laws, the space charge regime of the low energy, low intensity H_2^+ beam in SIR covers a large region in beam dynamics. This compact accelerator ring can be used to simulate the space charge effects of the large scale, high power isochronous cyclotrons such as the PSI Injector II cyclotron. Due to the loose requirements of time resolution and beam power for diagnostic tools, good availability and flexibility in the operation, the SIR is an ideal experimental facility to study the space charge effects in the isochronous regime.

The Small Isochronous Ring consists of three main parts: a multi-cusp Hydrogen ion source, an injection line, and a storage ring as shown in Figure 1.1. Its main parameters are listed in Table 1.1.

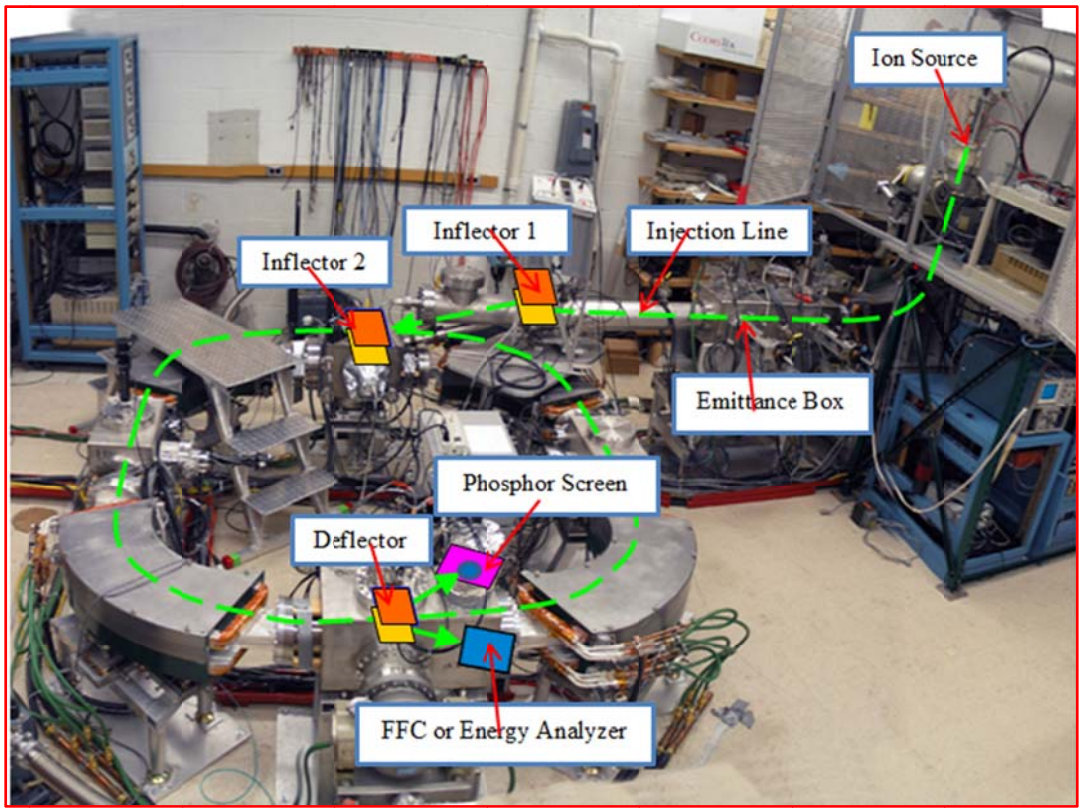

Figure 1.1: A photograph of the SIR with some key elements indicated.

Table 1.1: Main parameters of SIR

Ring circumference	6.58 m
Particle species	H^+, H_2^+, H_3^+, mainly use H_2^+
Kinetic energy	0 -30 keV
Peak current	0-40 μA for H_2^+
RMS emittance	Typically 2-3π *mm mrad*
Ring lattice	Four 90-degree dipole magnets
Bending radius	0.45 m
Dipole pole face angle	26^o
Mag. field strength	800 Gauss
Bare horizontal tune ν_x	1.14
Bare vertical tune ν_y	1.11
Bare slip factor η_0	$\sim 2.0 \times 10^{-4}$
Beam life time	~200 turns

The ion source produces three species of Hydrogen ions: H^+, H_2^+, and H_3^+. An analyzing dipole magnet under the ion source is used as a magnetic mass separator to select the H_2^+ ions which are usually used in the experiments. The H_2^+ ion beam with proper Courant-Snyder parameters and desired bunch length can be produced by an electrostatic quadrupole triplet and chopper in the injection line. The storage ring has a circumference of 6.58 meter. It mainly consists of four identical flat-field 90^o bending magnets with edge focusing. The pole faces of each magnet are rotated by 26^o in order to provide both the vertical focusing and isochronism at the same time. After being injected to the storage ring by two fast-pulsed electrostatic inflectors (Inflector 1 and Inflector 2 in Figure 1.1), the bunch may coast in the ring up to 200 turns. There is a Measurement Box located in the drift line between the 2^{nd} and 3^{rd} bending magnets in the ring. A pair of fast-pulsed electrostatic deflector in the Measurement Box can kick the beam either up to a phosphor screen above the median ring plane, or down to the fast Faraday cup (FFC) below the median ring plane. The phosphor screen and fast Faraday cup are used to monitor the transverse and longitudinal beam profiles, respectively. We can also perform

energy spread measurements if the fast Faraday cup assembly is replaced by an energy analyzer assembly.

A double-slit emittance measurement assembly is located in the Emittance Box of the injection line. It is used to measure the RMS emittance in horizontal and vertical phase space. An Einzel Lenz right under the ion source can focus the divergent beam. Together with the electrostatic quadrupole triplet in the injection line, users can obtain the proper Courant-Snyder parameters. A shielded Faraday cup at the end of the injection line is used to measure the beam current when the Inflector 1 is turned off. Two pairs of horizontal and vertical scanning wires are installed in the storage ring to monitor the transverse beam profiles. In order to adjust the betatron tunes and isochronism, four electrostatic quadrupoles and four gradient correctors are installed in the ring between the bending magnets and situated in the dipole magnets, respectively.

1.4 Summaries of previous studies of beam instability in SIR

It was observed both in simulations by CYCO and experiments at SIR, a coasting long bunch with uniform longitudinal charge density may develop a fast growth of density modulation. The whole bunch breaks up into many small clusters in the longitudinal direction quickly. Furthermore, the neighboring small clusters may merge together to form bigger ones by a consecutive binary merging process. Figure 1.2 shows the measured temporal evolutions of the longitudinal bunch profiles of a coasting beam with the beam energy of 20.9 MeV and the peak current of 9.3 μA [15]. Figure 1.3 shows the simulation results of the beam dynamics in SIR for three different peak intensities: 5 μA, 10 μA, and 20 μA [13].

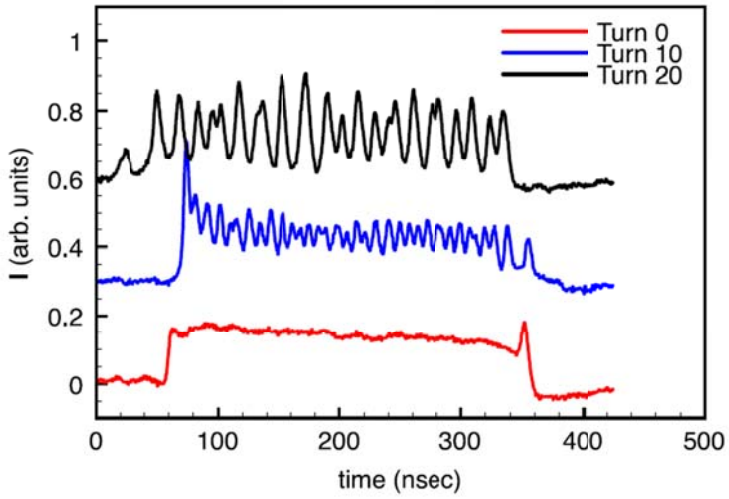

Figure 1.2: Longitudinal bunch profiles measured by the fast Faraday cup right after injection (turn 0), at turn 10 and turn 20. The current profiles measured at turn 10 and turn 20 are shifted vertically by 0.3 and 0.6, respectively [15].

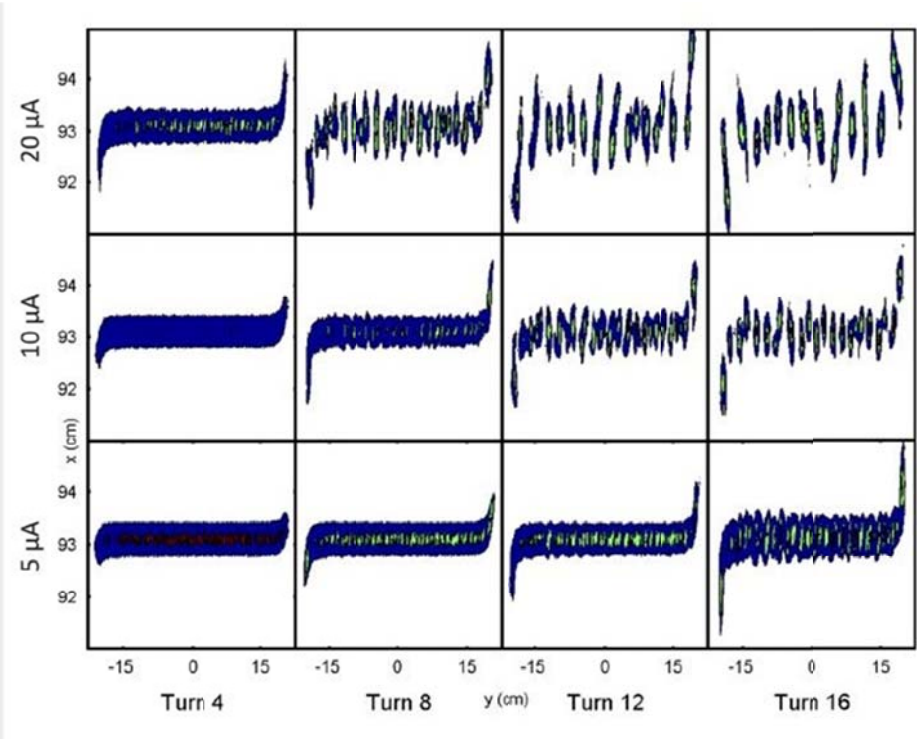

Figure 1.3: Simulation results of the beam dynamics in SIR for three different peak densities: 5 μA, 10 μA, and 20 μA [13].

In order to study the dependence of beam instability on various initial beam parameters, Rodriguez carried out extensive simulations and experimental studies [13]. He studied the temporal evolutions of the number of clusters by means of the cluster-counting technique. The simulation and experimental results agreed to each other quite well. Finally, several scaling laws of instability growth rates with respect to the various beam parameters (e.g., the beam current, energy, emittance and bunch length) were set up empirically. It was found that the instability growth rates are proportional to the beam current instead of the square root of beam current. This property contradicts the prediction by the conventional theory of microwave instability. Rodriguez also counted the decreasing number of clusters and fit it to an empirical exponential function of turns.

Pozdeyev explained [14-15] that the centroid wiggling of a long bunch in isochronous ring plays an important role in the microwave instability. It may produce coherent radial space charge fields, modify the dispersion function and coherent slip factor, raise the working point above transition and enhance the negative mass instability. Plugging the modified coherent slip factor into the conventional 1D formula for microwave instability growth rates, Pozdeyev derived an instability formula which can predict the linear dependence of instability growth rates on beam current. While this model overestimates the growth rate of short-wavelength perturbations. Later, Bi [16] proposed another model consisting of a round perturbed beam inside a round chamber. This model takes into account the effect of centroid offsets on transition gamma. Bi derived a 1D dispersion relation that can predict the fastest-growing mode and explain the various scaling laws. But this model is not consistent with the scaling laws on beam current, since the DC current component is neglected in calculating the coherent radial space charge field.

1.5 Major research results and conclusions in this dissertation

In spite of the pioneering work done by Pozdeyev, Rodriguez and Bi [12-16], some central questions still remain in regard to the more accurate, comprehensive and deeper understanding of the microwave instability in isochronous regime. For example,

(a) None of Pozdeyev [14-15] and Bi's theoretical models [16] utilized the longitudinal space charge (LSC) field and impedance models that exactly match the geometries of the real beam-chamber system and can work at any perturbation wavelengths. The validity of their LSC field and impedance models needs to be verified. It is highly desirable for the beam physicists to obtain the analytical LSC impedances for a round beam with sinusoidal density modulations inside a rectangular chamber, or between parallel plates (e.g., in CYCO). Moreover, the derived LSC impedances should be accurate enough at any perturbation wavelengths.

(b) Is the 1D growth rate formula or dispersion relation adopted by Pozdeyev [14-15] and Bi [16] accurate enough to predict the instability growth rates at any wavelengths? How do the energy spread and emittance neglected in their models affect the instability growth rates? How to introduce the well-known Landau damping effects in the isochronous regime?

(c) How does the energy spread of clusters evolve? What is the asymptotic behavior of the energy spread and why? How and why the cluster pair merge?

This dissertation primarily discusses and answers the above questions. To predict the microwave instability growth rates more accurately, this dissertation

(1) derives the analytical LSC impedances of a rectangular and round beam inside a rectangular chamber and between parallel plates;

(2) derives a 2D dispersion relation incorporating the Landau damping effects contributed from finite energy spread and emittance. It can explain the suppression of microwave instability growth rates at short perturbation wavelengths and predict the fastest-growing wavelength;

(3) studies the evolution of energy spread of SIR bunch by both simulation and experimental methods. We have designed a compact rectangular electrostatic retarding field analyzer [19] with a large entrance slit. The simulation and experimental studies of energy spread evolution of a long coasting bunch show that the slice RMS energy spread of clusters changes slowly at large turn numbers. This may result from nonlinear advection of the beam in the $\vec{E} \times \vec{B}$ velocity field [10].

1.6 Brief introduction to contents of the following chapters

Chapter 2 gives a brief introduction to some most important concepts and dynamics regarding the isochronous ring, including the momentum compaction factor, dispersion function, slip factor, beam optics of SIR lattice (hard-edge model), microwave instability, Landau damping, etc.

Chapter 3 derives the analytical LSC fields and impedances of (a) a rectangular beam and (b) a round beam with planar and rectangular boundary conditions, respectively. The derived LSC impedances match well with the numerical simulations. We study the effects of the cross-sectional geometries of both the beam and chambers on the LSC impedances.

Chapter 4 discusses the Landau damping effects of a coasting long bunch in the SIR. The limits of the conventional 1D formalisms used in the existing models are pointed out; a modified 2D dispersion relation suitable for the beam dynamics in the isochronous

regime is derived, by which the Landau damping effects are studied. It can explain the suppression of instability growth and predict the fastest-growing wavelength.

Chapter 5 introduces the working principles, simulation design, and mechanical structure of a rectangular retarding field energy analyzer with large entrance slit. The dissertation provides the tested performance and sensitivity of the analyzer.

Chapter 6 is devoted to studying the nonlinear beam dynamics of the microwave instability, including (a) energy spread measurements and simulations. First, this chapter gives a brief introduction to the measurement system, and then the measurement and data analysis methods. The simulation and experimental results are compared with each other; their physical meaning is interpreted by simple analysis. (b) verification of Cerfon's theory [10] on the vortex motion in $\vec{\boldsymbol{E}} \times \vec{\boldsymbol{B}}$ field by two-macroparticle model and two-bunch model.

Chapter 7 summarizes the main research results addressed in this dissertation and points out some possible research directions in the future.

Chapter 2

BASIC CONCEPTS AND BEAM DYNAMICS

For the convenience of further discussions on microwave instability in the following chapters, this chapter briefly summarizes some basic but important concepts that are essential in understanding the unique beam dynamics in the isochronous regime.

2.1 The accelerator model for the SIR

In this dissertation, the same accelerator model as the one used in Ref. [20] is adopted for the SIR. Figure 2.1 shows the schematic view of the coordinate system for the accelerator model.

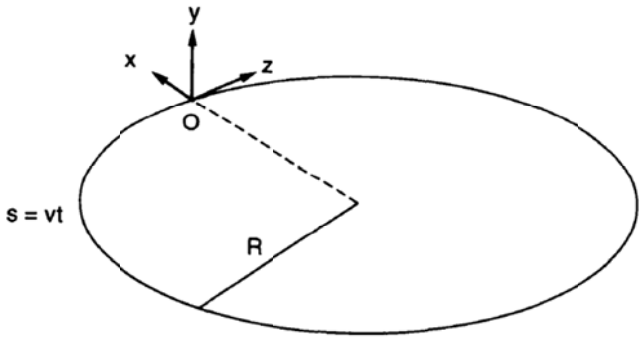

Figure 2.1: A simplified accelerator model for the SIR, in which x, y, and z denote the radial, vertical and longitudinal coordinates of the charged particle with respect to the reference particle O. (Note: the figure is reproduced from Ref. [20]).

The SIR is assumed to be an ideal circular storage ring with a circumference of $C_0=2\pi R$, where R is the average ring radius. A beam is coasting in the ring. Assume a hypothetical reference particle O within the bunch circulates along the design orbit turn after turn with

the exact design energy $E = \gamma m_{H_2^+} c^2$, where γ is the relativistic energy factor of the on-momentum particle, $m_{H_2^+}$ is the rest mass of the Hydrogen molecular ion H_2^+, c is the speed of light. The reference particle has a velocity of $v=\beta c$, where β is the relativistic speed factor. The distance traveled by the reference particle with respect to a fixed point of the storage ring is $s=vt=\beta ct$. For an arbitrary particle in the bunch, x, y, and z denote its radial, vertical and longitudinal coordinates with respect to the reference particle O, respectively. Then the motion of an arbitrary particle can be described by a six-component vector (x, x', y, y', z, δ) in phase space, where $x'=dx/ds$, and $y'=dy/ds$ are the radial and vertical velocity slopes relative to the ideal orbit, $\delta=\Delta p/p$ is the fractional momentum deviation. For a coasting SIR beam, we can choose a hypothetical on-momentum particle at the bunch center as the reference particle. For those off-momentum particles in a circular accelerator, there are three important parameters describing their motions: *momentum compaction factor* α, *dispersion function* $D(s)$ and *phase slip factor* η.

2.2 Momentum compaction factor

In a circular accelerator, the particles of different energy circulate around different closed orbits resulting in different path length C and different equilibrium radius. In beam dynamics, the ratio between the fractional path length deviation $\Delta C/C_0$ (or fractional equilibrium radius deviation $\Delta R/R$) and the fractional momentum deviation $\delta=\Delta p/p$ is customarily defined as the *momentum compaction factor*:

$$\alpha = \frac{\Delta C / C_0}{\Delta p / p} = \frac{\Delta R / R}{\Delta p / p}. \tag{2.1}$$

It is a measure for the change in equilibrium radius due to the change in momentum.

2.3 Dispersion function

The off-momentum particles with $\delta=\Delta p/p$ may have different closed (equilibrium) orbits from that of the on-momentum reference particle, yielding a horizontal (radial) displacement $x(s)$ in x-coordinate. Then the *periodic dispersion function* in a circular accelerator is defined as

$$D(s)=\frac{x(s)}{\delta}. \tag{2.2}$$

Both the momentum compaction factor α and the *periodic dispersion function* D(s) reflect the radial-longitudinal coupling of circular accelerators, which is an intrinsic property of the circular accelerators resulting from the guiding magnetic fields. Moreover, α and D(s) are related to each other by (Eq. (3.136) of Ref. [21])

$$\alpha=\frac{1}{C_0}\oint\frac{D(s)}{\rho(s)}ds=\langle\frac{D(s)}{\rho(s)}\rangle, \tag{2.3}$$

where $\rho(s)$ is the local radius of the curvature of trajectory, $\langle\cdots\rangle$ stands for the average value over the accelerator circumference. Let us assume all the bending magnets in the storage ring are identical to each other with bending radius ρ_0. Since a straight section has a bending radius of $\rho(s)=\infty$, only the dispersion function in the bending magnets contributes to α, then Eq. (2.3) can be written as

$$\alpha=\frac{1}{C_0\rho_0}\int_{bend}D(s)ds. \tag{2.4}$$

If the total length of bending magnets is $L_{bend}=2\pi\rho_0$, the average value of dispersion function in the bending magnet is

$$< D(s) >_{bend} = \frac{1}{2\pi\rho_0}\int_{bend} D(s)ds. \tag{2.5}$$

Then Eq. (2.4) reduces to

$$\alpha = \frac{2\pi\rho_0 < D(s) >_{bend}}{C_0\rho_0} = \frac{< D(s) >_{bend}}{R}. \tag{2.6}$$

where $R=C_0/2\pi$ is the average ring radius.

2.4 Transition gamma

The *transition gamma* γ_t in circular accelerators is defined as

$$\gamma_t^2 = \frac{\Delta p / p}{\Delta R / R}. \tag{2.7}$$

It is easy to learn from Eq. (2.1) and Eq. (2.7) that

$$\alpha = \frac{1}{\gamma_t^2}. \tag{2.8}$$

The total energy of a particle with transition gamma is just the *transition energy* which is equal to $E_t = \gamma_t mc^2$.

2.5 Slip factor

The revolution period of a particle is $T = 2\pi R/\beta c$, the fractional deviations of the relativistic speed and momentum are related by $\Delta\beta/\beta = \delta/\gamma^2$, then with Eq. (2.7),

$$\frac{\Delta T}{T_0} = -\frac{\Delta\omega}{\omega_0} = \frac{\Delta R}{R} - \frac{\Delta\beta}{\beta} = (\frac{1}{\gamma_t^2} - \frac{1}{\gamma^2})\delta = \eta\delta, \tag{2.9}$$

where T_0 and ω_0 are the revolution period and angular revolution frequency of the on-momentum reference particles, respectively, η is the phase *slip factor* defined as

$$\eta = \frac{1}{\gamma_t^2} - \frac{1}{\gamma^2} = \alpha - \frac{1}{\gamma^2}. \tag{2.10}$$

For the SIR, the bare slip factor without the space charge effect is $\eta_0 \approx 2\times10^{-4}$.

The revolution time and frequency of an off-momentum particle is determined by its changes in both velocity and path length. A particle with higher energy (δ>0) has a faster velocity and travels along a longer path length compared with the on-momentum reference particle (δ=0). For the case of $\gamma<\gamma_t$, below the transition, η<0, the faster speed of the higher energy particle (δ>0) may compensate for the longer path, this will result in a shorter revolution period (ΔT<0 in Eq. (2.9)) or higher revolution frequency ($\Delta\omega$>0 in Eq. (2.9)) compared with the on-momentum reference particle. While for the case of $\gamma>\gamma_t$, above the transition, η>0, the increase of path length of the higher energy particle (δ>0) may dominate over the increase of velocity. This will result in a longer revolution period (ΔT>0 in Eq. (2.9)) or lower revolution frequency ($\Delta\omega$<0 in Eq. (2.9)) compared with the on-momentum reference particle.

At transition, $\gamma=\gamma_t$, η=0, the revolution period (or frequency) of the particle is independent of its energy (or momentum). For a coasting bunch, if the space charge effects among the particles are excluded, all the particles with different energy will circulate along the accelerator rigidly with the same period (or frequency). This is the *isochronous regime*, in which the Small Isochronous Ring (SIR) is designed to be operated. Unfortunately, this is a regime which is most vulnerable to the perturbations and prone to beam instability for a space-charge dominated beam.

2.6 Beam optics for hard-edge model of SIR

Figure 2.2 depicts the layout of the SIR lattice. In consists of four 90-degree bending

magnets (B1-B4) connected by four straight drift sections (S1-S4). The pole face of each bending magnet is rotated by an angle φ for isochronism and vertical focusing.

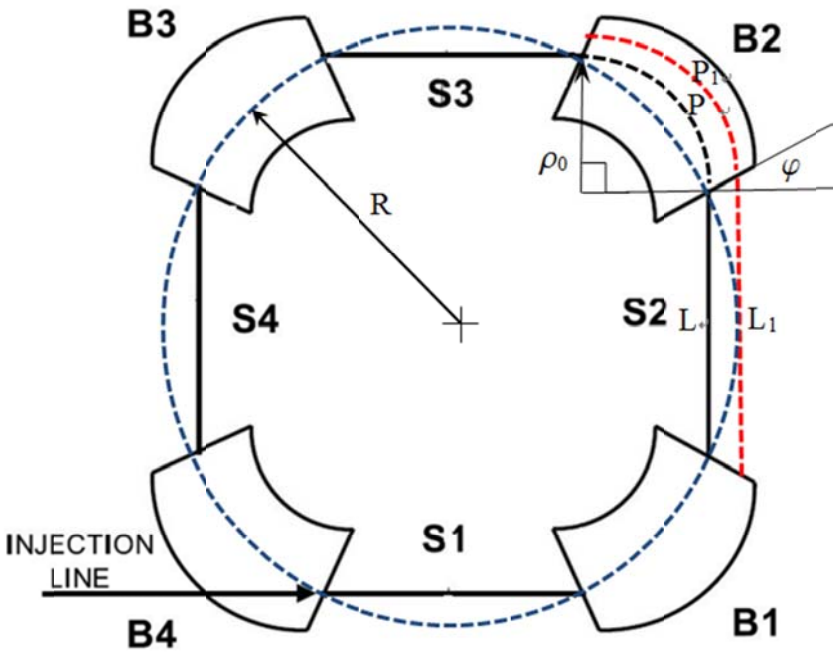

Figure 2.2: Layout of the SIR lattice.

Table 2.1: Parameters of SIR (hard-edge model)

Number of magnets N	4	Rotation angle of pole face φ	25.159^o
Bending radius ρ_0	0.45 m	Horizontal tune ν_x	1.14
Drift length L	0.79714 m	Vertical tune ν_y	1.17

Table 2.1 lists the main parameters of the hard-edge model of the SIR lattice [12]. Here the term 'hard–edge' means all the fringe magnetic fields are neglected.

Figure 2.3 shows the simulated optical functions $\hat{\beta}_x(s)$, $\hat{\beta}_y(s)$, and $D_x(s)$ v.s distance s of a single period of the ring calculated by code DIMAD.

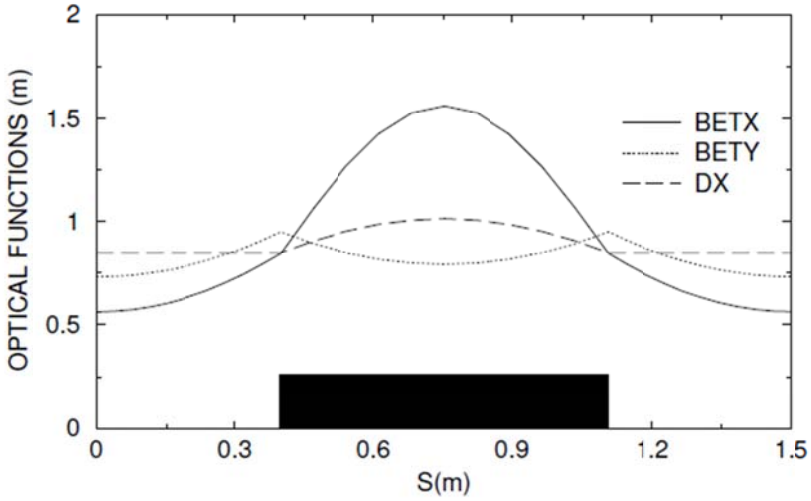

Figure 2.3: The optical functions v.s distance of a single period of the ring. The black rectangle schematically shows one of the dipole magnets. The legend items 'BETX', 'BETY', and 'DX' stand for the horizontal beta function $\hat{\beta}_x(s)$, vertical beta function $\hat{\beta}_y(s)$, and horizontal dispersion function $D_x(s)$, respectively. (Note: The figure is reproduced from Ref. [12]).

The design of SIR by the hard-edge model is based on the assumption: all the particles in a bunch with different energy deviations travel along their individual equilibrium (closed) orbits with the same nominal revolution period T_0. These particles do not perform betatron oscillations. Let us assume a non-relativistic particle with a positive fractional momentum deviation $\delta=\Delta p/p>0$ travels along its equilibrium orbit as indicted by the red dashed line in Figure 2.2. In order to obtain isochronism, in one period of the ring, the following equality should hold

$$\frac{L+P}{v}=\frac{L_1+P_1}{v_1} \tag{2.11}$$

where L, P are the straight and curved path length of the on-momentum particle with velocity v, respectively. L_1, P_1 and v_1 are the corresponding quantities of the off-momentum particle. Eq. (2.11) dictates the rotation angle of pole face [12]

$$\tan(\varphi) = \frac{L/2}{\rho_0 + \frac{L/2}{\tan(\frac{\pi}{4})}}. \tag{2.12}$$

By smooth approximation, the design orbit of SIR lattice can be treated as an ideal circle with average radius R as indicated by the blue dashed circle in Figure 2.2.

Neglecting the vertical motion, the Hamiltonian of a single particle coasting in SIR without space charge field and applied electric field is

$$H = \frac{x'^2}{2} + \frac{k_x x^2}{2} - \frac{x}{R}\delta + \frac{\delta^2}{2\gamma^2}, \tag{2.13}$$

where k_x is the radial (horizontal) focusing strength. According to the Hamiltonian mechanics,

$$\frac{dx}{ds} = \frac{\partial H}{\partial x'}, \qquad \frac{dx'}{ds} = -\frac{\partial H}{\partial x}, \qquad \frac{dz}{ds} = \frac{\partial H}{\partial \delta}, \qquad \frac{d\delta}{ds} = -\frac{\partial H}{\partial z}, \tag{2.14}$$

the equations of motion of a single particle are

Radial (horizontal): $$\frac{dx}{ds} = x', \qquad \frac{dx'}{ds} = -k_x x + \frac{\delta}{R}, \tag{2.15}$$

Longitudinal: $$\frac{dz}{ds} = -\frac{x}{R} + \frac{\delta}{\gamma^2}, \qquad \frac{d\delta}{ds} = 0. \tag{2.16}$$

The two radial equations of motion in Eq. (2.15) can also be combined as

$$\frac{d^2x}{ds^2} = -k_x x + \frac{\delta}{R}. \tag{2.17}$$

Using smooth approximation, $k_x = \frac{\nu_x^2}{R^2}$, where ν_x is the radial (horizontal) betatron tune, Eq. (2.17) can be rewritten as

$$\frac{d^2x}{ds^2} + \frac{\nu_x^2}{R^2}x = \frac{\delta}{R}. \tag{2.18}$$

Its general solution is

$$x(s) = A\cos(\frac{\nu_x}{R}s) + B\sin(\frac{\nu_x}{R}s) + \frac{R}{\nu_x^2}\delta, \tag{2.19}$$

$$x'(s) = -A\frac{\nu_x}{R}\sin(\frac{\nu_x}{R}s) + B\frac{\nu_x}{R}\cos(\frac{\nu_x}{R}s), \tag{2.20}$$

where the coefficients A and B depend on the initial conditions of the particle.

In smooth approximation, the dispersion function is $D(s)=R/\nu_x^2$, the motion of an off-momentum particle travelling along the equilibrium orbit can be analyzed conveniently using the above equations. Assume at s=0, a particle's initial radial offset, slope and fractional momentum deviation are $x(0) = D\delta = R\delta/\nu_x^2$, $x'(0) = 0$, and $\delta \neq 0$, respectively. From Eqs. (2.19) and (2.20), it is easy to obtain A=B=0, then the radial equation of motion is simplified as

$$x(s) = \frac{R\delta}{\nu_x^2}. \tag{2.21}$$

Substituting Eq. (2.21) into Eq. (2.16), the longitudinal equation of motion becomes

$$\frac{dz}{ds} = -\frac{\delta}{\nu_x^2} + \frac{\delta}{\gamma^2}. \tag{2.22}$$

The longitudinal coordinate $z(s)$ can be solved by integration as

$$z(s) = z(0) - (\frac{1}{\nu_x^2} - \frac{1}{\gamma^2})\delta s. \tag{2.23}$$

The *one-turn* slip factor at s=0 can be calculated as

$$\eta = -\frac{1}{C_0}\frac{z(C_0) - z(0)}{\delta} = \frac{1}{\nu_x^2} - \frac{1}{\gamma^2}. \tag{2.24}$$

Note that for an isochronous ring, the term $1/\nu_x^2$ in Eq. (2.24) should be replaced by

$1/\gamma_t^2$, where γ_t is the transition gamma defined in Eq. (2.7). Then the slip factor in Eq. (2.24) becomes

$$\eta = \frac{1}{\gamma_t^2} - \frac{1}{\gamma^2} = \eta_0, \tag{2.25}$$

where η_0 is the bare slip factor.

The slip factor in Eq. (2.25) is derived for an off-momentum particle without betatron oscillation. Here comes a question, if a particle performs radial (horizontal) betatron oscillation around its equilibrium orbit, how does the slip factor change? Let us study the motion of a particle with the initial condition of $x(0) = 0,\ x'(0) = 0,$ and $\delta \neq 0$. The particle will perform betatron oscillation around its equilibrium orbit with radial offset $x_{eq} = D\delta = \frac{R\delta}{\nu_x^2}$. From Eqs. (2.19) and (2.20), the radial equation of motion is solved as

$$x(s) = \frac{R\delta}{\nu_x^2}[1 - \cos(\frac{\nu_x}{R}s)], \tag{2.26}$$

which yields the longitudinal equation of motion

$$\frac{dz}{ds} = -\frac{\delta}{\nu_x^2}[1 - \cos(\frac{\nu_x}{R}s)] + \frac{\delta}{\gamma^2}. \tag{2.27}$$

Then the longitudinal coordinate $z(s)$ is obtained by integration as

$$z(s) = z_0 - (\frac{1}{\nu_x^2} - \frac{1}{\gamma^2})\delta s + \frac{R\delta}{\nu_x^3}\sin(\frac{\nu_x}{R}s), \tag{2.28}$$

The last term in Eq. (2.28) is an oscillatory function of s. The 1-*turn* slip factor at s=0 is

$$\eta_{1-turn}(0) = -\frac{1}{C_0}\frac{z(C_0) - z(0)}{\delta} = (\frac{1}{\nu_x^2} - \frac{1}{\gamma^2}) - \frac{1}{2\pi\nu_x^3}\sin(2\pi\nu_x). \tag{2.29}$$

Replacing the term $1/\nu_x^2$ by $1/\gamma_t^2$, then the 1-*turn* slip factor at s=0 in Eq. (2.29) for

the isochronous ring becomes

$$\eta_{1-turn}(0) = (\frac{1}{\gamma_t^2} - \frac{1}{\gamma^2}) - \frac{1}{2\pi\nu_x^3}\sin(2\pi\nu_x). \tag{2.30}$$

The comparison between Eqs. (2.25) and (2.30) indicates that, for an off-momentum particle performing betatron oscillation around its equilibrium orbit, there is an extra term $-\frac{1}{2\pi\nu_x^3}\sin(2\pi\nu_x)$ in the slip factor. A similar extra term also appears in the 2D dispersion relation Eq. (4.41) derived in Chapter 4. For the hard-edge model of SIR lattice, the two terms in Eq. (2.30) are

$$\frac{1}{\gamma_t^2} - \frac{1}{\gamma^2} = \eta_0 = 0, \qquad \text{and} \qquad -\frac{1}{2\pi\nu_x^3}\sin(2\pi\nu_x) \approx -0.083, \tag{2.31}$$

respectively. Then the total slip factor taking into account betatron oscillation effect becomes negative (below transition). Note that in the conventional definitions of the momentum compaction factor α and slip factor η, the effects of betatron oscillation are all neglected. For conventional circular accelerators whose working points are far from transition, the extra term in the new slip factor can be neglected. While in the isochronous ring, due to smallness of the bare slip factor η_0, this extra term should be taken into account in the instability analysis. The above discussions show that the betatron oscillation may destroy the isochronism.

Assume an on-momentum particle coasts along the design trajectory of SIR with $x(s) = 0$, $x'(s) = 0$, $\delta(s) = 0$. The particle may maintain its isochronous motion for ever if there are no external perturbing forces. At a given position s_1, for some reasons (e.g., LSC field, RF electric field), the particle receives a sudden longitudinal kick, so that $x(s_1)$ and $x'(s_1)$ are not changed but $\delta(s_1) \neq 0$. Then according to the above analysis, the

particle will perform betatron oscillation and lose its isochronism.

We can see that, even if in an ideal isochronous ring, not all the particles can keep the isochronous motion. Only those particles whose radial offset, radial slope and momentum deviation satisfy the closed orbit condition can maintain the isochronous motion.

Appendix A provides more studies on the beam optics of the SIR lattice (hard-edge model) using the standard matrix formalism.

2.7 Negative mass instability (microwave instability)

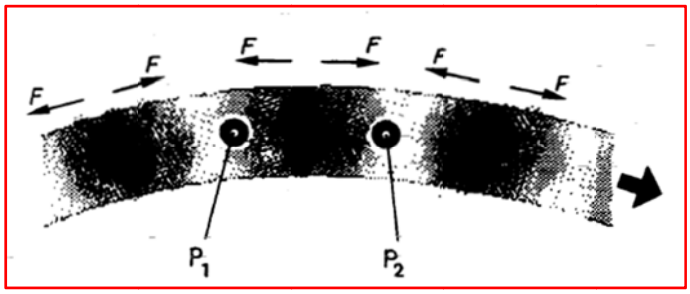

Figure 2.4: Mechanism of negative mass instability or microwave instability (The figure is reproduced from Ref. [8]).

Assume at a given time, there are small longitudinal charge density perturbations in a bunch circulating in an accelerator above transition as shown in Figure 2.4. The charge density variations will produce a self-field (or space charge field) directing from the density peak region to the density valley region. The particles on the forward side of the density bump such as P_2 will see a pushing force F and gain energy, while the particles on the trailing side of the density bump such as P_1 will see a pulling self-force F and lose energy. The on-momentum reference particle located right at the density peak sees zero self-force and keeps a constant energy. The discussion in Sect. 2.5 tells us that, above transition, the higher energy particle like P_2 has a lower revolution frequency than the

on-momentum reference particle, while the lower energy particle like P_1 has a higher revolution frequency than the on-momentum reference particle. This may result in an enhancement of the azimuthal density modulation amplitude. In beam instability analysis, this self-bunching phenomenon is usually termed the *negative mass instability*. The term comes from the illusion that the particles seem to move in the opposite directions from the self-force or space charge force exerting on them. Usually the space–charge driven negative mass instability is characterized by density perturbation wavelengths which are much shorter than the bunch length. For this reason, it is also named *microwave instability* in modern literature.

2.8 Microwave instability in the isochronous regime

The microwave instability in the isochronous regime is the main topic of this dissertation. It demonstrates some unique features that cannot be explained by the conventional theory of microwave instability. For example, the instability growth rate is proportional to the unperturbed beam intensity I_0 instead of the square root of I_0. This confusing phenomenon is first explained by Pozdeyev in Refs. [14-15]. He pointed out that, in a circular accelerator, the longitudinal density modulation produces the longitudinal space charge (LSC) field modulation and the coherent energy modulation along the beam. In consequence, the local beam centroid wiggling takes place due to dispersion function as shown in Figure 2.5. The coherent radial space charge field on the local centroid is proportional to the local centroid offset, which in turn will modify the dispersion function D, momentum compaction factor α and produce a positive increment of the coherent slip factor $\Delta\eta_{coh}$ of the local centroid. For a space-charge dominated beam,

$\Delta\eta_{coh}$ is proportional to I_0 and dominates over the vanishingly small bare slip factor η_0. Therefore, the working point of the nominal isochronous ring turns out to be raised above transition where the microwave instability may take place with a growth rate proportional to I_0.

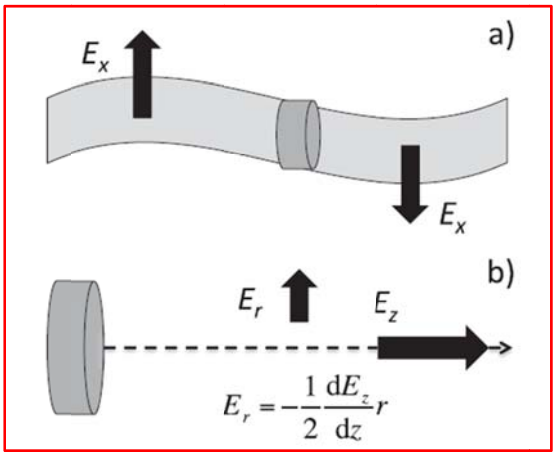

Figure 2.5: Schematic drawing of beam centroid wiggling and the associated coherent space charge fields (The figure is reproduced from Ref. [15]).

Pozdeyev's theory clearly shows that the radial-longitudinal coupling and centroid wiggling play a key role in the mechanism of the microwave instability in the isochronous regime.

2.9 Landau damping

As discussed in Sects. 2.6 and 2.8, the betatron motion, the space charge field and centroid wiggling may destroy the isochronism. Therefore, an *ideal* isochronous ring becomes a *quasi-isochronous* ring with a non-zero slip factor. For a bunch with given energy (or momentum) spread and emittance coasting in a *quasi-isochronous* ring, there will be a revolution frequency spread among the particles. The resulting revolution

frequency spread may tend to counteract and smear out the longitudinal self-bunching, and then the beam instability will be prevented or suppressed. This mechanism of instability suppression is termed *Landau damping* in the literature. Chapter 4 discusses the Landau damping in the isochronous regime in detail by a 2D dispersion relation.

2.10 Coherent and incoherent motions

The terms of *coherent* and *incoherent* are used to describe the properties of a local *beam centroid* and a *single particle* in this dissertation, respectively. The subscripts '*coh*' and '*inc*' are added to the corresponding parameters to tell them apart. For example, the equations of coherent and incoherent radial motions of a SIR beam can be expressed as:

$$x_c'' + \frac{v_x^2}{R^2} x_c = \frac{\delta_{coh}}{R} + \frac{eE_{x,coh}}{\gamma m_{H_2^+} \beta^2 c^2}, \tag{2.32}$$

$$x_\beta'' + \frac{v_x^2}{R^2} x_\beta = \frac{\delta_{inc}}{R} + \frac{eE_{x,inc}}{\gamma m_{H_2^+} \beta^2 c^2}, \tag{2.33}$$

where v_x is the bare radial betatron tune which is the number of betatron oscillations per revolution without space charge effects; δ_{coh} and δ_{inc} are the *coherent* and *incoherent* fractional momentum deviations, $E_{x,coh}$ and $E_{x,inc}$ are the *coherent* and *incoherent* radial space charge fields, respectively.

Chapter 3

STUDY OF LONGITUDINAL SPACE CHARGE IMPEDANCES[1]

3.1 Introduction

When a charged beam travels along a surrounding metallic vacuum chamber, the space charge field inside the beam will perturb the beam resulting in beam instability under some circumstances. For example, the space charge effect plays an important role in the microwave instability of low energy beam with high intensity near or above transition [14-16]. The space charge field is also one of the important reasons causing the microbunching instability for free-electron lasers (FELs) [22]. An accurate calculation of the LSC fields and impedances is helpful to explain the beam behavior and predict the growth rates of the beam instability with a good resolution. Both the direct self-fields of the beam and its image charge fields due to the conducting chamber wall should be taken into account in the analysis. The image charges may reduce the LSC fields inside the beam and the associated LSC impedances compared with a beam in free space. This is the so-called shielding effect of the vacuum chamber.

The LSC field depends on not only the geometric configurations of the cross-sections of the beam-chamber system, but also the distributions of the beam profiles. Therefore, the space charge field models which are either exactly the same as or close to the real beam-chamber system are preferred in beam instability analysis. It is also highly

[1] [1] Y. Li, L. Wang, Nuclear Instruments and Methods in Physics Research A 747, 30 (2014).
[2] Y. Li, L. Wang, Nuclear Instruments and Methods in Physics Research A 769, 44 (2015).

desirable that the derived space charge fields and impedances are valid at any perturbation wavelengths. The coasting SIR beam is typically a long bunch with a roughly round cross-section; the vacuum chamber is roughly rectangular with large aspect ratio, which can also be simplified as a pair of infinitely large parallel plates (e.g., in the simulation code CYCO [12]). Unfortunately, at present, there are no ready-to-use LSC impedance formulae available for the SIR beam-chamber system in the existing literature, which satisfy the requirements of both the geometric configuration and the range of validity in perturbation wavelength. Beam physicists have to use other field models to approximate the LSC fields of SIR beam instead. For example, Pozdeyev [15] and Bi [16] use the LSC impedance formulae of a round beam in free space, and a round beam inside a round chamber to approximate the LSC impedances of SIR beam, respectively. The accuracies and range of validity of these models sometimes are questionable. Hence, derivations of more accurate analytical LSC impedance formulae for the SIR beam-chamber system become the major pursuits of this chapter.

First, this chapter summarizes the existing LSC field models and some popular methods for analytical derivations of the LSC impedances. Second, this chapter studies the LSC impedances of a *rectangular* beam with sinusoidal line charge density modulations inside a *rectangular* chamber, and between a pair of *parallel plates* as a limiting case. Third, based on the rectangular beam model, this chapter continues to derive the approximate analytical LSC impedances of a *round* beam with sinusoidal line density modulations under planar and rectangular boundary conditions, respectively. The derived analytical LSC impedances are valid at any perturbation wavelength and are consistent well with the numerical simulation results.

3.2 A summary of the existing LSC field models

Various space charge field models with different cross-sections of the beam and chamber have been investigated in existing literatures. For example, a round beam in free space [23-26], a round beam inside a round chamber [16, 24, 25, 27, 28], a round beam inside an elliptic chamber [29], a uniformly charged line between two parallel plates [30], a uniformly charged round beam between two parallel plates [31], a uniformly charged round beam inside a rectangular chamber [32], a rectangular beam inside a rectangular chamber [33-34], a rectangular beam between parallel plates [35], a single particle between parallel plates [36], a line charge inside rectangular chamber and between parallel plates [37], a vertical ribbon beam between parallel plates [38], etc.

The above-mentioned models are either not for a round beam, or/and not for a rectangular chamber (or between parallel plates), or/and not valid at any perturbation wavelengths. To our knowledge, at present, there are no analytical LSC impedance formulae available in modern publications for a round beam inside a straight rectangular chamber (or between parallel plates) which are valid in the entire wavelength spectrum.

3.3 Review of analytical methods for derivation of the LSC fields

Some (not all) popular methods are used to calculate the analytical LSC fields.

(a) Faraday's law and rectangular integration loop [21, 32]. This method is only valid in the long-wavelength limits. When the charge density modulation wavelength λ is small, the electric fields at the off-axis field points have both normal and skew components with respect to the beam axis. The three-dimensional (3D) effects of the electric fields become

important making this method invalid.

(b) Direct integration methods. Usually the direct integration methods are only applicable to the field models with simple charge distributions in free space. Some literatures use this method to calculate the LSC fields assuming the gradient of the charge density $d\Lambda/dz$ is independent of the longitudinal coordinate z and is put outside of the integral over z (e.g., Refs. [21, 35]). In fact, this assumption is invalid for a beam with short-wavelength density modulations (e.g., $\Lambda(z) = \Lambda_k\cos(kz)$, where $k=2\pi/\lambda$). Thus the results are only valid in the long-wavelength limits too.

(c) Separation of variables. In some special cases, the exact analytical 3D space charge fields of a beam with sinusoidal longitudinal charge density modulations can be solved by the method of separation of variables, such as a round beam in free space and inside a round chamber [16, 23, 27]. The 3D space charge fields solved by this method are exact and valid in the whole spectrum of perturbation wavelengths. But this method is critical of the configurations of the cross-sectional geometry of the beam-chamber system. Hence, it is not applicable to all field models.

(d) Image method. According to the superposition theorem of the electric fields, the space charge field of a beam is equal to the sum of the direct self-field in free space (open boundary) and its image fields. If these fields can be calculated separately, it is easy to obtain the total LSC field and impedance.

3.4 LSC impedances of a rectangular beam inside a rectangular chamber and between parallel plates

By separation of variables technique, this section will derive the LSC impedance for a field model consisting of a rectangular beam with sinusoidal line charge density

modulations under two boundary conditions: (a) inside a rectangular vacuum chamber, and (b) between parallel plates. The results are valid at any perturbation wavelengths.

3.4.1 Field model of a rectangular beam inside a rectangular chamber

The geometry of the cross-section of the field model is shown in Figure 3.1. The beam and the chamber are coaxial with the axes located at (w, 0). The full width and height of the inner boundary of the chamber are $2w$ and $2h$, respectively. The full width and height of the beam are $2a$ and $2b$, respectively. The horizontal beam dimension $2a$ is variable and can be as wide as the full chamber width $2w$.

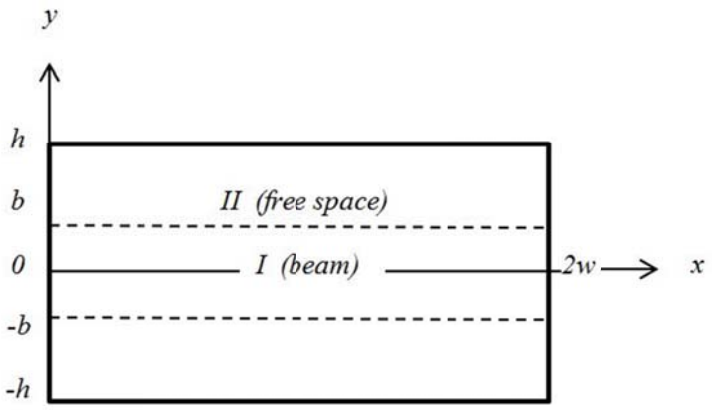

Figure 3.1: A rectangular beam inside a rectangular chamber.

Assume the vertical particle distribution is uniform in the region of $-b \le y \le b$. For the longitudinal charge distributions along z-axis, since the unperturbed charge density Λ_0 does not affect the LSC fields, we can neglect this DC component.

In the *lab* frame, let us assume that the line charge density and beam current have sinusoidal modulations along the longitudinal coordinate z, and can be written in the form of propagating waves as

$$\Lambda(z,t) = \Lambda_k \exp[i(kz - \omega t)], \qquad I(z,t) = I_k \exp[i(kz - \omega t)], \tag{3.1}$$

respectively, where Λ_k and I_k are the amplitudes, $I_k = \Lambda_k \beta c$, β is the relativistic speed of the beam, c is the speed of light in free space, ω is the angular frequency of the perturbations, k is the wave number of the line charge density modulations. In order to calculate the LSC fields inside the beam in the *lab* frame, first, we can calculate the electrostatic potentials and fields in the *rest* frame of the beam, and then convert them into the *lab* frame by Lorentz transformation.

In the *rest* frame, the line charge density of a beam can be simplified as

$$\Lambda'(z') = \Lambda'_k \cos(k'z'), \tag{3.2}$$

where the symbol prime stands for the *rest* frame.

For general purpose, we assume there are no restrictions for the horizontal beam distributions within the chamber. If the dependence of the perturbed volume charge density $\rho'(x', y', z')$ on x' in the *rest* frame can be described by a function of $G(x')$, then

$$\rho'(x', y', z') = \begin{cases} \dfrac{\Lambda'_k \cos(k'z')}{2b} G(x'), & |\, y' \,| \le b. \\ 0, & b < |\, y' \,| \le h. \end{cases} \tag{3.3}$$

where $G(x')$ satisfies the normalization condition of

$$\int_0^{2w} G(x')dx' = 1, \tag{3.4}$$

and the volume charge density correlates with the line charge density

$$\int_{-h}^{h} dy' \int_0^{2w} \rho'(x', y', z')dx' = \Lambda'(z'). \tag{3.5}$$

In order to solve the Poisson equation in the Cartesian coordinate system analytically

and conveniently using the method of separation of variables, the normalized horizontal distribution function $G(x')$ can be written as a Fourier series. Since the charge must vanish on the chamber side walls at $x' = 0$ and $x' = 2w$, we can expand $G(x')$ to a sinusoidal series

$$G(x') = \frac{1}{2w}\sum_{n=1}^{\infty} g'_n \sin(\eta_n x'), \tag{3.6}$$

$$\eta_n = \frac{n\pi}{2w}. \tag{3.7}$$

The dimensionless Fourier coefficient g'_n can be calculated by

$$g'_n = 2\int_0^{2w} G(x')\sin(\eta_n x')dx'. \tag{3.8}$$

From Eq. (3.3) and Eq. (3.6), the volume charge density in the *rest* frame can be expressed as

$$\rho'(x',y',z') = \begin{cases} \dfrac{\Lambda'_k \cos(k'z')}{4bw}\displaystyle\sum_{n=1}^{\infty} g'_n \sin(\eta_n x'), & |\, y' \,| \le b, \\ 0, & b < |\, y' \,| \le h. \end{cases} \tag{3.9}$$

3.4.2 Calculation of the space charge potentials and fields

In Region I (charge region) and Region II (charge free region), the electrostatic space charge potentials $\varphi'_I(x',y',z')$ and $\varphi'_{II}(x',y',z')$ in the *rest* frame satisfy the Poisson equation and Laplace equation, respectively. Then we have

$$\left(\frac{\partial^2}{\partial x'^2} + \frac{\partial^2}{\partial y'^2} + \frac{\partial^2}{\partial z'^2}\right)\varphi'_I(x',y',z') = -\frac{\Lambda'_k \cos(k'z')}{4\varepsilon_0 bw}\sum_{n=1}^{\infty} g'_n \sin(\eta_n x'), \tag{3.10}$$

$$(\frac{\partial^2}{\partial x'^2}+\frac{\partial^2}{\partial y'^2}+\frac{\partial^2}{\partial z'^2})\varphi'_{II}(x',y',z')=0, \tag{3.11}$$

where $\varepsilon_0 = 8.85\times10^{-12}$ F/m is the permittivity in free space.

The basic components of the solutions to Eq. (3.11) and the homogeneous form of Eq. (3.10) can be written as

$$\varphi'_h = X(x')Y(y')\cos(k'z'). \tag{3.12}$$

The possible configurations of the solutions to $X(x')$ and $Y(y')$ may have the forms of

$$X(x') \sim \cos(\eta_n x'), \sin(\eta_n y') \quad \text{or their combinations,} \tag{3.13}$$

and

$$Y(y') \sim \cosh(v'_n y'), \sinh(v'_n y') \quad \text{or their combinations,} \tag{3.14}$$

respectively, where

$$v'^2_n = \eta^2_n + k'^2, \qquad n=1, 2, 3 \ldots\ldots \tag{3.15}$$

Considering the boundary conditions (a) $\varphi' = 0$, $E'_y = 0$ at $x' = 0, 2w$; (b) $\varphi' = 0$, $E'_x = 0$ at $y'=\pm h$, and the potential $\varphi'(x', y', z')$ should be even functions of y', the basic components of solutions to Eq. (3.11) and the homogeneous form of Eq. (3.10) may have the following forms:

In region I (charge region): $$\varphi'_{h,I} \sim \sin(\eta_n x')\cosh(v'_n y')\cos(k'z'), \tag{3.16}$$

In region II (charge free region): $$\varphi'_{h,II} \sim \sin(\eta_n x')\sinh[v'_n(h-|y'|)]\cos(k'z'). \tag{3.17}$$

The particular solution to the inhomogeneous Eq. (3.10) can be written as

$$\varphi'_{i,I}(x',y',z') = \cos(k'z')\sum_{n=1}^{\infty} C'_n \sin(\eta_n x'). \tag{3.18}$$

Plugging Eq. (3.18) into Eq. (3.10) and comparing the coefficients of the like terms of the two sides gives the coefficients C'_n

$$C'_n = \frac{\Lambda'_k g'_n}{4\varepsilon_0 b w {v'_n}^2}. \tag{3.19}$$

Then in region I (charge region), the field potentials in the *rest* frame are

$$\varphi'_I(x',y',z') = \varphi'_{h,I} + \varphi'_{i,I} = \cos(k'z')\sum_{n=1}^{\infty} \sin(\eta_n x')[A'_n \cosh(v'_n y') + C'_n]. \tag{3.20}$$

In region II (charge free region), the field potentials in the *rest* frame are

$$\varphi'_{II}(x',y',z') = \cos(k'z')\sum_{n=1}^{\infty} B'_n \sin(\eta_n x')\sinh[v'_n(h-|y'|)]. \tag{3.21}$$

The boundary conditions between Region I and Region II are: at $y'=\pm b$, $\varphi'_I = \varphi'_{II}$, $\partial\varphi'_I/\partial y' = \partial\varphi'_{II}/\partial y'$. Then the coefficients A'_n and B'_n can be determined as

$$A'_n = -\frac{\cosh[v'_n(h-b)]}{\cosh(v'_n h)} C'_n, \qquad B'_n = \frac{\sinh(v'_n b)}{\cosh(v'_n h)} C'_n. \tag{3.22}$$

Finally, the space charge potentials in the *rest* frame are

(a) In region I (charge region), $0 \le |y'| \le b$,

$$\varphi'_I(x',y',z') = \frac{\Lambda'_k \cos(k'z')}{4\varepsilon_0 b w}\sum_{n=1}^{\infty}\frac{g'_n}{{v'_n}^2}\sin(\eta_n x')\{1-\frac{\cosh[v'_n(h-b)]}{\cosh(v'_n h)}\cosh(v'_n y')\}. \tag{3.23}$$

(b) In region II (charge free region), $b<|y'|\le h$,

$$\varphi'_{II}(x',y',z') = \frac{\Lambda'_k \cos(k'z')}{4\varepsilon_0 b w}\sum_{n=1}^{\infty}\frac{g'_n}{{v'_n}^2}\frac{\sinh(v'_n b)}{\cosh(v'_n h)}\sin(\eta_n x')\sinh[v'_n(h-|y'|)]. \tag{3.24}$$

For a beam with rectangular cross-section and uniform transverse charge density, the volume charge density in the *rest* frame can be expressed as

$$\rho'(x',y',z')=\begin{cases}\dfrac{\Lambda'_k}{4ab}\cos(k'z'), & w-a\le x'\le w+a,|\,y'\,|\le b.\\ 0, & x'<w-a,x'>w+a,b\lhd|\,y'\,|\le h.\end{cases} \tag{3.25}$$

Comparing Eq. (3.25) with Eq. (3.3) gives $G(x')$ is equal to $1/2a$ inside the beam and 0 outside of the beam, respectively. Then g'_n can be calculated from Eq. (3.8) as

$$g'_n=\frac{2}{\eta_n a}\sin(\eta_n w)\sin(\eta_n a) \tag{3.26}$$

inside the beam and 0 outside of the beam, respectively.

According to Eq. (3.23), the LSC field inside the beam in the *rest* frame can be calculated as

$$E'_{z,l}(x',y',z')=-\frac{\partial\varphi'_l(x',y',z')}{\partial z'}=-\frac{\dfrac{d\Lambda'(z')}{dz'}}{4\varepsilon_0 bw}\sum_{n=1}^{\infty}\frac{g'_n}{\nu'^2_n}\sin(\eta_n x')\{1-\frac{\cosh[\nu'_n(h-b)]}{\cosh(\nu'_n h)}\cosh(\nu'_n y')\}. \tag{3.27}$$

According to the theory of relativity, the relations of parameters between the *rest* frame and the *lab* frame are

(a) The longitudinal electric field is invariant, i.e.,

$$E'_{z,l}=E_{z,l}, \tag{3.28}$$

(b) The wave number $$k'=k/\gamma, \tag{3.29}$$

(c) The coordinates $$x'=x,\quad y'=y,\quad z'=\gamma(z-\beta ct), \tag{3.30}$$

(d) The line charge density amplitude

$$\Lambda'_k=\Lambda_k/\gamma, \tag{3.31}$$

(e) $$\nu_n'^2 = \eta_n^2 + k'^2 = \eta_n^2 + \frac{k^2}{\gamma^2}, \tag{3.32}$$

(f) $$\frac{d\Lambda'(z')}{dz'} = -k'\Lambda_k' \sin(k'z') = -\frac{k\Lambda_k}{\gamma^2}\sin(kz - \omega t). \tag{3.33}$$

If we choose exponential representation as used in Eq. (3.1), then Eq. (3.33) can also be expressed as

$$\frac{d\Lambda'(z')}{dz'} = \frac{1}{\gamma^2}\frac{\partial\Lambda(z,t)}{\partial z}, \tag{3.34}$$

where γ is the relativistic factor. Then the LSC field in the *lab* frame becomes

$$E_{z,l}(x,y,z,t) = -\frac{\frac{\partial\Lambda(z,t)}{\partial z}}{4\varepsilon_0 bw\gamma^2}\sum_{n=1}^{\infty}\frac{g_n}{\nu_n^2}\sin(\eta_n x)\{1 - \frac{\cosh[\nu_n(h-b)]}{\cosh(\nu_n h)}\cosh(\nu_n y)\}, \tag{3.35}$$

where

$$g_n = g_n' = \frac{2}{\eta_n a}\sin(\eta_n w)\sin(\eta_n a), \tag{3.36}$$

$$\nu_n^2 = \nu_n'^2 = \eta_n^2 + k'^2 = \eta_n^2 + \frac{k^2}{\gamma^2}. \tag{3.37}$$

3.4.3 LSC impedances

The average LSC field over the cross-section of the beam at z and time t is

$$< E_{z,l}(z,t) > = \frac{1}{4ab}\int_{-b}^{b} dy \int_{w-a}^{w+a} E_{z,l}(x,y,z,t)dx$$

$$= -\frac{\frac{\partial\Lambda(z,t)}{\partial z}}{4\varepsilon_0 bw\gamma^2}\sum_{n=1}^{\infty}\frac{g_n}{\nu_n^2} < \sin(\eta_n x) > \{1 - \frac{\cosh[\nu_n(h-b)]}{\cosh(\nu_n h)} < \cosh(\nu_n y) >\}, \tag{3.38}$$

where

$$< \sin(\eta_n x) >= \frac{1}{2a} \int_{w-a}^{w+a} \sin(\eta_n x) dx = \frac{1}{2} g_n, \tag{3.39}$$

$$< \cos(\nu_n y) >= \frac{1}{2b} \int_{-b}^{b} \cosh(\nu_n y) dy = \frac{1}{b\nu_n} \sinh(\nu_n b). \tag{3.40}$$

Finally, the average LSC fields in the beam region can be expressed as

$$< E_{z,I}(z,t) >= -\frac{1}{4\varepsilon_0 b w \gamma^2} \chi_{rect}(k) \frac{\partial \Lambda(z,t)}{\partial z}, \tag{3.41}$$

where

$$\chi_{rect}(k) = \sum_{n=1}^{\infty} \frac{g_n^{\ 2}}{2\nu_n^{\ 2}} \{1 - \frac{\cosh[\nu_n (h-b)]}{\nu_n b \cosh(\nu_n h)} \sinh(\nu_n b)\}. \tag{3.42}$$

The sum of the infinite series in Eq. (3.42) can be evaluated by truncating it to a finite number of terms, as long as the sum converges well.

The *average* energy loss per turn of a unit charge in a storage ring due to the *average* LSC field is

$$- < E_{z,I}(z,t) > C_0 = Z_{0,sc}^{\parallel}(k) I_k \exp[i(kz - \omega t)], \tag{3.43}$$

where C_0 is the circumference of the storage ring, $Z_{0,sc}^{\parallel}(k)$ is the LSC impedance of the rectangular beam inside the rectangular chamber. It is easy to obtain from Eqs. (3.1), (3.41) and (3.43) that the LSC impedance (Ω) is

$$Z_{0,rect,rect}^{\parallel}(k) = i \frac{Z_0 C_0 k}{4\beta b w \gamma^2} \chi_{rect,\ rect}(k), \tag{3.44}$$

where Z_0 = 377 Ω is the impedance of free space, R is the average radius of the storage

ring. If the impedance is evaluated by the LSC fields on the beam axis (w, 0), since in Eq. (3.35), $\sin(\eta_n x)= \sin(n\pi/2)$, $\cosh(\nu_n y)=1$, then $\chi_{rect,rect}(k)$ in Eq. (3.42) should be replaced by

$$\chi_{rect,rect}^{axis}(k) = \sum_{n=1}^{\infty} \frac{g_n}{\nu_n^2} \sin(\frac{n\pi}{2}) \{1 - \frac{\cosh[\nu_n(h-b)]}{\cosh(\nu_n h)}\}. \tag{3.45}$$

For a special case of infinite h, i.e., the rectangular chamber becomes a pair of vertical parallel plates separated by $2w$, since when $h\to\infty$, the limit of $\cosh[\nu_n(h-b)]/\cosh(\nu_n h)$ approaches $\cosh(\nu_n b)-\sin(\nu_n b)$, the parameter $\chi_{rect,rect}(k)$ in Eq. (3.42) can be simplified as

$$\chi_{rect,vpp}(k) = \sum_{n=1}^{\infty} \frac{g_n^2}{2\nu_n^2} [1 - \frac{\cosh(\nu_n b) - \sinh(\nu_n b)}{\nu_n b} \sinh(\nu_n b)]. \tag{3.46}$$

Eqs. (3.44) and (3.46) give the LSC impedances of a rectangular beam between a pair of vertical parallel plates separated by $2w$. In Eq. (3.46), if b is infinite, i.e. a rectangular beam with infinite height between two vertical parallel plates, since the last part in the right hand side of Eq. (3.46) becomes zero, then

$$\chi_{rect,vpp}(k)\,|_{b=\infty} = \sum_{n=1}^{\infty} \frac{g_n^2}{2\nu_n^2}. \tag{3.47}$$

For a special case of $w\to\infty$, i.e., the rectangular chamber becomes a pair of horizontal parallel plates separated by $2h$, if we make exchanges $a\leftrightarrow b$, $w\leftrightarrow h$, it is easy to obtain its impedances from Eqs. (3.44) and (3.46) that

$$Z_{0,rect,hpp}^{\parallel}(k) = i\frac{Z_0 C_0 k}{4\beta a h \gamma^2} \chi_{rect,hpp}(k), \tag{3.48}$$

$$\chi_{rect,hpp}(k)=\sum_{n=1}^{\infty}\frac{g_{n,hpp}^{\ 2}}{2\nu_{n,hpp}^{\ 2}}[1-\frac{\cosh(\nu_{n,hpp}a)-\sinh(\nu_{n,hpp}a)}{\nu_{n,hpp}a}\sinh(\nu_{n,hpp}a)], \tag{3.49}$$

where
$$\eta_{n,hpp}=\frac{n\pi}{2h}, \tag{3.50}$$

$$\nu_{n,hpp}^{\ 2}=\eta_{n,hpp}^{\ 2}+\frac{k^2}{\gamma^2}, \qquad \text{n=1, 2, 3 ……,} \tag{3.51}$$

$$g_{n,hpp}=\frac{2}{\eta_{n,hpp}b}\sin(\eta_{n,hpp}h)\sin(\eta_{n,hpp}b). \tag{3.52}$$

Eqs. (3.48)-(3.52) give the LSC impedances of a rectangular beam between a pair of horizontal parallel plates separated by $2h$. In Eq. (3.49), if $a \to \infty$, i.e. a rectangular beam with infinite width between two horizontal parallel plates, since the limit of $[\cosh(\nu_{n,hpp}a)\text{-}\sinh(\nu_{n,hpp}a)]\sinh(\nu_{n,hpp}a)/\nu_{n,hpp}a \to 0$, then

$$\chi_{rect,hpp}(k)\,|_{a=\infty}=\sum_{n=1}^{\infty}\frac{g_{n,hpp}^{\ 2}}{2\nu_{n,hpp}^{\ 2}}. \tag{3.53}$$

3.4.4 Case studies of the LSC impedances

In this subsection, we will calculate the LSC impedances of SIR beam by both analytical formulae and numerical method.

Lanfa Wang of Stanford Linear Accelerator Center (SLAC) developed a simulation code that can solve the Poisson equation numerically based on the Finite Element Method (FEM) [39]. The code can be used to calculate the space charge potentials, fields and impedances of the beam-chamber system with any configurations of the charge distributions and boundary shapes. In the *rest* frame, assume the harmonic volume charge density can be written as product of the transverse and longitudinal components

$$\rho'(x', y', z') = \rho'_{\perp}(x', y')\Lambda'(z') = \rho'_{\perp}(x', y')\Lambda'_k e^{ik'z'}, \tag{3.54}$$

where $\int \rho'_{\perp}(x', y')dx'dy' = 1$. Similarly, the potential due to the harmonic charge density is written as

$$\varphi'(x', y', z') = \varphi'_{\perp}(x', y')e^{ik'z'}. \tag{3.55}$$

The Poisson equation with Eqs. (3.54) and (3.55) becomes

$$(\nabla'^2_{\perp} - k'^2)\varphi'_{\perp} = -\Lambda'_k \frac{\rho'_{\perp}(x', y')}{\varepsilon_0}, \tag{3.56}$$

where $\nabla'^2_{\perp} = \partial^2/\partial x'^2 + \partial^2/\partial y'^2$ and $\varphi'_{\perp} = 0$ on the metal boundary. The potentials given by Eq. (3.56) with arbitrary beam and chamber shapes can be solved using the FEM. The whole domain is first divided into many small element regions (finite element). For each element, the strong form of the Poisson equation Eq. (3.56) can be rewritten as the FEM equation

$$\mathbf{M}\varphi'_{\perp} + k'^2\mathbf{B} = \mathbf{Q}, \tag{3.57}$$

where

$$M_{ij}^e = \iint_{S^e} \left(\frac{\partial N_i}{\partial x'}\frac{\partial N_j}{\partial x'} + \frac{\partial N_i}{\partial y'}\frac{\partial N_j}{\partial y'} \right) dx'dy', \tag{3.58}$$

$$B_i^e = \iint_{S^e} N_i N_j dx' dy', \tag{3.59}$$

$$Q_i^e = \frac{q_i}{\varepsilon_0}. \tag{3.60}$$

Here $N(x', y')$ is called the shape function in FEM, by which the potentials at a field point $P(x', y')$ within an element can be interpolated by the potentials of its neighboring nodes. $N(x', y')$ is related to the coordinates of the field point $P(x', y')$ and the nodes of the

element region. $\boldsymbol{M}$ is the stiffness matrix with matrix element $M_{i,j}^{e}$, i and j are the node indices of the finite element, S^e is the integration boundary of the finite element, q_i is the charge at the node i, which is proportional to the harmonic line charge density amplitude Λ'_k. The $\varphi'_\perp$ of Eq. (3.57) at all nodes satisfying equations Eqs. (3.57)-(3.60) and the boundary condition $\varphi'_\perp = 0$ on the chamber wall can be solved numerically. Then the total potentials in the *rest* frame can be calculated from Eq. (3.55), the corresponding LSC fields and impedances in the *lab* frame can be calculated using the similar procedures in Sect. 3.4.3.

Now we can use the rectangular beam and chamber model to estimate the LSC impedances of the coasting H_2^+ beam in the Small Isochronous Ring (SIR) at Michigan State University (MSU) [12]. The ring circumference is $C_0 = 6.58$ m, the kinetic energy of the beam is E_k=20 keV ($\beta \approx 0.0046$, $\gamma \approx 1.0$), the cross-section of the vacuum chamber is rectangular with w=5.7 cm, h=2.4 cm, the real beam is approximately round with radius r_0=0.5 cm. We can use a square beam model with a=b=r_0=0.5 cm to mimic the round beam.

Figure 3.2 shows the comparisons of the *on-axis* and *average* LSC impedances of SIR beam between the theoretical calculations and numerical simulations using a square beam model. We can see that the theoretical and simulated impedances match quite well. Note that the *on-axis* LSC impedances are higher than the averaged ones. The former may overestimate the LSC effects. For this reason, we only plot the average LSC impedances in Figures 3.3-3.9.

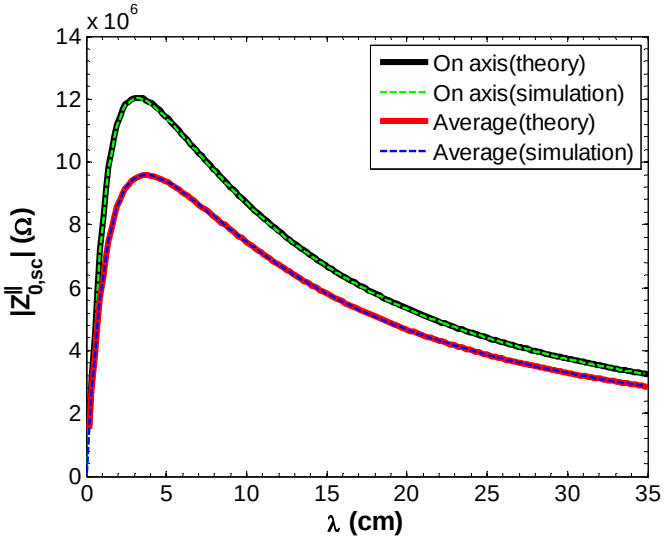

Figure 3.2: Comparisons of the *on-axis* and *average* LSC impedances between the theoretical calculations and numerical simulations for a beam model of square cross-section inside rectangular chamber with w = 5.7 cm, h =2.4 cm, a = b = 0.5 cm.

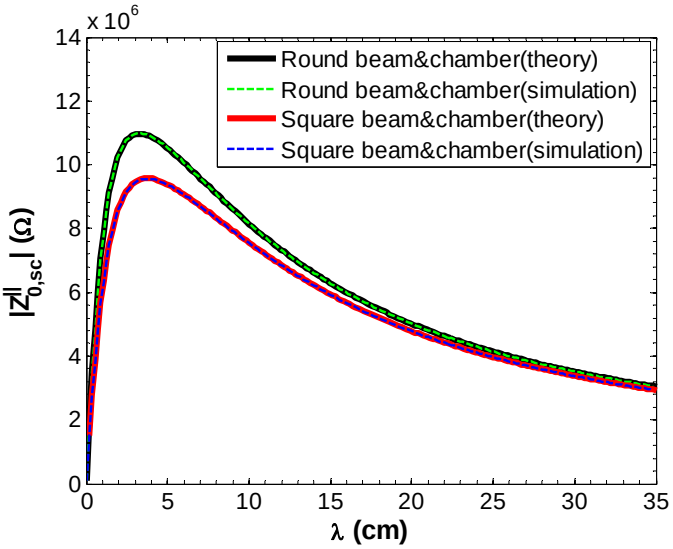

Figure 3.3: Comparisons of the LSC impedances between the square and round models (w=h =r_w =3.0 cm, a=b=r_0 =0.5 cm).

Figure 3.3 shows the comparisons of the LSC impedances between the square and round field models. The LSC impedances of a round beam of radius r_0 inside a round chamber of radius r_w can be derived from Ref. [16] as

$$Z^{\parallel}_{0,round,round}(\bar{k}) = i\frac{Z_0 C_0 \bar{k}}{\beta\pi\gamma}\chi_{round,round}(\bar{k}), \tag{3.61}$$

where
$$\chi_{round,round}(\bar{k}) = \frac{1}{(\bar{k}r_0)^2} - \frac{<I_0(\bar{k}r)>}{\bar{k}r_0 I_0(\bar{k}r_w)}[K_1(\bar{k}r_0)I_0(\bar{k}r_w) + K_0(\bar{k}r_w)I_1(\bar{k}r_0)], \tag{3.62}$$

$I_0(x)$, $I_1(x)$, $K_0(x)$, and $K_1(x)$ are the modified Bessel functions, $\bar{k} = k/\gamma$ and

$$< I_0(\bar{k}r) >= \frac{1}{\pi r_0^2}\int_0^{2\pi} d\theta \int_0^{r_0} I_0(\bar{k}r) r dr = \frac{2I_1(\bar{k}r_0)}{\bar{k}r_0}. \tag{3.63}$$

The parameters used in the calculations are w=h=r_w =3.0 cm, a=b=r_0 =0.5 cm. We can observe that the model with square beam and chamber shapes has lower LSC impedances compared with the round ones. At large perturbation wavelengths, the impedances of the two field models are close to each other.

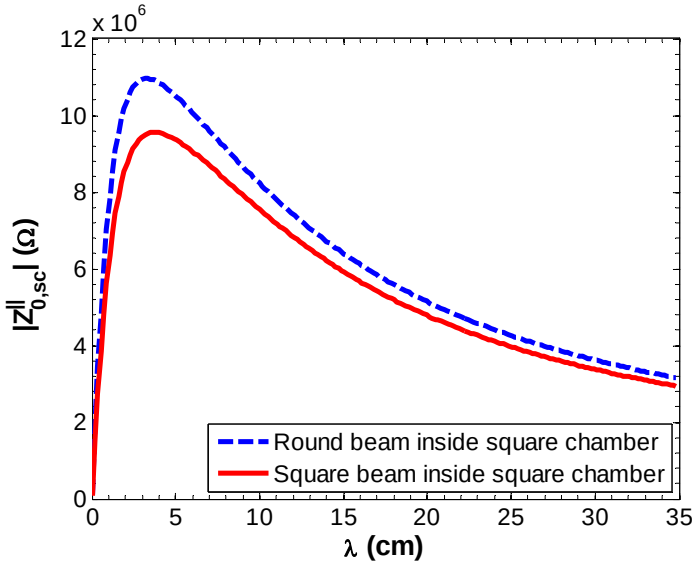

Figure 3.4: Simulated LSC impedances of the *square* and *round* beam models in a *square* chamber (w = h =3.0 cm, a = b = r_0 = 0.5 cm), respectively.

Figure 3.4 shows the simulated LSC impedances of the *square* and *round* H_2^+ beam of 20 keV inside a same *square* chamber. The parameters used in the calculations are w=h =3.0 cm, a=b=r_0 =0.5 cm. We can observe that the square beam has relatively lower LSC impedances than the round beam. The difference of impedances is caused by the different beam shapes. At large perturbation wavelengths, the LSC impedances of the two field models are close to each other.

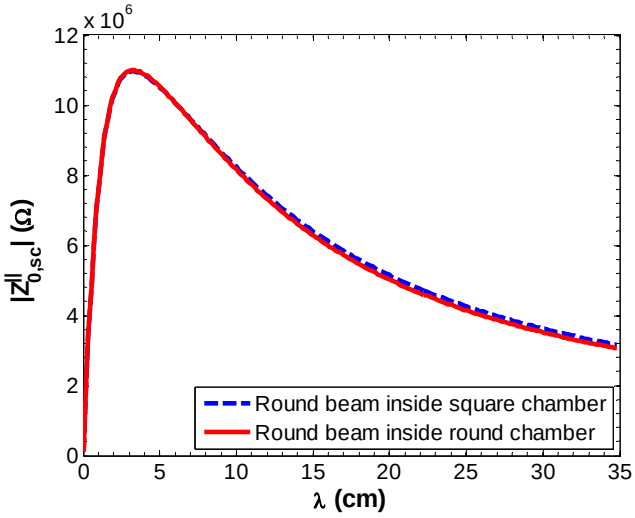

Figure 3.5: Simulated LSC impedances of a *round* beam inside *square* and round chambers ($w = h = r_w = 3.0$ cm, $r_0 = 0.5$ cm), respectively.

Figure 3.5 shows the simulated LSC impedances of a *round* H_2^+ beam of 20 keV inside the *round* and *square* chambers, respectively. The parameters used in the calculations are w=h=r_w=3.0 cm, r_0 =0.5 cm. We can observe that the two curves are close to each other, and the *square* chamber model has relatively higher LSC impedances than the *round* chamber model. The reason for this tiny difference is that the four corners of the square chamber are relatively farther away from the beam axis compared with a round chamber inscribing the square chamber, thus the shielding effects of the square chamber due to

image charges are weaker, and therefore the LSC field becomes stronger. At large perturbation wavelengths, the impedances of the two field models are close to each other. Figures 3.3-3.5 show that the lower impedances of the rectangular beam and chamber model in Figure 3.3 mainly originate from the different beam shapes rather than the chamber shapes.

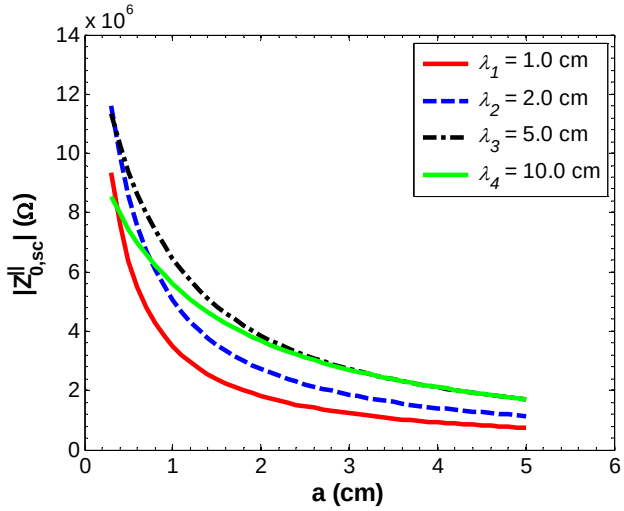

Figure 3.6: LSC impedances of *rectangular* beam model with different half widths *a* inside a *rectangular* chamber (w = 5.7 cm, h = 2.4 cm, a is variable, b = 0.5 cm).

Figure 3.6 shows the calculated LSC impedances of four perturbation wavelengths for a 20 keV H_2^+ beam model with *rectangular* cross-section inside the *rectangular* chamber of SIR. The parameters used in the calculations are w = 5.7 cm, h = 2.4 cm, b = 0.5 cm, the half beam width a is variable. We can see the LSC impedances decrease with beam width $2a$ for a fixed beam height $2b$.

Figure 3.7 shows the calculated LSC impedances of four perturbation wavelengths for a 20 keV H_2^+ beam model with *rectangular* cross-section inside a *rectangular* chamber of SIR. The parameters used in the calculations are w = 5.7 cm, h = 2.4 cm, a = 0.5 cm, the

half beam height b is variable. We can see the LSC impedances decrease with beam height $2b$ for a fixed beam width $2a$.

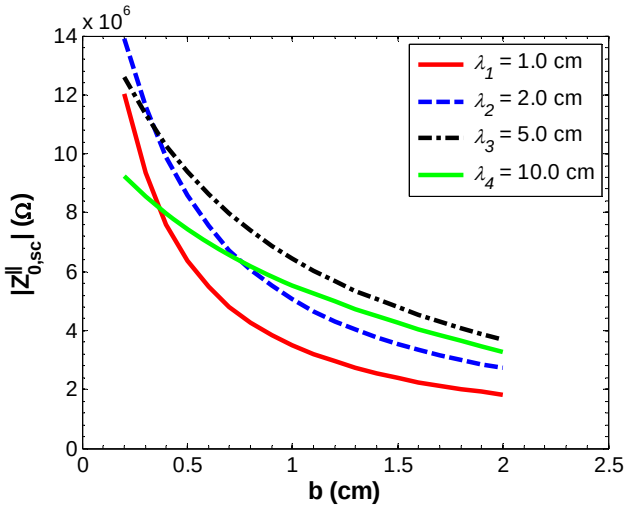

Figure 3.7: LSC impedances of a *rectangular* beam model with different half heights b inside *rectangular* chamber (w = 5.7 cm, h = 2.4 cm, a = 0.5 cm, b is variable).

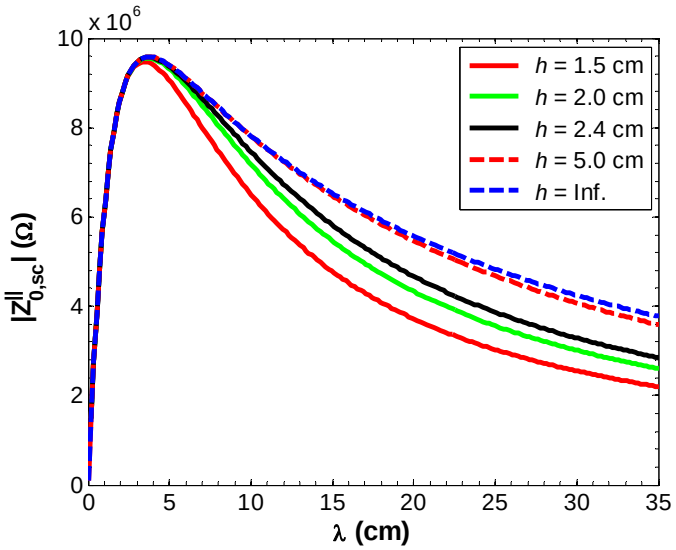

Figure 3.8: LSC impedances of *square* beam model inside *rectangular* chamber (w = 5.7 cm, h is variable, $a = b$ = 0.5 cm).

Figure 3.8 shows the calculated LSC impedances of a 20 keV H_2^+ beam model with *square* cross-section inside a *rectangular* chamber of SIR. The parameters used in the calculations are w = 5.7 cm, a = b = 0.5 cm, the half chamber height h is variable. For short wavelengths λ < 5.0 cm, the LSC impedances are almost independent of the changes of h. For longer wavelengths λ > 5.0 cm, when h > 5.0 cm, the impedances are insensitive to the changes of h and are close to the limiting case of $h = \infty$ (vertical parallel plates).

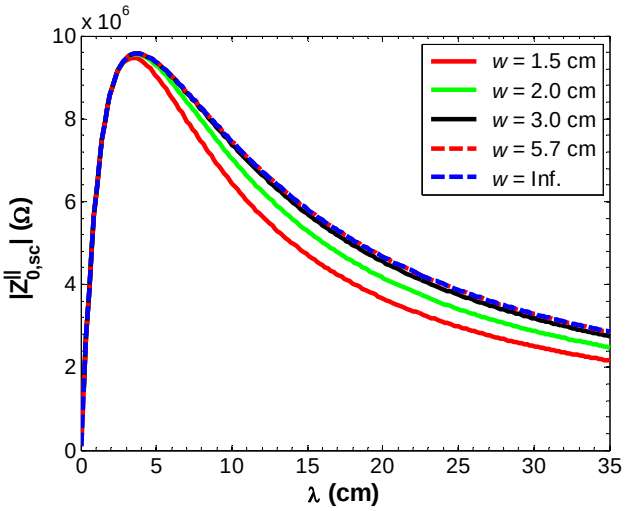

Figure 3.9: LSC impedances of a *square* beam model inside a *rectangular* chamber (w is variable, h = 2.4 cm, a = b = 0.5 cm).

Figure 3.9 shows the calculated LSC impedances of a 20 keV H_2^+ beam model with *square* cross-section inside a *rectangular* chamber of SIR. The parameters used in the calculations are h = 2.4 cm, a = b = 0.5 cm, the half chamber width w is variable. For short wavelengths λ<5.0 cm, the LSC impedances are almost independent of the changes of w. For longer wavelengths λ>5.0 cm, when w > 3.0 cm, the impedances are insensitive to the changes of w and are close to the limiting case of $w = \infty$ (horizontal parallel plates).

3.4.5 Conclusions for the rectangular beam model

We introduced a 3D space charge field model of *rectangular* cross-section to calculate the perturbed potentials, fields and the associated LSC impedances. The calculated LSC impedances are consistent well with the numerical simulation results. A rectangular beam shape with $a=b=r_0$ may help to reduce the LSC impedances compared with the conventional round beam with radius r_0. This result is consistent with Ref. [35] in which a planar geometry was investigated. For fixed b(or a), when a(or b) increases, the LSC impedance will decrease. The LSC impedances of a rectangular beam inside a pair of infinitely large parallel plates are also derived in this paper. Theoretical calculations demonstrate that, when the transverse chamber dimensions are approximately more than five times of the transverse beam dimensions, the rectangular chamber of the Small Isochronous Ring (SIR) can be approximated by a pair of parallel plates. This result validates the simplified boundary model of parallel plates used in the Particle-In-Cell (PIC) simulation code CYCO to simulate the rectangular chamber of SIR [12].

3.5 LSC impedances of a round beam inside a rectangular chamber and between parallel plates

This section presents the approximate analytical solutions to the LSC impedances of a round beam with uniform transverse distribution and sinusoidal line density modulations under two boundary conditions: (a) between parallel plates (b) inside a rectangular chamber, respectively. Since the transverse dimensions of almost all the beam chambers are much larger than the transverse beam size, the image charge fields of a round beam can be approximated by those of a line charge. Then the approximate LSC fields and

impedances of the two models in discussion can be calculated by image method.

In order to obtain the approximate analytical LSC impedances of a round beam with planar and rectangular boundary conditions, first, we need to know the LSC fields E_z of the following four component field models:

(a) A round beam in free space, $E_{z,round,fs}$.

(b) A line charge in free space, $E_{z,line,fs}$.

(c) A line charge between two parallel plates, $E_{z,line,pp}$.

(d) A line charge inside a rectangular chamber $E_{z,line,rect}$.

For a *round* beam between a pair of parallel plates, when the separation between the plates is much larger than the beam diameter, its image LSC fields can be approximated by those of a line charge between the parallel plates as $E^{image}_{z,roundpp} \approx E^{image}_{z,linepp} = E_{z,linepp} - E_{z,linefs}$, its total LSC fields are approximately equal to $E_{z,roundpp} = E_{z,roundfs} + E^{image}_{z,roundpp}$ $\approx E_{z,roundfs} + E^{image}_{z,linepp} = E_{z,roundfs} + E_{z,linepp} - E_{z,linefs}$; similarly, for a *round* beam inside a *rectangular* chamber, when the full chamber height is much larger than the beam diameter, its image LSC fields $E^{image}_{z,round,rect}$ and total LSC fields $E_{z,round,rect}$ can be approximated as $E^{image}_{z,roundrect} \approx E_{z,linerect} - E_{z,linefs}$ and $E_{z,roundrect} \approx E_{z,roundfs} + E_{z,linerect} - E_{z,linefs}$ respectively. Next, we will derive the LSC fields of the four component field models listed in (a)-(d).

3.5.1 A round beam in free space

In the *lab* frame, assume there is an infinitely long round beam of radius r_0 with sinusoidal line density Λ and beam intensity modulations I of

$$\Lambda(z,t) = \Lambda_k \exp[i(kz - \omega t)], \text{ and } \quad I(z,t) = I_k \exp[i(kz - \omega t)], \tag{3.64}$$

respectively. According to Ref. [26], its LSC field in the *lab* frame is

$$E_{z,round,fs}(r,z,t) = -\frac{1}{\pi\varepsilon_0 r_0^{\,2}\bar{k}^2\gamma^2}\frac{\partial\Lambda(z,t)}{\partial z}[1 - K_1(\bar{k}r_0)I_0(\bar{k}r)]. \tag{3.65}$$

where $\varepsilon_0 = 8.85\times10^{-12}$ F m^{-1} is the permittivity in free space, $\bar{k} = k/\gamma$, γ is the relativistic factor, $I_0(x)$ and $K_1(x)$ are the modified Bessel functions of the first and second kinds, respectively.

3.5.2 A line charge in free space

In the *lab* frame, assume there is an infinitely long line charge in free space with sinusoidal line charge density and beam intensity modulations described in Eq. (3.64). First, we can calculate its potentials and fields in the *rest* frame of the beam, and then convert them into the *lab* frame by Lorentz transformation. In the *rest* frame of the beam, the line charge density is

$$\Lambda'(z') = \Lambda'_k \cos(k'z'), \tag{3.66}$$

where the parameters with primes stand for those in the *rest* frame. The electrostatic potentials can be calculated easily in cylindrical coordinate system by direct integration as

$$\varphi'_{line,fs}(r',z') = \frac{\Lambda'_k}{4\pi\varepsilon_0}\int_{-\infty}^{\infty}\frac{\cos(k'\bar{z}')}{[(\bar{z}'-z')^2+r'^2]^{\frac{1}{2}}}d\bar{z}' = \frac{\Lambda'(z')}{2\pi\varepsilon_0}K_0(k'r'). \tag{3.67}$$

The LSC field in the *rest* frame is

$$E'_{z,line,fs}(r',z') = -\frac{1}{2\pi\varepsilon_0}\frac{d\Lambda'(z')}{dz'}K_0(k'r'). \tag{3.68}$$

In the *lab* frame, according to the theory of relativity, we have

$$E'_z = E_z, \tag{3.69}$$

$$r' = r, \tag{3.70}$$

$$z' = \gamma(z-\beta ct), \tag{3.71}$$

$$\Lambda'_k = \Lambda_k/\gamma, \tag{3.72}$$

$$k' = \frac{k}{\gamma} = \bar{k}, \tag{3.73}$$

$$\frac{d\Lambda'(z')}{dz'} = -k'\Lambda'_k\sin(k'z') = -\frac{k\Lambda_k}{\gamma^2}\sin(kz-\omega t). \tag{3.74}$$

If we choose exponential representation as used in Eq. (3.64), then Eq. (3.74) can also be expressed as

$$\frac{d\Lambda'(z')}{dz'} = \frac{1}{\gamma^2}\frac{\partial\Lambda(z,t)}{\partial z}. \tag{3.75}$$

From Eqs. (3.68)-(3.75), the LSC fields in the *lab* frame become

$$E_{z,line,fs}(r,z,t) = -\frac{1}{2\pi\varepsilon_0\gamma^2}\frac{\partial\Lambda(z,t)}{\partial z}K_0(\bar{k}r). \tag{3.76}$$

3.5.3 A line charge between parallel plates

The schematic view of an infinitely long line charge between two infinitely large, perfectly conducting parallel plates is shown in Figure 3.10. Its sinusoidal line charge density and beam intensity modulations are described by Eq. (3.64).

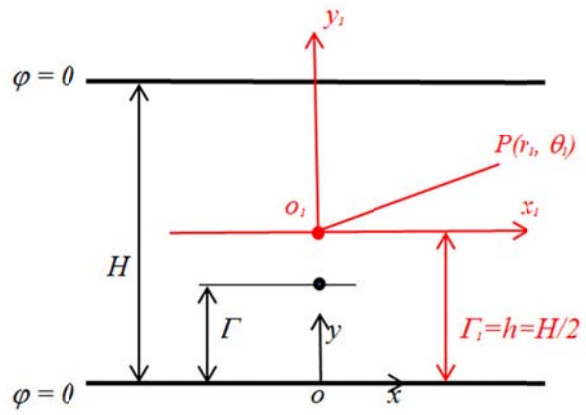

Figure 3.10: A line charge with sinusoidal density modulations between parallel plates.

Assume the two plates are separated by a distance H, the line charge is parallel to the plates and its distance to the lower plate is Γ, the potentials on the two plates are all 0. Though Ref. [37] provided solutions to the LSC fields and impedances of a line charge between parallel plates and inside a rectangular chamber, the field potential is solved by 2D Green function neglecting the 3D effects caused by the line density modulations. Hence, the results are only valid in the long-wavelength limits. Ref. [40] solved the 2D electrostatic potentials of a uniform line charge between two parallel plates using the method of separation of variables. We can use the same method and similar procedures to solve the 3D fields of our model. We choose the Cartesian coordinate *xoy* with *o* as the origin. Assume in the *rest* frame of the beam, the basic harmonic component of the space

charge potential can be written in the form

$$\varphi'_{line,pp}(x',y',z') = X(x')Y(y')\cos(k'z'), \tag{3.77}$$

which satisfies the Laplace equation

$$\frac{\partial^2\varphi'_{line,pp}}{\partial x'^2} + \frac{\partial^2\varphi'_{line,pp}}{\partial y'^2} + \frac{\partial^2\varphi'_{line,pp}}{\partial z'^2} = 0. \tag{3.78}$$

Plugging Eq. (3.77) into Eq. (3.78) results in

$$\frac{1}{X}\frac{d^2X}{dx'^2} + \frac{1}{Y}\frac{d^2Y}{dy'^2} = k'^2. \tag{3.79}$$

Considering the boundary conditions $\varphi'_{line,pp}(y' = 0) = \varphi'_{line,pp}(y' = H) = \varphi'_{line,pp}(x' = \pm\infty) = 0$, we can choose

$$\frac{1}{X}\frac{d^2X}{dx'^2} = k'^2 + \alpha^2, \qquad \frac{1}{Y}\frac{d^2Y}{dy'^2} = -\alpha^2, \tag{3.80}$$

where $\alpha > 0$. Then the solutions to Eq. (3.80) can be written as

$$X(x') = A'_1 e^{\sqrt{k'^2+\alpha^2}x'} + A'_2 e^{-\sqrt{k'^2+\alpha^2}x'}, \tag{3.81}$$

$$Y(y') = B'_1 \sin(\alpha y') + B'_2 \cos(\alpha y'). \tag{3.82}$$

The boundary conditions $\varphi'_{line,pp}(y'=0) = \varphi'_{line,pp}(y'=H) = 0$ give $B'_2 = 0, \alpha = n\pi/H$, then $Y(y') \sim \sin(n\pi y'/H)$. Because at $x' = 0$, there is a line charge which produces singularity, we should calculate the electrostatic potentials $\varphi'_{line,pp,+}$ for $x' > 0$ and $\varphi'_{line,pp,-}$ for $x' < 0$ separately.

In Eq. (3.81), when $x' \to +\infty$, $\varphi'_{line,pp,+} \to 0$, then the coefficient $A'_{1+}=0$; when $x' \to -\infty$, $\varphi'_{line,pp,-} \to 0$, then the coefficient $A'_{2-}=0$. The solutions of X can be written as

$$X_{\pm}(x') = A'_{\pm} e^{\mp\sqrt{k'^2+\alpha^2}x'} \tag{3.83}$$

where '+' and '–' stand for $x>0$ and $x<0$, respectively.

The potentials including all harmonic components can be expressed as

$$\varphi'_{line,pp,\pm} = \sum_{n=1}^{\infty} C'_{n\pm} e^{\mp\sqrt{k'^2+\left(\frac{n\pi}{H}\right)^2}x'} \sin(\frac{n\pi}{H}y')\cos(k'z'), \tag{3.84}$$

where C'_{n+} and C'_{n-} are the coefficients to be determined by the boundary conditions for $x>0$ and $x<0$, respectively. At $x'=0$, $y' \neq \Gamma$, $\varphi'_{line,pp,+} = \varphi'_{line,pp,-}$ which gives $C'_{n+} = C'_{n-} = C'_n$. If the line charge is rewritten in the form of surface charge density

$$\sigma' = \Lambda'(z')\delta(y'-\Gamma), \tag{3.85}$$

where $\delta(x)$ is the Dirac Delta function, then on the plane $x' = 0$, the boundary condition $D_{2n}' - D_{1n}' = \sigma'$ gives

$$\varepsilon_0(\frac{\partial\varphi'_{\text{line,pp,-}}}{\partial x'} - \frac{\partial\varphi'_{line,pp,+}}{\partial x'})\,|_{x'=0} = \Lambda'_k \cos(k'z')\delta(y'-\Gamma). \tag{3.86}$$

Eqs. (3.84) and (3.86) give

$$\sum_{n=1}^{\infty} 2C'_n \sqrt{k'^2+\left(\frac{n\pi}{H}\right)^2} \sin(\frac{n\pi}{H}y') = \frac{\Lambda'_k}{\varepsilon_0}\delta(y'-\Gamma). \tag{3.87}$$

Multiplying the two sides of Eq. (3.87) by $\sin(n\pi y'/H)$ and integrating y' from 0 to H

gives the coefficient C_n'

$$C_n' = \frac{\Lambda_k'}{\varepsilon_0 H \sqrt{k'^2 + \left(\frac{n\pi}{H}\right)^2}} \sin(\frac{n\pi}{H}\Gamma). \tag{3.88}$$

Then the potentials in Eq. (3.84) can be expressed as

$$\varphi_{line,pp}'(x', y', z') = \frac{\Lambda'(z')}{\varepsilon_0 H} \sum_{n=1}^{\infty} \frac{1}{\sqrt{k'^2 + \left(\frac{n\pi}{H}\right)^2}} \sin(\frac{n\pi}{H}\Gamma) e^{-\sqrt{k'^2+\left(\frac{n\pi}{H}\right)^2}|x'|} \sin(\frac{n\pi}{H} y'). \tag{3.89}$$

Let's consider a special case of $\Gamma=\Gamma_1=h=H/2$, i.e., the line charge is on the median plane of the two plates as shown in Figure 3.10, if we choose a new coordinate system $x_1o_1y_1$ with o_1 as the origin (see Figure 3.10), according to $x' = x_1'$, $y' = y_1'+h$, the potentials in the *rest* frame of the beam become

$$\varphi_{line,pp}'(x_1', y_1', z') = \frac{\Lambda'(z')}{2\varepsilon_0 h} \sum_{n=1}^{\infty} \frac{1}{\sqrt{k'^2 + \left(\frac{n\pi}{2h}\right)^2}} \sin(\frac{n\pi}{2}) e^{-\sqrt{k'^2+\left(\frac{n\pi}{2h}\right)^2}|x_1'|} \sin[\frac{n\pi}{2h}(y_1' + h)]. \tag{3.90}$$

If we use cylindrical coordinate system, $x_1' = r'\cos(\theta')$, $y_1' = r'\sin(\theta')$, Eq. (3.90) becomes

$$\varphi_{line,pp}'(r', \theta', z') = \frac{\Lambda'(z')}{2\varepsilon_0 h} \sum_{n=1}^{\infty} \frac{1}{\sqrt{k'^2 + \left(\frac{n\pi}{2h}\right)^2}} \sin(\frac{n\pi}{2}) e^{-\sqrt{k'^2+\left(\frac{n\pi}{2h}\right)^2} r'|\cos(\theta')|} \sin[\frac{n\pi}{2h}(r'\sin(\theta') + h)]. \tag{3.91}$$

The LSC field in the *rest* frame is

$$E'_{z',line,pp}(r',\theta',z') = -\frac{1}{2\varepsilon_0 h}\frac{d\Lambda'(z')}{dz'}\sum_{n=1}^{\infty}\frac{1}{\sqrt{k'^2+\left(\frac{n\pi}{2h}\right)^2}}\sin(\frac{n\pi}{2})e^{-\sqrt{k'^2+\left(\frac{n\pi}{2h}\right)^2}\,r'|\cos(\theta')|}\sin[\frac{n\pi}{2h}(r'\sin(\theta')+h)]. \quad (3.92)$$

Using the Lorentz transformation of Eqs. (3.69) - (3.75), and $\theta'=\theta$, the LSC field in the *lab* frame becomes

$$E_{z,line,pp}(r,\theta,z,t) = -\frac{1}{2\varepsilon_0 h\gamma^2}\frac{\partial\Lambda(z,t)}{\partial z}\sum_{n=1}^{\infty}\frac{1}{\sqrt{\bar{k}^2+\left(\frac{n\pi}{2h}\right)^2}}\sin(\frac{n\pi}{2})e^{-\sqrt{\bar{k}^2+\left(\frac{n\pi}{2h}\right)^2}\,r|\cos(\theta)|}\sin[\frac{n\pi}{2h}(r\sin(\theta)+h)]. \quad (3.93)$$

3.5.4 A line charge inside a rectangular chamber

In the *lab* frame, assume there is an infinitely long line charge centered inside a rectangular chamber, the sinusoidal line charge density and beam intensity modulations are described in Eq. (3.64). The full chamber width and height are $W=2w$ and $H=2h$, respectively. Sect. 3.4.2 derives the potential of an infinitely long beam with rectangular cross-section and uniform transverse charge density inside a rectangular chamber. In the *rest* frame of beam, in the charge-free region inside the chamber ($b\le|y'|\le h$), the potentials are

$$\varphi'_{II,rect,rect}(x',y',z') = \frac{\Lambda'_k\cos(k'z')}{4\varepsilon_0 bw}\sum_{n=1.}^{\infty}\frac{g'_n}{v'^2_n}\frac{\sinh(v'_n b)}{\cosh(v'_n h)}\sin[\eta_n(x'+w)]\sinh[v'_n(h-|y'|)], \quad (3.94)$$

where
$$g'_n = g_n = \frac{2}{a\eta_n}\sin(\eta_n w)\sin(\eta_n a), \quad (3.95)$$

and $\eta_n=n\pi/2w$, $v_n'^2=\eta_n^2+k'^2$, $n=1, 2, 3,\ldots$. In the limiting case of $a=b=0$, the rectangular

beam shrinks to a line charge. Because a=0, g_n'=g_n=2sin($\eta_n w$) and b=0, sinh($\nu_n' b$)/b=ν_n', then Eq. (3.94) becomes

$$\varphi'_{II,line,rect}(x',y',z') = \frac{\Lambda'(z')}{2\varepsilon_0 w}\sum_{n=1.}^{\infty}\frac{\sin(\eta_n w)}{\nu'_n\cosh(\nu'_n h)}\sin[\eta_n(x'+w)]\sinh[\nu'_n(h-|y'|)]. \tag{3.96}$$

Using the Lorentz transformation of x'= x, y' = y, and Eqs. (3.69), (3.71)-(3.75), the LSC field in the *lab* frame becomes

$$E_{z,line,rect}(x,y,z,t) = -\frac{1}{2\varepsilon_0 w\gamma^2}\frac{\partial\Lambda(z,t)}{\partial z}\sum_{n=1.}^{\infty}\frac{\sin(\eta_n w)}{\nu_n\cosh(\nu_n h)}\sin[\eta_n(x+w)]\sinh[\nu_n(h-|y|)], \tag{3.97}$$

where $\nu_n^2 = \nu_n'^2 = \eta_n^2 + \bar{k}^2 = \eta_n^2 + k^2/\gamma^2$.

3.5.5 Approximate LSC impedances of a round beam between parallel plates and inside a rectangular chamber

The *average* longitudinal wake potential (or energy loss per turn of a unit charge) in a circular accelerator due to the LSC field is

$$\mathrm{V}(z,t) = -<E_z>C_0 = Z_0^{\|}(k)I_k\exp[i(kz-\omega t)], \tag{3.98}$$

where <E_z> is the LSC field averaged over the cross-section of the round beam and can be calculated using the formula

$$< f(r,\theta) >= \frac{1}{\pi r_0^2}\int_0^{2\pi} d\theta \int_0^{r_0} f(r,\theta) r dr. \tag{3.99}$$

(a) For a round beam midway between parallel plates, the *average* LSC impedance can be calculated by Eqs. (3.65), (3.76), (3.92), and (3.98) with $E_z = E_{z,round,pp} \approx E_{z,round,fs} + E_{z,line,pp} - E_{z,line,fs}$ as

$$Z_{0,roundpp}^{\parallel}(\bar{k}) = i\frac{Z_0 C_0}{2\beta\gamma h}\chi_{line,pp}(\bar{k}) + i\frac{Z_0 C_0}{\pi\beta\gamma r_0}K_1(\bar{k}r_0)[1-\frac{2I_1(\bar{k}r_0)}{\bar{k}r_0}], \tag{3.100}$$

where

$$\chi_{line,pp}(\bar{k}) = \sum_{n=1}^{\infty}\frac{1}{\sqrt{1+\left(\frac{n\pi}{2\bar{k}h}\right)^2}}\sin(\frac{n\pi}{2}) < e^{\sqrt{1+\left(\frac{n\pi}{2\bar{k}h}\right)^2}\bar{k}r|\cos(\theta)|}\sin[\frac{n\pi}{2h}(r\sin(\theta)+h)] >. \tag{3.101}$$

(b) For a round beam inside and coaxial with a rectangular chamber, the approximate *average* LSC impedance can be calculated by Eqs. (3.65), (3.76), (3.97), and (3.98) with $E_z = E_{z,round,rect} \approx E_{z,round,fs} + E_{z,line,rect} - E_{z,line,fs}$ as

$$Z_{0,round,rect}^{\parallel}(\bar{k}) = i\frac{Z_0 C_0}{2\beta\gamma w}\chi_{line,rect}(\bar{k}) + i\frac{Z_0 C_0}{\pi\beta\gamma r_0}K_1(\bar{k}r_0)[1-\frac{2I_1(\bar{k}r_0)}{\bar{k}r_0}], \tag{3.102}$$

where

$$\chi_{line,rect}(\bar{k}) = \sum_{n=1}^{\infty}\frac{\bar{k}\sin(\eta_n w)}{\nu_n\cosh(\nu_n h)} < \sin[\eta_n(r\cos(\theta)+w)]\sinh[\nu_n(h-r|\sin(\theta)|)] >. \tag{3.103}$$

In the derivations of Eqs. (3.100) and (3.102), two identities of integrals

$\int_0^{\xi} xK_0(x)dx = 1 - \xi K_1(\xi)$ and $\int_0^{\xi} xI_0(x)dx = \xi I_1(\xi)$ are used. Note that the first terms on the right hand side of Eqs. (3.100) and (3.102) are contributed from the *average* LSC fields of a line charge midway between parallel plates and inside a rectangular chamber, respectively; the second terms are contributed from the differences of the *average* LSC fields within beam radius r_0 between a round beam and a line charge in free space. Eqs. (3.101) and (3.103) can be evaluated by truncating the infinite series to a finite number of terms, as long as the sum converges well.

3.5.6 Summary of some LSC impedances formulae

For the purpose of comparisons in Sect. 3.5.7, here we would like to summarize some LSC impedance formulae in both the long-wavelength and short-wavelength limits, which are often used in literatures.

3.5.6.1 A round beam inside a round chamber

For a round beam with radius r_0 and uniform transverse distribution centered inside a round chamber with inner chamber wall radius r_w, the LSC impedance is repeated here as

$$Z^{\parallel}_{0,round,round}(\bar{k}) = i\frac{2RZ_0}{\beta\gamma\bar{k}r_0^2}\{1 - \frac{f_1}{I_0(\bar{k}r_w)}[K_1(\bar{k}r_0)I_0(\bar{k}r_w) + K_0(\bar{k}r_w)I_1(\bar{k}r_0)]\}. \quad (3.104)$$

where $f_1 = \bar{k}r_0$ for the *on-axis* impedance [24, 25] and $f_1 = 2I_1(\bar{k}r_0)$ for the *average* one (see Eqs. (3.61)-(3.63)), respectively.

(a) In the long-wavelength limits

The total LSC impedance of a uniform disk beam with radius r_0 inside a round chamber with radius r_w in the *long-wavelength* limits is [20, 25]

$$Z_{0,round,round}^{\parallel,LW}(\bar{k}) = i\frac{\bar{k}RZ_0}{\beta\gamma}(f_2 + \ln\frac{r_w}{r_0}), \tag{3.105}$$

where $f_2 = 1/2$ for the *on-axis* impedance and $f_2 = 1/4$ for the *average* one, respectively.

(b) In the short-wavelength limits

If $r_w >> r_0$, the image charge effects of the chamber wall can be neglected in the short-wavelength limits, the LSC impedance of a round beam is approximately equal to that in free space. Refs. [22, 23] give the *on-axis* LSC impedance of a round beam in the short-wavelength limits as

$$Z_{0,round,round}^{\parallel,axis,SW}(\bar{k}) = Z_{0,round,fs}^{\parallel,axis}(\bar{k}) = i\frac{2RZ_0}{\beta\gamma\bar{k}r_0^2}[1-\bar{k}r_0K_1(\bar{k}r_0)]. \tag{3.106}$$

The LSC impedances in Eq. (3.106) are derived from the *on-axis* LSC fields of the 1D space charge field model. While Ref. [25] pointed out that the 1D field model does not hold any more for $\lambda<4\pi r_0/\gamma$ or $kr_0/\gamma > 0.5$. In addition, the *off-axis* LSC fields always decrease from the beam axis $r=0$ to the beam edge $r=r_0$. Ref. [41] studied these 3D space charge effects analytically and made a conclusion that, if the LSC fields were averaged over the beam cross-section, the 1D and 3D field models predict almost the identical LSC fields. The *average* LSC impedance is given in Refs. [24, 26] as

$$Z^{\parallel}_{0,round,fs}(\bar{k}) = i\frac{2RZ_0}{\beta\gamma\bar{k}r_0^{\,2}}[1-2I_1(\bar{k}r_0)K_1(\bar{k}r_0)]. \tag{3.107}$$

3.5.6.2 A round beam inside a rectangular chamber in the long-wavelength limits

Let's assume an infinitely long, transversely uniform round beam with radius r_0 is inside and coaxial with a rectangular chamber. The full chamber width and height are W=2w and H=2h, respectively. Then according to Eq. (23) of Ref. [32], the LSC impedance of an accelerator ring in the *long-wavelength* limits is

$$Z^{\parallel,LW}_{0,round,rect}(\bar{k}) = i\frac{\bar{k}RZ_0}{\beta\gamma}\{f_3 + \ln[\frac{4h}{\pi r_0}\tanh(\frac{\pi w}{2h})]\}, \tag{3.108}$$

where $f_3 = 1/2$ for the *on-axis* impedance and $f_3 = 1/4$ for the *average* one, respectively.

3.5.6.3 A round beam between parallel plates in the long-wavelength limits

In the limiting case of $W\to\infty$, the rectangular chamber becomes a pair of parallel plates, according to Eq. (3.108), Eqs. (A6) and (A7) in Appendix of Ref. [31], its LSC impedance becomes

$$Z^{\parallel,LW}_{0,round,pp}(\bar{k}) = i\frac{\bar{k}RZ_0}{\beta\gamma}[f_4 + \ln(\frac{4h}{\pi r_0})], \tag{3.109}$$

where $f_4 = 1/2$ for the *on-axis* impedance and $f_4 = 1/4$ for the *average* one, respectively.

3.5.7 Case study and comparisons of LSC impedances

In this section, as a case study, we will calculate the approximate LSC impedances of a coasting H_2^+ beam in the SIR, compare them with the simulation results and the theoretical values predicted by other models. The kinetic energy of the beam is E_k = 20 keV ($\beta \approx 0.0046$, $\gamma \approx 1$), the beam radius r_0 is variable. Since $w>>h$, the rectangular chamber can also be simplified as a pair of infinitely large parallel plates. The LSC impedances are calculated by both theoretical and numerical methods using the Finite Element Method (FEM) code.

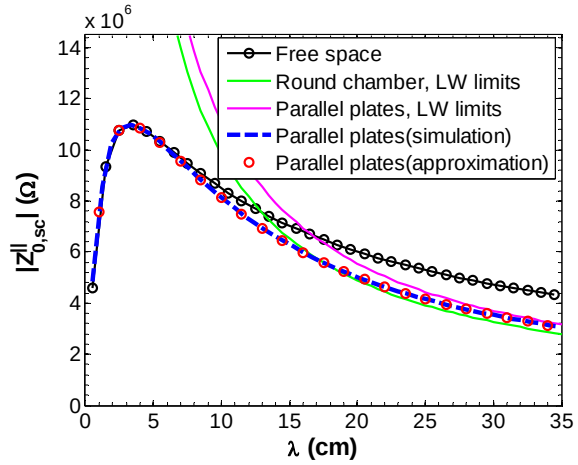

Figure 3.11: Comparisons of the *average* LSC impedances of a *round* SIR beam with beam radius r_0=0.5 cm under different boundary conditions and in different wavelength limits. λ is the perturbation wavelength, $\left|Z_{0,sc}^{||}\right|$ is the modulus of LSC impedance. In the legend, 'Free space', 'Round chamber', and 'Parallel plates' are boundary conditions; 'LW limits' stands for the *long-wavelength* limits; '(approximation)' and '(simulation)' stand for the theoretical approximation and simulation (FEM) methods, respectively.

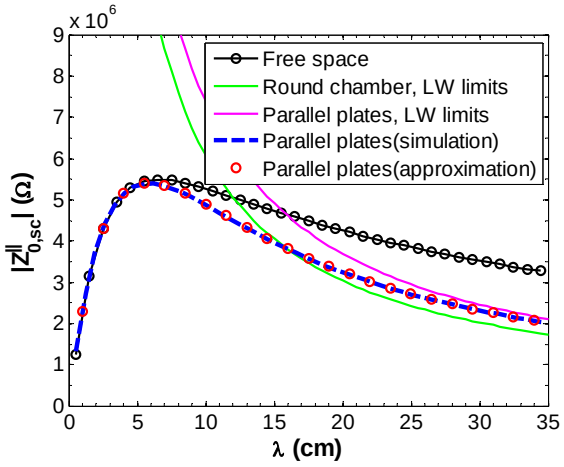

Figure 3.12: Comparisons of the *average* LSC impedances of a *round* SIR beam with beam radius r_0=1.0 cm under different boundary conditions and in different wavelength limits.

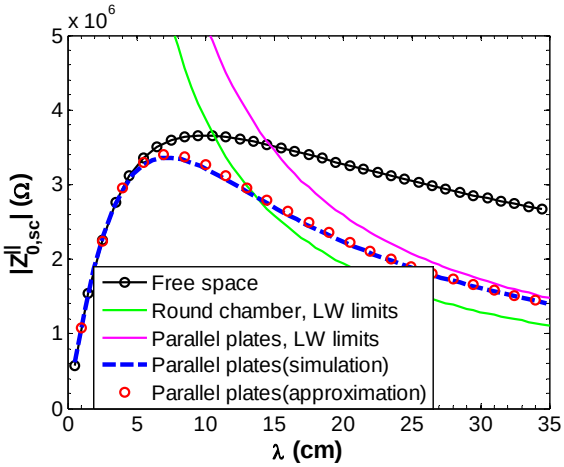

Figure 3.13: Comparisons of the *average* LSC impedances of a *round* SIR beam with beam radius r_0=1.5 cm under different boundary conditions and in different wavelength limits.

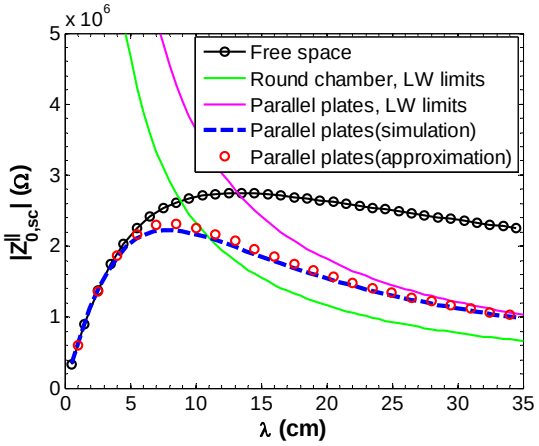

Figure 3.14: Comparisons of the *average* LSC impedances of a *round* SIR beam with beam radius r_0=2.0 cm under different boundary conditions and in different wavelength limits.

Figures 3.11- 3.14 show the simulated (blue dashes) and theoretically approximated (Eqs. (3.100) and (3.101), red circles) *average* LSC impedances of a round SIR beam with radii r_0 =0.5 cm, 1.0 cm, 1.5 cm and 2.0 cm midway between the parallel plates with h=2.4 cm. For the purpose of comparisons, the *theoretical average* LSC impedances of the round beam predicted by three existing models are also plotted. (a) In free space (Eq. (3.107), black lines with circles). (b) Inside a round chamber with r_w=h=2.4 cm, in the long-wavelength limits (Eq. (3.105), green lines). (c) Between parallel plates with h=2.4 cm, in the long-wavelength limits (Eq. (3.109), magenta lines). For a small beam size, for instance r_0<1.0 cm, the theoretical approximations are consistent well with the simulations in all the wavelengths. A small discrepancy appears for large beam size case when the image charge effect becomes large, for instance r_0=2.0 cm. The long-wavelength model with a round chamber gives smaller impedance as expected because of the larger shielding effect compared with a pairs of parallel plates. The difference of the impedance between a round chamber and a pairs of parallel plates becomes larger when the beam size increases.

Figures 3.15-3.18 show the simulated (blue dashes) and theoretically approximated (Eqs. (3.102) and (3.103), red circles) *average* LSC impedances of a round SIR beam with radii r_0 =0.5 cm, 1.0 cm, 1.5 cm and 2.0 cm inside and coaxial with a rectangular chamber with w=5.7 cm, h=2.4 cm. For the purpose of comparisons, the *theoretical average* LSC impedances predicted by three existing models are also plotted. (a) In free space (Eq. (3.107), black lines with circles). (b) Inside a round chamber with r_w=h=2.4 cm, in the long-wavelength limits (Eq. (3.105), green lines). (c) Inside a rectangular chamber with w=5.7 cm, h=2.4 cm, in the long-wavelength limits (Eq. (3.108), magenta lines).

Figures 3.11-3.18 show that, for both the parallel plates and rectangular chamber models, the simulated (blue dashes) and theoretical (red circles) *average* LSC impedances match quite well for the cases r_0 = 0.5 cm, 1.0 cm and 1.5 cm ($r_0/h\approx$0.21, 0.42, and 0.63). For the case of r_0=2.0 cm ($r_0/h \approx 0.83$), the relative errors between the theoretical and simulated peak LSC impedances are about 3.8% and 4.0% for the parallel plates and rectangular chamber models, respectively. This shows the line charge approximation in calculation of the image fields of a round beam is valid. Only at r_0 = 2.0 cm may this assumption underestimate the shielding effects of the image fields resulting in overestimation of the LSC impedances to some small noticeable extents. When the transverse beam dimension approaches the chamber height, the line charge assumption for the image charge fields of a round beam may induce bigger but still acceptable errors. For the wavelengths in the range of $0<\lambda\leq5$ cm, the theoretical (red circles) and simulated (blue dashes) *average* LSC impedance curves overlap the impedance curves for a beam in free space (black lines with circles) predicted by Eq. (3.107). It denotes that the

shielding effects due to the image charges are on a negligible level, it is valid to calculate the average LSC impedances by Eq. (3.107) directly for the parallel plates and rectangular chamber models. For λ>5 cm, the average LSC impedances predicted by the model of a round beam in free space (black lines with circles) gradually deviate from and are larger than the theoretical (red circles) and simulated (blue dashes) LSC impedances of the two models discussed in this paper. This is caused by the neglect of the important shielding effects of beam chambers at large wavelengths. When λ approaches 35 cm, the theoretical (red circles) and simulated (blue dashes) *average* LSC impedance curves approach the magenta curves predicted by Eq. (3.109) in Figures 3.11-3.14 and Eq. (3.108) in Figures 3.15-3.18 in the *long-wavelength* limits, respectively. These comparison results indicate the derived average LSC impedance formulae Eqs. (3.100)-(3.103) are consistent well with the simulations and the existing LSC impedance models in both the short-wavelength and long-wavelength limits. In the long-wavelength limits, for $r_0<<h$, the average LSC impedances of the round chamber model (green lines) are consistent with the ones predicted by the parallel plates and rectangular models (see the red circles and blue dashes in Figure 3.11 and Figure 3.15); while as r_0 increases and approaches *h,* the round chamber model (green lines) predicts smaller LSC impedances gradually than the parallel plates and rectangular chamber models (red circles and blue dashes) at large wavelengths (see Figures 3.12-3.14 and Figures 3.16-3.18). This result indicates that, at large perturbation wavelengths, the round chamber model has larger shielding effects on the LSC fields than the models with planar and rectangular boundaries, and the shielding effects of the round chamber become more significant when $r_0/h \rightarrow 1$.

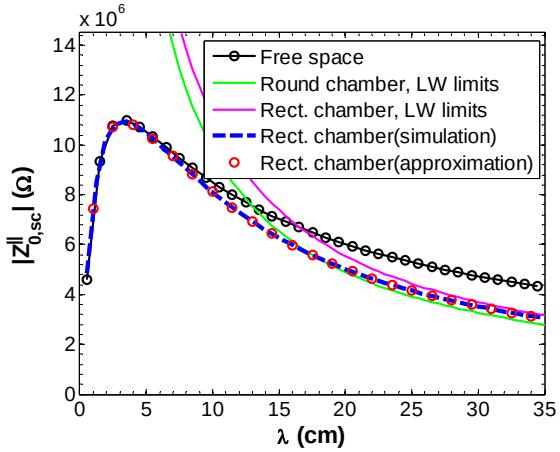

Figure 3.15: Comparisons of the *average* LSC impedances of a *round* SIR beam with beam radius r_0=0.5 cm under different boundary conditions and in different wavelength limits. In the legend, 'Free space', 'Round chamber', and 'Rect. chamber' are boundary conditions, where 'Rect.' is the abbreviation for 'Rectangular'; The other symbols and abbreviations are the same as those in Figure 3.11.

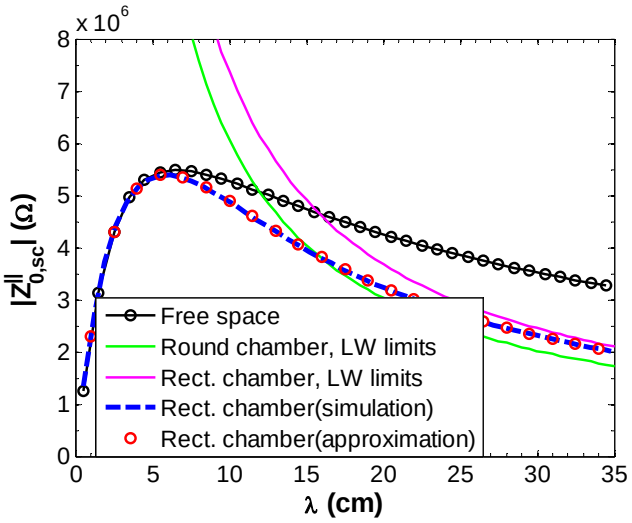

Figure 3.16: Comparisons of the *average* LSC impedances of a *round* SIR beam with beam radius r_0=1.0 cm under different boundary conditions and in different wavelength limits.

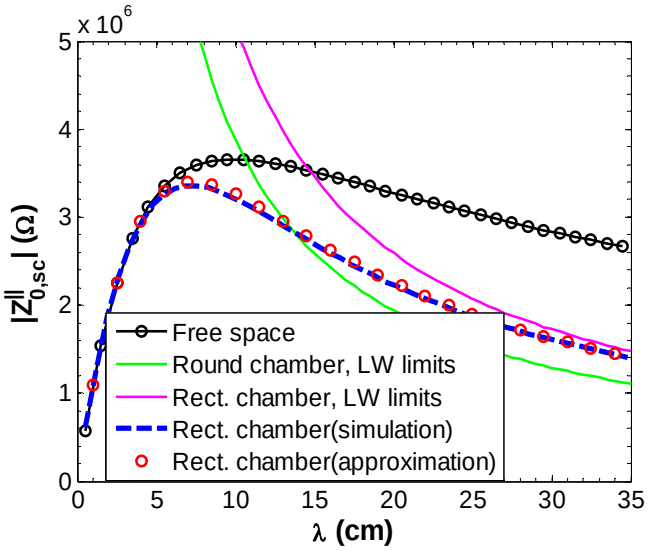

Figure 3.17: Comparisons of the *average* LSC impedances of a *round* SIR beam with beam radius r_0=1.5 cm under different boundary conditions and in different wavelength limits.

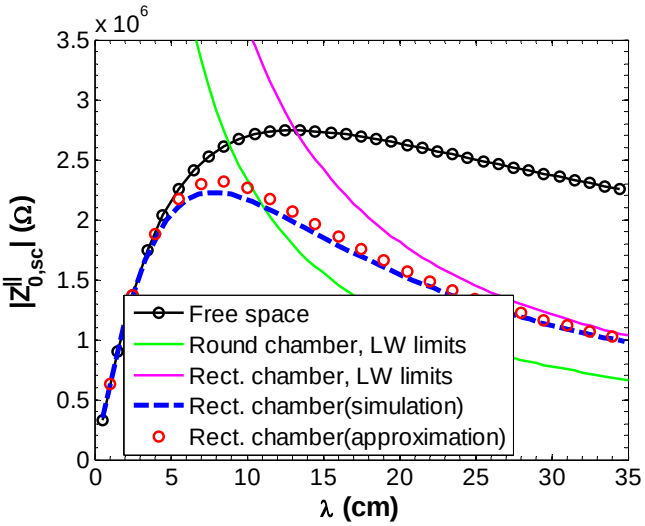

Figure 3.18: Comparisons of the *average* LSC impedances of a *round* SIR beam with beam radius r_0 =2.0 cm under different boundary conditions and in different wavelength limits.

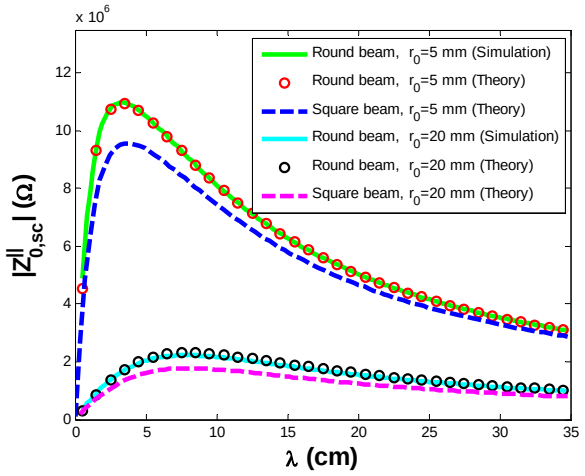

Figure 3.19: Comparisons of the *average* LSC impedances between the round beam and square beam for a parallel plate field model. For a round beam, r_0 is the beam radius; for a square beam, r_0 is the half length of the side. The square beam model underestimates the LSC impedances.

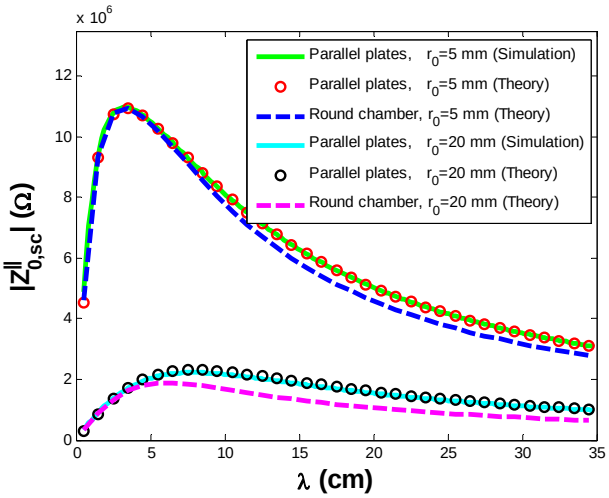

Figure 3.20: Comparisons of the *average* LSC impedances of a round beam between parallel plates and a round beam inside a round chamber. The round chamber model underestimates the LSC impedances at larger λ.

Figure 3.19 shows the *average* LSC impedances of a SIR beam with beam radii r_0=0.5 cm and 2.0 cm midway between a pair of parallel plates with h=2.4 cm. The theoretical impedances are calculated by both the round beam model using Eq. (3.100) and square beam model (a=b=r_0), respectively. For a round beam, the square beam model with

length of side $a=b=r_0$ may underestimate the average LSC impedances compared with the round beam model with radius r_0.

Figure 3.20 shows the *average* LSC impedances of a *round* SIR beam with beam radii r_0 =0.5 cm and 2.0 cm midway between a pair of *parallel plates* with h=2.4 cm and inside a *round chamber* with $r_w=h$=2.4 cm. The theoretical impedances of the parallel-plate model and round chamber model are calculated by Eq. (3.100) and Eq. (3.104), respectively. For a round beam with fixed radius and energy, the round chamber model may underestimate the average LSC impedances compared with the parallel plates model with radius $h=r_w$. This difference is caused by the stronger shielding effects of the image fields produced by the round chamber compared with the parallel plates. Some literatures use the round chamber model to approximate the LSC field and impedance of a round beam between parallel plates or inside a rectangular chamber (e.g., Ref. [16]). Figure 3.20 clearly indicates that this approximation only holds when λ is small, where the shielding effect is negligible. For a 20 keV SIR beam with r_0 =0.5 cm inside a rectangular chamber with w=5.7 cm and h=2.4 cm, the round chamber approximation for the LSC impedance is only accurate for $\lambda\leq$ 5 cm. For $\lambda>$ 5 cm, the round chamber approximation will induce larger errors.

In summary, Figures 3.11-3.20 show that, for a typical 20 keV SIR beam with r_0 =0.5 cm inside a rectangular chamber, when $\lambda\leq$ 5 cm, the image charge effects are negligible. In this case, for simplicity, we can use the LSC impedance formula for a round beam in free space (Eq. (3.107)) to calculate the LSC impedance with a good accuracy; For $\lambda\geq$35 cm, we can use the impedance formulae in the long-wavelength limits Eq. (3.108) for a rectangular chamber model or Eq. (3.109) for a parallel plates model to estimate the LSC

impedance. While for 5 cm<λ<35 cm, none of the existing models and formulae can be used to evaluate the LSC impedance accurately. In this case, we have to use the approximate theoretical impedance formulae Eqs. (3.102) and (3.103) for a rectangular-chamber model or Eqs. (3.100) and (3.101) for a parallel-plate model. This is the merit of the approximate analytical LSC impedance formulae derived in this chapter.

3.5.8 Conclusions for the model of a round beam inside rectangular chamber (between parallel plates)

In this subsection, we mainly derive the approximate average LSC impedance formulae for a round beam under two boundary conditions: (a) Midway between a pair of infinitely large, perfectly conducting parallel plates. (b) Inside and coaxial with a perfectly conducting rectangular chamber. In most accelerators, since $w>>r_0$, $h>>r_0$, the image charge fields of a round beam can be treated as those of a line charge in calculation of the LSC fields inside the beam. Consequently, the associated LSC impedances can be approximated by means of image methods based on the superposition theorem of the electric fields. The approximate theoretical average LSC impedances of the parallel-plate model and the rectangular-chamber model are consistent well with the numerical simulation results in a wide range of the radios of r_0/h. In addition, the theoretical LSC impedances predicted by the two field models also match well with the existing field models in both the short-wavelength ($\lambda \leq 5$ cm) and the long-wavelength ($\lambda \rightarrow 35$ cm) limits. In particular, for 5 cm<λ<35 cm, the approximate theoretical LSC impedances formulae have better accuracies than the existing models and formulae. Hence, they are valid at any perturbation wavelengths and can be used as general expressions of the *average* LSC impedances in the future research work on space-charge induced

instabilities, even for large ratios of r_0/h. At last, the image method together with the line charge approximation employed in this paper can also be used to derive the LSC impedances of field models with other cross-sectional geometries.

Chapter 4

MICROWAVE INSTABILITY AND LANDAU DAMPING EFFECTS[2]

4.1 Introduction

Our previous simulation and experimental results indicated that the instability growth rates of SIR beam are proportional to the unperturbed beam intensity I_0 instead of the square root of I_0 [13]. Pozdeyev [14, 15] and Bi [16] developed their own models and theories separately to explain the mechanisms of microwave instability in the isochronous regime, respectively. Pozdeyev pointed out that, in the isochronous regime, the radial coherent space charge fields of a coasting bunch with centroid wiggling may modify the slip factor, raise the working point above transition and enhance the microwave instability. This makes the instability growth rates linearly dependent on the beam intensity [14, 15]. While Bi's model [16] is not consistent with the scaling law on beam intensity, since the unperturbed beam density component is neglected in calculation of the coherent radial space charge force of the perturbed local centroid.

It is also found in the simulations that the spectral evolutions of the line charge densities are not pure exponential functions of time, instead, they are often characterized by the betatron oscillations superimposed on the exponential growth curves. These betatron oscillations are the dipole modes in the longitudinal structure of the beam due to dipole moment of the centroid offsets [20].

[2] Y. Li, L. Wang, F. Lin, Nuclear Instruments and Methods in Physics Research A 763, 674 (2014).

In the isochronous regime, the longitudinal motion of particles was usually thought to be frozen. If and how the Landau damping affects the instability growth rates in the isochronous regime is still unknown for beam physicists. The theoretical and simulation studies in this chapter demonstrate that the Landau damping mechanism can also take effect and suppress the microwave instability for a beam with space charge in the isochronous regime.

Both Pozdeyev and Bi's models use the 1D (longitudinal) conventional instability growth rates formula derived exclusively for a monoenergetic beam and neglects the emittance effect. As a result, the radial-longitudinal coupling effects in an isochronous ring are not included completely. This may overestimate the instability growth rates, especially for the short-wavelength perturbations, because the Landau damping effects caused by the finite energy spread and the emittance are all neglected. Though Pozdeyev explained the suppression of the instability growth of short-wavelength perturbations by the radial-longitudinal coupling effects qualitatively [15], till now, no quantitative discussions on the Landau damping effects are available for a coasting bunch with space charge in the isochronous regime.

To predict the microwave instability growth rates more accurately than the existing conventional 1D formula, this chapter introduces and derives a 2D dispersion relation with Landau damping effects considering the contributions from both the finite energy spread and emittance. By doing this, it can explain the suppression of the microwave instability growth rates of the short-wavelength perturbations and predict the fastest-growing wavelength.

This chapter is organized as follows. Sect. 4.2 discusses the limitations of the

conventional 1D growth rates formula and presents a modified 2D dispersion relation. Sect. 4.3 discusses the Landau damping effects in the isochronous ring by 2D dispersion relation. Sect. 4.4 carries out the simulation study of microwave instability in SIR and provides benchmarking of the 2D dispersion relation with different initial beam parameters.

4.2 2D dispersion relation

4.2.1 A brief review of the 1D growth rates formula

The conventional 1D growth rates formula for the microwave instability of a monoenergetic and laminar beam used in Ref. [15] is:

$$\tau^{-1}(k) = \omega_0 \sqrt{-i \frac{\eta e I_0 k R Z(k)}{2\pi\beta^2 E}}, \tag{4.1}$$

where ω_0 is the angular revolution frequency of the on-momentum particles, $\eta=\alpha-1/\gamma^2$ is the slip factor, α is the momentum compaction factor, γ is the relativistic energy factor of the on-momentum particle, e is the electron charge, I_0 is the unperturbed beam intensity, k is the perturbation wavenumber of the longitudinal charge density, R is the average ring radius, $Z(k)$ is the longitudinal space charge (LSC) impedance, β is the relativistic speed factor, E is the total energy of the on-momentum charged particle. Essentially, the 1D dispersion relation Eq. (23) of Ref. [16] is the same as the 1D growth rates formula Eq. (4.1), if we express the LSC field by the LSC impedance.

For the circular SIR beam with radius r_0, the transverse dimension of the vacuum chamber is much greater than the beam diameter. Hence, Ref. [15] neglects the image charge effects of the chamber in the short-wavelength limits, and chooses $Z(k)$ is equal to

the *on-axis* LSC impedance of the monopole mode [15]:

$$Z(k) = Z_{0,sc}^{\parallel}(k) = i\frac{2Z_0 R}{k\beta r_0^{\,2}}[1 - \frac{kr_0}{\gamma}K_1(\frac{kr_0}{\gamma})], \tag{4.2}$$

where Z_0 = 377 Ohm (Ω) is the impedance of free space, $K_1(x)$ is the modified Bessel function of the second kind.

For a coasting long bunch with strong space charge effects in the isochronous ring, the LSC fields may induce the coherent energy deviations and the associated radial offsets of the local centroids. Consequently, there is centroid wiggling along the bunch. Ref. [15] assumed that the longitudinal distribution of the radial centroid offsets is a sinusoidal function of the longitudinal coordinate z with a wavenumber k_c. In the first-order approximation, we can choose $k \approx k_c$ and use the same k in the expressions of $\eta(k)$ and $Z(k)$ in Eq. (4.1) just as treated in Ref. [15] (please check Eqs. (2), (12), (13), and (14) in Ref. [15]).

Ref. [15] uses the following formalism to derive the space-charge modified coherent slip factor of a local centroid: due to centroid wiggling, there will be coherent radial space charge field $E_{x,sc}$. It produces positive increments in the dispersion function D (which is approximated by $D \approx 1/\nu_x^2$), the momentum compaction factor α, and the coherent slip factor $\eta(k)$. Finally, the space-charge modified coherent slip factor $\eta_{sc}(k)$ can be determined, i.e., $E_{x,sc} \rightarrow \Delta D_{sc} \rightarrow \Delta\alpha_{sc} \rightarrow \Delta\eta_{sc}(k) \rightarrow \eta_{sc}(k)$. In the end, $\eta_{sc}(k)$ may be approximated as [14, 15]

$$\eta \approx \eta_{sc}(k) = \frac{eI_0}{2\pi\varepsilon_0\gamma m_{H_2^+}\omega_0^{\,3} r_0^2 R}[1 - \frac{kr_0}{\gamma}K_1(\frac{kr_0}{\gamma})]. \tag{4.3}$$

Note the relativistic factor γ is introduced in Eq. (4.3) to make the original expressions of

$\eta_{sc}(k)$ in Refs. [14, 15] compatible with the high energy beams. Plugging Eqs. (4.2) and (4.3) into Eq. (4.1) gives the instability growth rates $1/\tau \propto I_0[1-\frac{kr_0}{\gamma}K_1\left(\frac{kr_0}{\gamma}\right)]$.

4.2.2 Limitations of 1D growth rates formula

Though the above formalism adopted in Ref. [15] may explain the origin of the microwave instability of SIR beam and is consistent with the scaling law on beam intensity, it is not accurate enough and still has some limitations.

First, the LSC impedance in Eq. (4.2) is evaluated from the *on-axis* LSC field of a 1D space charge field model. As discussed in Chapter 3, due to the 3D effects on the LSC fields, Eq. (4.2) should be replaced by the *average* LSC impedance formula to account for the LSC field more accurately in the short-wavelength limits:

$$Z(k) = Z_{0,sc}^{\parallel}(k) = i\frac{2Z_0R}{k\beta r_0^{\,2}}[1-2I_1(\frac{kr_0}{\gamma})K_1(\frac{kr_0}{\gamma})]. \tag{4.4}$$

Second, the space-charge modified coherent slip factor is not accurate enough since it does not include the betatron oscillation effect of the local centroid (please refer to Eq. (2.30) of Sect. 2.6). In Ref. [42], the transformation of the longitudinal coordinate z with respect to the bunch center is

$$z = z_0 + R_{51}x_0 + R_{52}x_0' + R_{56}\delta, \tag{4.5}$$

where x_0 and $x_0' = dx_0/ds$ are the initial radial betatron motion amplitude and velocity slope at s=0, respectively, $\delta=\Delta p/p$ is the fractional *momentum* deviation, $R_{51}(s)$, $R_{52}(s)$, and $R_{56}(s)$ are the transfer matrix elements and depend on the path length s. Note that in Ref. [42], δ was defined differently as the fractional *energy* deviation $\delta=\Delta E/E$ of an

ultra-relativistic electron particle with $\beta \approx 1$, since $\delta = \Delta p/p \approx (\Delta E/E)/\beta^2 \approx \Delta E/E$; in addition, the definition of $R_{51}(s)$, $R_{52}(s)$, and $R_{56}(s)$ in Eq. (4.5) and Ref. [42] are different from the standard ones (please refer to Appendices A and B for details). For a coasting beam with space charge in the isochronous ring, in the conventional 1D (longitudinal) beam dynamics, the space–charge modified parameters of the slip factor η_{sc}, the momentum compaction factor α_{sc}, the transition gamma $\gamma_{t,sc}$, the element $R_{56,sc}$, and the local dispersion function $D_{sc}(s)$ are related to each other by:

$$\eta_{sc} = \alpha_{sc} - \frac{1}{\gamma^2} = \frac{1}{\gamma_{t,sc}^2} - \frac{1}{\gamma^2} = -\frac{R_{56,sc}(C_0)}{C_0}, \tag{4.6}$$

$$\alpha_{sc} = \frac{1}{\gamma_{t,sc}^2} = -\frac{R_{56,sc}(C_0)}{C_0} + \frac{1}{\gamma^2} = \frac{1}{C_0}\int_L \frac{D_{sc}(s)}{\rho(s)} ds = < \frac{D_{sc}(s)}{\rho(s)} >, \tag{4.7}$$

where $\rho(s)$ is the local radius of curvature of trajectory, <···> denotes the average value over the ring circumference C_0. From Eqs. (4.6), (4.7) and the formalism used in Ref. [15], we can see that only the contribution of the momentum compaction factor α_{sc} or the element $R_{56,sc}$ is considered in the modification of $\eta_{sc}(k)$. While Eq. (4.5) shows $\Delta z = z - z_0$ is determined by R_{51}, R_{52}, and R_{56}, the ring is isochronous if $\Delta z = 0$ after one revolution. The space-charge modified coherent slip factor of a local centroid should be dependent on both R_{56} and R_{51}, R_{52}. In Ref. [42], where the *method of characteristics* is employed, the parameters x_0, x_0', and z_0, at $s=0$ are regarded as constants of motion, they are related to the current coordinates of the particle x, x' and z at position s by a canonical transformation

$$x_0(x, x', \delta, s) = \sqrt{\frac{\hat{\beta}_0}{\hat{\beta}}}(x - D\delta)\cos\psi - \sqrt{\hat{\beta}_0\hat{\beta}}[x' - D'\delta + \frac{\hat{\alpha}}{\hat{\beta}}(x - D\delta)]\sin\psi,$$

$$x_0'(x,x',\delta,s)=\frac{x-D\delta}{\sqrt{\hat{\beta}\hat{\beta}_0}}\sin\psi+\sqrt{\frac{\hat{\beta}}{\hat{\beta}_0}}[x'-D'\delta+\frac{\hat{\alpha}}{\hat{\beta}}(x-D\delta)]\cos\psi, \tag{4.8}$$

$$z_0(x,x',\delta,s)=z-R_{56}\delta-x_0R_{51}-x_0'R_{52},$$

where $\hat{\alpha}$, $\hat{\beta}_0$, and $\hat{\beta}$ are the Courant-Snyder parameters, ψ is the phase advance. Their derivatives with respect to δ are

$$\frac{\partial x_0}{\partial\delta}=-\sqrt{\frac{\hat{\beta}_0}{\hat{\beta}}}D\cos\psi+\sqrt{\hat{\beta}_0\hat{\beta}}(D'+\frac{\hat{\alpha}}{\hat{\beta}}D)\sin\psi,$$

$$\frac{\partial x_0'}{\partial\delta}=-\frac{D}{\sqrt{\hat{\beta}\hat{\beta}_0}}\sin\psi-\sqrt{\frac{\hat{\beta}}{\hat{\beta}_0}}(D'+\frac{\hat{\alpha}}{\hat{\beta}}D)\cos\psi, \tag{4.9}$$

$$\frac{\partial z_0}{\partial\delta}=-R_{56}-\frac{\partial x_0}{\partial\delta}R_{51}-\frac{\partial x_0'}{\partial\delta}R_{52},$$

which usually are non-zero parameters. Accordingly, the exact expression of the slip factor at s can be calculated as $\eta(s,k)=-(d\Delta z/d\delta)/C_0=-[R_{51}(s,s+C_0)\partial x_0/\partial\delta+R_{52}(s,s+C_0)\partial x_0'/\partial\delta+R_{56}(s,s+C_0)]/C_0$, and it also depends on $R_{51}(s,s+C_0)$, $R_{52}(s,s+C_0)$ if $\partial x_0/\partial\delta\neq0$ and $\partial x_0'/\partial\delta\neq0$. Here $R_{51}(s,s+C_0)$, $R_{52}(s,s+C_0)$ and $R_{56}(s,s+C_0)$ are the transfer matrix elements between s and $s+C_0$. The space–charge modified slip factor expressed in Eq. (4.6) is only a special case at $s=0$, $\partial x_0/\partial\delta=0$, and $\partial x_0'/\partial\delta=0$. The contributions of $R_{51,sc}$ and $R_{52,sc}$ to the coherent slip factor are related to the betatron motion of the centroid and should not be neglected in the isochronous regime.

Third, Ref. [15] only takes into account the coherent motion of the local beam centroid neglecting the incoherent motions of individual particles in the beam slices. In fact, a local beam slice usually has a finite energy spread and emittance. Eq. (4.5) and the above analysis indicate that, the betatron motions of particles in a beam slice with different δ, x_0,

and x_0' may have different longitudinal path length differences Δz which are not the same as that of the local centroid. This may cause smearing of the beam intensity perturbations and is the very reason of Landau damping.

4.2.3 Space-charge modified tunes and transition gammas in the isochronous regime

The radial space charge fields may modify the radial tunes and transition gammas in the isochronous regime [14-16]. Due to the large ratios between the full chamber width (~11.4 cm), full chamber gap (~4.8 cm) and the beam diameter (~1 cm), the image charge effects caused by the vacuum chamber are small for perturbation wavelength $\lambda \leq 5$ cm as shown in Chapter 3. Then Pozdeyev's model [14, 15] of a uniform circular beam with centroid wiggling in free space can be used to calculate the radial space charge fields and modified tunes. Assuming the total radial offset of a particle is $x=x_c+x_\beta$, where x_c is the beam centroid offset $x_c=a_c\cos(kz)$, k is the wavenumber of radial offset perturbations of local beam centroids with respect to the design orbit along z, x_β is the radial offset of a single particle due to the betatron oscillation. The equations of coherent and incoherent radial motions can be expressed as:

$$x_c'' + \frac{v_x^2}{R^2} x_c = \frac{\delta_{coh}}{R} + \frac{eE_{x,coh}}{\gamma m_{H_2^+} \beta^2 c^2}, \tag{4.10}$$

$$x_\beta'' + \frac{v_x^2}{R^2} x_\beta = \frac{\delta_{inc}}{R} + \frac{eE_{x,inc}}{\gamma m_{H_2^+} \beta^2 c^2}, \tag{4.11}$$

where v_x is the bare radial betatron tune, δ_{coh} and δ_{inc} are the coherent and incoherent fractional momentum deviations, $E_{x,coh}$ and $E_{x,inc}$ are the coherent and incoherent radial space charge fields [15, 16], respectively, and can be expressed as

$$E_{x,coh} = \xi_{coh}\gamma m_{H_2^+}\omega_0^{\,2} x_c / e, \qquad E_{x,inc} = \xi_{inc}\gamma m_{H_2^+}\omega_0^{\,2} x_\beta / e. \tag{4.12}$$

Here

$$\xi_{coh} = \frac{eI_0}{2\pi\varepsilon_0\gamma m_{H_2^+}\omega_0^{\,3} r_0^2 R}[1-\frac{kr_0}{\gamma}K_1(\frac{kr_0}{\gamma})], \qquad \xi_{inc} = \frac{eI_0}{2\pi\varepsilon_0\gamma m_{H_2^+}\omega_0^{\,3} r_0^2 R}, \tag{4.13}$$

are two unitless parameters. For a typical SIR beam with $0 < \xi_{coh} << 1$ and $0 < \xi_{inc} << 1$, the coherent and incoherent radial tunes can be easily obtained from Eqs. (4.10)-(4.13) as

$$\nu_{x,coh} \approx \nu_x(1-\frac{\xi_{coh}}{2\nu_x^2}), \qquad \nu_{x,inc} \approx \nu_x(1-\frac{\xi_{inc}}{2\nu_x^2}). \tag{4.14}$$

Here the coherent radial tune $\nu_{x,coh}$ and incoherent radial tune $\nu_{x,inc}$ stand for the number of betatron oscillations per revolution of a local centroid and a single particle, respectively. According to Ref. [16], the space-charge modified coherent and incoherent transition gammas in an isochronous accelerator are

$$\gamma_{t,coh}^2 = \frac{\delta p/p}{\delta R/R} = 1-n-\xi_{coh}, \qquad \gamma_{t,inc}^2 = \frac{\delta p/p}{\delta R/R} = 1-n-\xi_{inc}, \tag{4.15}$$

where n= -(r/B)($\partial B/\partial r$) is the magnetic field index. For the SIR with $n < 0$, $|n|<<1$, if the space charge effects are negligible (i.e., $\xi_{coh}=\xi_{inc}=0$, $\gamma_{t,0}^2 = 1-n$), the bare slip factor is η_0 $=1/\gamma_{t,0}^2 - 1/\gamma^2 \approx 1+n-1/\gamma^2 \approx 2\times 10^{-4}$. Then

$$\frac{1}{\gamma_{t,coh}^2} - \frac{1}{\gamma^2} \approx \eta_0 + \xi_{coh}, \qquad \frac{1}{\gamma_{t,inc}^2} - \frac{1}{\gamma^2} \approx \eta_0 + \xi_{inc}. \tag{4.16}$$

4.2.4 2D dispersion relation

For a hot beam with large energy spread and emittance in an isochronous ring, the Landau damping effects are important due to the strong radial-longitudinal coupling.

Hence, a multi-dimensional dispersion relation including both the longitudinal and radial dynamics is needed. Usually the vertical motions of particles can be regarded as decoupled from their radial and longitudinal motions. In this section, first, we would like to summarize and comment the main procedures and definitions used in Ref. [42], where a 2D (longitudinal and radial) dispersion relation was derived for the coherent synchrotron radiation (CSR) instability of an ultra-relativistic electron beam in a conventional storage ring. Based on this model, we can derive a 2D dispersion relation for the microwave instability of the non-relativistic H_2^+ beam in an isochronous ring.

4.2.4.1 Review of the 2D dispersion relation for CSR instability of ultra-relativistic electron beams in non-isochronous regime

First, Ref. [42] defined a 2D Gaussian beam model with an initial equilibrium beam distribution function

$$f_0 = \frac{n_b}{2\pi\varepsilon_{x,0}} \exp[-\frac{x_0^{\,2} + (\hat{\beta}_0 x_0')^2}{2\varepsilon_{x,0}\hat{\beta}_0}] g(\delta + \hat{u} z_0), \tag{4.17}$$

where

$$g(\delta) = \frac{1}{\sqrt{2\pi}\sigma_\delta} \exp(-\frac{\delta^2}{2\sigma_\delta^{\,2}}), \tag{4.18}$$

n_b is the linear number density of the beam, $\varepsilon_{x,0}$ is the initial radial emittance, x_0 is the initial radial offset, $x_0' = dx_0/ds$ is the initial radial velocity slope, $\hat{\beta}_0$ is the betatron function at s=0, δ is the uncorrelated fractional *momentum* deviation, $\hat{u}$ is the chirp parameter which accounts for the correlation between the longitudinal position z of the particle in the bunch and its fractional momentum deviation δ, σ_δ is the *uncorrelated* fractional RMS *momentum* spread (Note in Ref. [42], σ_δ was defined differently as the *uncorrelated* fractional RMS *energy* spread for an ultra-relativistic electron beam with

$\beta \approx 1$). Then the perturbed distribution function f_1 is assumed to have a sinusoidal dependence on z_0 as

$$f_1(x_0, x_0', z_0, \delta_0, s) = f_k(x_0, x_0', \delta_0, s) e^{ikz_0}, \tag{4.19}$$

where $\delta_0 = \delta + \hat{u} z_0$ is the total fractional momentum deviation including both the *uncorrelated* and *correlated* fractional momentum deviation. Plugging the distribution function of $f=f_0+f_1$ into the linearized Vlasov equation, after lengthy derivations, a Volterra integral equation is derived as

$$g_k(s) = g_k^{(0)}(s) + \int_0^s K(s', s) g_k(s') ds', \tag{4.20}$$

where

$$g_k(s) = \int dx_0 dx_0' d\delta_0 f_k(x_0, x_0', \delta_0, s) \exp\{-ikC(s)[\delta_0 R_{56}(s) + x_0 R_{51}(s) + x_0' R_{52}(s)]\}, \tag{4.21}$$

$$g_k^{(0)}(s) = \int dx_0 dx_0' d\delta_0 f_k(x_0, x_0', \delta_0, 0) \exp\{-ikC(s)[\delta_0 R_{56}(s) + x_0 R_{51}(s) + x_0' R_{52}(s)]\}, \tag{4.22}$$

$$C(s) = \frac{1}{1 - \hat{u} R_{56}(s)}, \tag{4.23}$$

is the bunch length compression factor, $K(s', s)$ is the kernel of integration. The perturbed harmonic line density with wave number k at (z, s) is

$$n_{1,k}(z, s) = \int dx_0 dx_0' d\delta_0 f_1 = C(s) g_k(s) e^{-ikC(s)z}. \tag{4.24}$$

We can see that $|C(s)g_k(s)|$ is just the amplitude of the perturbed line density at s. For storage rings, the linear chirp factor $\hat{u} = 0$, the compression factor $C(s)$ =1. By smooth approximations of $\varepsilon_{x,0} = \sigma_x^2 \nu_x / R$, $\hat{\beta} = R/\nu_x$, $\psi = \nu_x s / R$, $D = R/\nu_x^2$, $\hat{\alpha} = 0$, $D' = 0$, the integral kernel in Eq. (4.20) is simplified as

$$K(s', s) = K_1(\chi)$$

$$= -\frac{ie\Lambda_0}{v_x^{\,2}\gamma m_{e^-}cC_0}kZ(k)[-\frac{R}{v_x}\sin(\frac{v_x\chi}{R})+\chi]e^{-(k\sigma_x/v_x)^2[1-\cos(v_x\chi/R)]-(k\sigma_\delta/v_x^{\,2})^2\chi^2/2}, \qquad (4.25)$$

where $\Lambda_0=en_b$ is the unperturbed line charge density, m_{e^-} is the rest mass of electron, $Z(k)$ is the CSR impedance in unit of Ohm, σ_x is the RMS beam radius, $\chi=s-s'$ is the relative path length difference between two positions at s and s', specifically, if we choose $s'=0$, then $\chi=s$. Note that the Eq. (4.25) uses the SI instead of CGS system of units as in Ref. [42]. By smooth approximation, the kernel $K(s', s)$ is only dependent on the parameter $\chi=s-s'$ and radial tune ν_x. Applying Laplace transform to the two sides of Eq. (4.20) yields an algebraic equation

$$\hat{g}_k(\mu)=\frac{\hat{g}_k^{(0)}(\mu)}{1-\hat{K}(\mu)}, \qquad (4.26)$$

where μ is the complex Laplace variable and

$$\hat{g}_k(\mu)=\int_0^\infty ds g_k(s)e^{-\mu s}, \qquad (4.27)$$

$$\hat{g}_k^{(0)}(\mu)=\int_0^\infty ds g_k^{(0)}(s)e^{-\mu s}, \qquad (4.28)$$

$$\hat{K}(\mu)=\int_0^\infty d\chi K_1(\chi)e^{-\mu\chi}, \qquad (4.29)$$

are the Laplace images of $g_k(s)$, $g_k^{(0)}(s)$ and $K_1(\chi)$, respectively. The relation of $1-\hat{K}(\mu)=0$ for the denominator of Eq. (4.26) determines the dispersion relation. Finally the 2D dispersion relation for the CSR instability of an ultra-relativistic electron beam in a non-isochronous storage ring is derived in Appendix B of Ref. [42] as

$$1=-\frac{ie\Lambda_0}{v_x^{\,2}\gamma m_{e^-}cC_0}kZ(k)\int_0^\infty d\chi e^{-\mu\chi}[\chi-\frac{R}{v_x}\sin\frac{v_x\chi}{R}]e^{-(k\sigma_x/v_x)^2[1-\cos(v_x\chi/R)]-(k\sigma_E/Ev_x^{\,2})^2\chi^2/2}. \qquad (4.30)$$

Note $\sigma_\delta\approx\sigma_E/E$ has been used in Eq. (4.30), where σ_E is the RMS energy spread, and the

SI system of units is used in Eq. (4.30). Eq. (4.30) is an integral equation which determines the relations between the wavenumber k and the complex Laplace variable μ. For a fixed k, the values of μ can be solved numerically.

Ref. [42] did not explicitly interpret the CSR instability growth rates from the solutions to Eq. (4.30). Theoretically speaking, $g_k(s)$ can be calculated by inverse Laplace transform (Fourier-Mellin transform)

$$g_k(s) = \frac{1}{2\pi i}\int_{\sigma-i\infty}^{\sigma+i\infty} d\mu \frac{\hat{g}_k^{(0)}(\mu)}{1-\hat{K}(\mu)} e^{\mu s}, \tag{4.31}$$

where σ is a positive real number. The integration is along the Bromwich contour, which is a line parallel to the imaginary μ-axis and to the right of all the singularities satisfying $1-\hat{K}(\mu)=0$ in the complex μ-plane. In practice, the integral in Eq. (4.31) poses a great difficulty in mathematics due to complexity of the integrand. A popular method dealing with this difficulty is widely used in the Plasma Physics [43-46] by applying Cauchy's residue theory to an equivalent Bromwich contour. First, the Bromwich contour is deformed by analytic continuation, and then the solutions of $g_k(s)$ can be evaluated by the residues of the poles using Cauchy's residue theorem as

$$g_k(s) \approx \sum_j Rsd[\hat{g}_k(\mu)e^{\mu s}, \mu_j] = \sum_j \lim_{\mu\to u_j}[(\mu-\mu_j)\hat{g}_k(\mu)e^{\mu s}] = \sum_j e^{\mu_j s} Rsd[\hat{g}_k(\mu), \mu_j], \tag{4.32}$$

where $Rsd[\hat{g}_k(\mu), \mu_j]$ stands for the residue of $\hat{g}_k(\mu)$ at the pole μ_j. Using the relation $s = \beta ct$, where t is the time, the temporal evolution of $g_k(s)$ becomes

$$g_k(t) \approx \sum_j e^{\mu_j \beta ct} Rsd[\hat{g}_k(\mu), \mu_j]. \tag{4.33}$$

For a storage ring, $C(s)$=1, Eq. (4.24) gives the amplitude of perturbed harmonic line density with wavenumber k as

$$| n_{1,k}(z,t) | = | g_k(t) | . \tag{4.34}$$

Eqs. (4.33) and (4.34) show that, for a pole at μ_j, (a) if Re(μ_j)<0, the k-th Fourier component of the line density damps exponentially at a rate of τ^{-1}=Re(μ_j)βc; (b) if Re(μ_j)>0, this pole may induce the CSR instability which grows exponentially at a rate of τ^{-1}=Re(μ_j)βc. The total instability growth rates are dominated by the pole μ_j which has the greatest positive real part.

4.2.4.2 2D dispersion relation for microwave instability of low energy beam in isochronous regime

The 2D dispersion relation Eq. (4.30) can be modified to study the space-charge induced microwave instability of a low energy coasting H_2^+ bunch in the SIR. In the derivation of Eq. (4.30), the term which is proportional to $1/\gamma^2$ is neglected in the longitudinal equation of motion due to $\gamma >> 1$. In addition, in Eq. (4.30), the method of smooth approximation is used to express all the beam optics parameters, such as the betatron function, phase advance, dispersion function, R_{51}, R_{52}, and R_{56} as functions of radial tune ν_x. Because the space charge effects are also neglected, the radial betatron tune ν_x in Eq. (4.30) is a k-independent constant. While for a coasting beam with space charge in the SIR, the space charge fields may modify the radial tunes and beam optics parameters. These neglected terms and space charge effects should be considered in the 2D dispersion relation for the SIR beam. Hence Eq. (1) and Eq. (4) of Ref. [42] should be modified as

$$\frac{dz}{ds} = -\frac{x}{\rho(s)} \rightarrow -\frac{x}{\rho(s)} + \frac{\delta}{\gamma^2}, \tag{4.35}$$

$$R_{56}(s) = -\int_0^s \frac{D(s')}{\rho(s')} ds' \rightarrow -\int_0^s \frac{D_{sc}(s')}{\rho(s')} ds' + \frac{s}{\gamma^2}. \tag{4.36}$$

Consequently, using relative path length difference χ=s-s', the increment of R_{56} from s' to s in Eq. (B4) of Ref. [42] should be modified as

$$\Delta R_{56}(s', s) = -\frac{1}{\nu_x^2}\chi \rightarrow -(\frac{1}{\gamma_{t,sc}^2} - \frac{1}{\gamma^2})\chi. \tag{4.37}$$

When the elements R_{51} and R_{52} are included, the corresponding modified increment of R_{56} becomes

$$\Delta\widetilde{R}_{56}(s',s) = -\frac{1}{\nu_x^2}[\chi - \frac{R}{\nu_x}\sin(\frac{\nu_x\chi}{R})] \rightarrow -(\frac{1}{\gamma_{t,sc}^2} - \frac{1}{\gamma^2})\chi + \frac{R}{\nu_{x,sc}^3}\sin(\frac{\nu_{x,sc}\chi}{R}). \tag{4.38}$$

where $\nu_{x,sc}$ is the space-charge modified radial tune.

Note that:

(a) In Eq. (4.37), for the longitudinal dynamics in the isochronous regime, we cannot use the method of smooth approximation to express $\Delta R_{56}(s', s)$ by $-(1/\nu_{x,sc}^2 - 1/\gamma^2)\chi$ directly due to smallness of the slip factor, otherwise it will induce considerable errors. We may use $\Delta R_{56}(s', s) = -(1/\gamma_{t,sc}^2 - 1/\gamma^2)\chi$ instead. While the sinusoidal function term in Eq. (4.38) is contributed from R_{51} and R_{52}, and it can be estimated as a function of the radial betatron tune $\nu_{x,sc}$ using the smooth approximation.

(b) In Eqs. (4.36)-(4.38), $R_{56}(s) = \partial z/\partial\delta$ is the linear correlation coefficient between the longitudinal coordinate z at s and the fractional momentum deviation δ at s=0. $\Delta R_{56}(s', s)$ is the increment of R_{56} between s' and s without the effects of R_{51} and R_{52}

$$\Delta R_{56}(s', s) = R_{56}(s) - R_{56}(s'). \tag{4.39}$$

$\Delta\widetilde{R}_{56}(s',s)$ differs from $R_{56}(s)$ and $\Delta R_{56}(s',\ s)$ by including the effects of R_{51} and R_{52}. According to Appendix A of Ref. [42], for a coasting beam in the SIR, $\Delta\widetilde{R}_{56}(s',s)$ can be simplified as

$$\Delta\widetilde{R}_{56}(s',s)=\Delta R_{56}(s',s)|_{s'}+\Delta R_{51}(s',s)\frac{\partial x_0}{\partial\delta}|_{s'}+\Delta R_{52}(s',s)\frac{\partial x_0'}{\partial\delta}|_{s'}. \tag{4.40}$$

Now we can substitute Eqs. (4.37) and (4.38) into Eq. (4.30) to obtain the 2D dispersion relation for the SIR beam. In the substitution, in the square bracket of the integrand between the two exponential functions of Eq. (4.30), the space-charge modified transition gamma $\gamma_{t,sc}$ and the radial tune $\nu_{x,sc}$ should be replaced by the coherent ones of $\gamma_{t,coh}$ and $\nu_{x,coh}$, respectively. While $\gamma_{t,sc}$ and $\nu_{x,sc}$ in the last exponential function of Eq. (4.30) should be replaced by the incoherent ones of $\gamma_{t,inc}$ and $\nu_{x,inc}$, respectively. If the uncorrelated fractional RMS *momentum* spread σ_δ is replaced by the RMS *energy* spread σ_E using the relation $\sigma_\delta=\sigma_E/(\beta^2E)$, where E is the total energy of the on-momentum particle, finally, the 2D dispersion relation for a low energy SIR beam in the SI system of units becomes

$$1=-\frac{ie\Lambda_0}{\beta\gamma m_{H_2^+}cC_0}kZ_{0,sc}^{\parallel}(k)\int_0^\infty d\chi e^{-\mu\chi}\left[\left(\frac{1}{\gamma_{t,coh}^2}-\frac{1}{\gamma^2}\right)\chi-\frac{R}{\nu_{x,coh}^3}\sin\frac{\nu_{x,coh}\chi}{R}\right]\cdot e^{-(k\sigma_x/\nu_{x,inc})^2[1-\cos(\nu_{x,inc}\chi/R)]-\frac{1}{2}[\frac{k\sigma_E}{\beta^2E}(1/\gamma_{t,inc}^2-1/\gamma^2)\chi]^2}. \tag{4.41}$$

Note that the 2D dispersion relation Eq. (4.41) is derived for a Gaussian beam model without the coherent radial centroid offsets and energy deviations. Therefore it is only valid for predictions of the long-term microwave instability growth rates in an isochronous ring neglecting the line charge density oscillations due to dipole moments of

the centroid offsets. Here the term 'long-term' stands for multi-periods of betatron oscillations in the time scale. When the dispersion relation Eq. (4.41) is to be solved numerically, a large but finite real number can be set as the upper limit of χ instead of infinity to calculate the integral.

4.3 Landau damping effects in isochronous ring

4.3.1 Space-charge modified coherent slip factors

For the SIR beam with typical beam intensities, usually $|\eta_0| << \xi_{coh}$, when the space charge effects are considered. Then in the first-order approximation, according to Eq. (4.16), the space-charge modified coherent slip factor without the effects of R_{51} and R_{52} (e.g., neglect the betatron motion effects) may be estimated as

$$\eta_{coh} = \eta_{\mathrm{R}56} = \frac{1}{\gamma^2_{t,coh}} - \frac{1}{\gamma^2} \approx \eta_0 + \xi_{coh} \approx \xi_{coh}, \tag{4.42}$$

which is essentially the same as Eq. (12) in Ref. [15].

For a ring lattice with average radius R and space-charge modified radial tune $\nu_{x,sc}$, by smooth approximation of $\hat{\beta}=R/\nu_x$, $\psi=\nu_x s/R$, $D=R/\nu_x^2$, $\hat{\alpha}=0, D'=0$, the increments of R_{51} and R_{52} between s' and s can be calculated from Eq. (B2) and Eq. (4) of Ref. [42] as

$$\Delta R_{51}(s',s) = -\frac{1}{\nu_{x,sc}}[\sin(\frac{\nu_{x,sc}}{R}s) - \sin(\frac{\nu_{x,sc}}{R}s')], \tag{4.43}$$

$$\Delta R_{52}(s',s) = \frac{1}{\nu^2_{x,sc}}[\cos(\frac{\nu_{x,sc}}{R}s) - \cos(\frac{\nu_{x,sc}}{R}s')]. \tag{4.44}$$

According to Eq. (4.9) (i.e., Eq. (20) of Ref. [42]),

$$\frac{\partial x_0}{\partial \delta}|_{s'} = -\frac{R}{\nu_{x,sc}^2}\cos(\frac{\nu_{x,sc}}{R}s'), \tag{4.45}$$

$$\frac{\partial x_0'}{\partial \delta}|_{s'} = -\frac{1}{\nu_{x,sc}}\sin(\frac{\nu_{x,sc}}{R}s'). \tag{4.46}$$

Then by Eqs. (4.40)，(4.43)-(4.46), in the second-order approximation, taking into account the contributions from the matrix elements R_{51} and R_{52} (e.g., the betatron motion effects) to the longitudinal beam dynamics, the space-charge modified coherent slip factor can be calculated as

$$\tilde{\eta}_{coh} = -\frac{\Delta\tilde{R}_{56}(s,s+C_0)}{C_0} = -[\Delta R_{56}(s,s+C_0)|_s + \Delta R_{51}(s,s+C_0)\frac{\partial x_0}{\partial \delta}|_s + \Delta R_{52}(s,s+C_0)\frac{\partial x_0'}{\partial \delta}|_s]/C_0$$

$$= \eta_{R56} + \eta_{R51}(s) + \eta_{R52}(s) = \eta_{R56} - \frac{1}{2\pi\nu_{x,coh}^3}\sin(2\pi\nu_{x,coh}), \tag{4.47}$$

where

$$\eta_{R51}(s) = -\Delta R_{51}(s,s+C_0)\frac{\partial x_0}{\partial \delta}|_s / C_0 = -\frac{1}{2\pi\nu_{x,coh}^3}[\sin(\frac{\nu_{x,coh}}{R}(s+C_0)) - \sin(\frac{\nu_{x,coh}}{R}s)]\cos(\frac{\nu_{x,coh}}{R}s), \tag{4.48}$$

$$\eta_{R52}(s) = -\Delta R_{51}(s,s+C_0)\frac{\partial x_0'}{\partial \delta}|_s / C_0 = \frac{1}{2\pi\nu_{x,coh}^3}[\cos(\frac{\nu_{x,coh}}{R}(s+C_0)) - \cos(\frac{\nu_{x,coh}}{R}s)]\sin(\frac{\nu_{x,coh}}{R}s), \tag{4.49}$$

$$\eta_{R56} = -\Delta R_{56}(s,s+C_0)/C_0 = \frac{1}{\gamma_{t,sc}^2} - \frac{1}{\gamma^2}, \tag{4.50}$$

are the slip factors contributed from the matrix elements R_{51}, R_{52} and R_{56}, respectively. We can see η_{R51} and η_{R52} are functions of s, while η_{R56} is independent of s. The last term of Eq. (4.47) is contributed from the combined effects of R_{51} and R_{52} and is independent of s. In fact, Eq. (4.47) is the same as Eq. (2.30) which describes an off-momentum particle performing betatron oscillation around a closed orbit.

Assuming a SIR bunch has beam intensity $I_0 = 1.0$ μA, kinetic Energy $E_{k0} = 19.9$ keV,

radial and vertical emittance $\varepsilon_{x,0}=\varepsilon_{y,0}=50\pi$ mm mrad, the calculated slip factors by Eqs. (4.47)-(4.50) as functions of the line charge perturbation wavelength λ at $s= C_0$ and $s=10$ C_0 are shown in Figure 4.1. If we increase the beam intensity to 10 μA, the calculated slip factors at $s= C_0$ and $s= 10$ C_0 are shown in Figure 4.2.

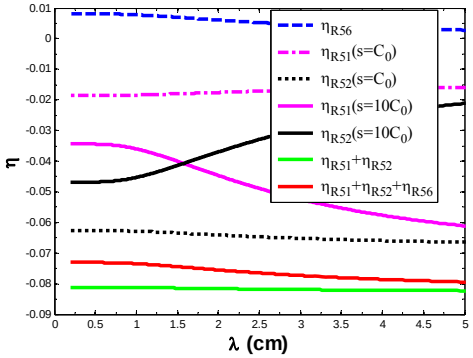

Figure 4.1: Slip factors for $I_0 = 1.0$ μA at $s=C_0$ and $s=10$ C_0.

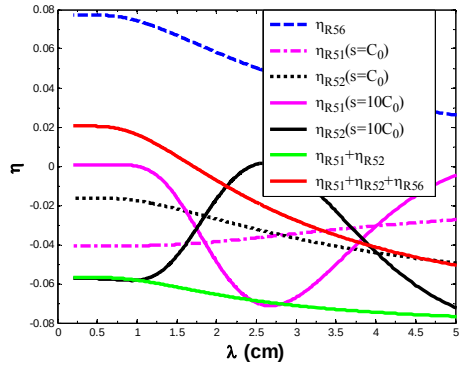

Figure 4.2: Slip factors for $I_0 = 10$ μA at $s=C_0$ and $s=10$ C_0.

Figure 4.1 and Figure 4.2 demonstrate that, for a beam in an isochronous ring, because of smallness of η_{R56}, the component of the space-charge modified slip factor $\eta_{R51}+\eta_{R52}$ contributed from the elements of R_{51} and R_{52} plays an important role in the longitudinal beam dynamics and cannot be neglected. The situation is different from a storage ring working far from transition. Note that in Figure 4.1 and Figure 4.2, the total slip factor

$\eta_{R51}+\eta_{R52}+\eta_{R56}$ can be negative for some given perturbations wavelengths and beam parameters.

4.3.2 Exponential suppression factor

We can define the exponential function of the integrand in Eq. (4.41) as exponential suppression factor (E.S.F.)

$$E.S.F. = e^{-(k\sigma_x/\nu_{inc})^2[1-\cos(\nu_{inc}\chi/R)]^2} \times e^{-\frac{1}{2}[\frac{k\sigma_E}{\beta^2 E}(1/\gamma_{t,inc}{}^2-1/\gamma^2)\chi]^2}. \qquad (4.51)$$

The first exponential function in Eq. (4.51) originates from the smooth approximation of $\Delta R_{51}(s', s)=R_{51}(s)-R_{51}(s')$, $\Delta R_{52}(s', s)=R_{52}(s)-R_{52}(s')$ and the emitttance $\varepsilon_{x,0}=\sigma_x^2 \nu_{x,inc}/R$. While the second exponential function in Eq. (4.51) originates only from the RMS energy spread and $\Delta R_{56}(s', s)=R_{56}(s)-R_{56}(s')$ without the contributions of R_{51} and R_{52}. The *E.S.F.* is a measure of Landau damping effects for the microwave instability of SIR beam.

For a SIR beam with the current of 1.0 μA, mean kinetic energy of 19.9 keV, Figure 4.3(a) shows the calculated *E.S.F.* at $\chi=C_0$ with $\sigma_E=0$ and variable emittance. Figure 4.3(b) shows the calculated *E.S.F.* at $\chi=C_0$ with $\varepsilon_{x,0}=50\pi$ mm mrad and variable σ_E. Note for a beam without uncorrelated energy spread ($\sigma_E=0$ eV), the *E.S.F.* in the short-wavelength limits is still small due to the finite beam emittance effect. Since the *E.S.F.* is related to $\exp[-A(k\sigma_x)^2]=\exp[-A(2\pi\sigma_x/\lambda)^2]$ and $\exp[-B(k\sigma_E)^2]=\exp[-B(2\pi\sigma_E/\lambda)^2]$, where A and B are coefficients which are independent of σ_x, σ_E and λ, then the Landau damping effects are more effective for a beam with large uncorrelated RMS energy spread and emittance at the shortest perturbation wavelengths. Figure 4.4(a) and Figure 4.4(b) show the calculated *E.S.F.* at $\chi=10C_0$. Comparison between Figure 4.3(b) and Figure 4.4(b)

indicates the *E.S.F.* decreases significantly with larger relative path length difference χ due to the finite uncorrelated energy spread effect.

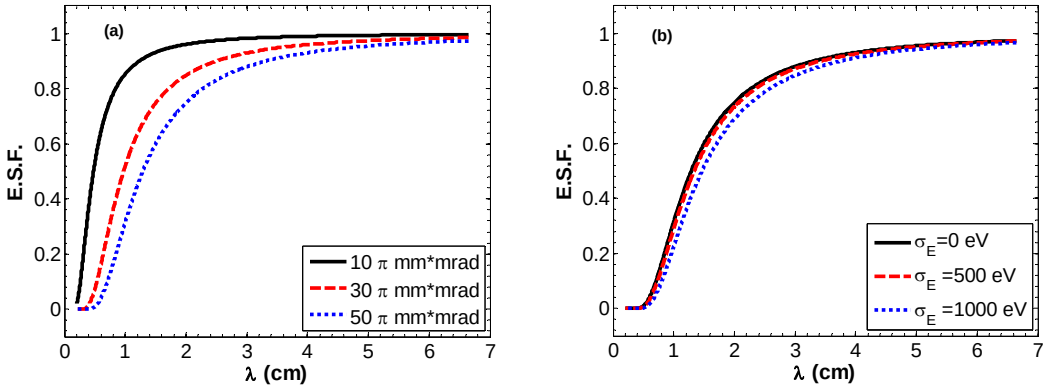

Figure 4.3: The *E.S.F.* at $\chi = C_0$ for a 1.0 μA, 19.9 keV SIR beam. (a) $\sigma_E = 0$, and variable emittance. (b) $\varepsilon_{x,0}$= 50π mm mrad, and variable σ_E.

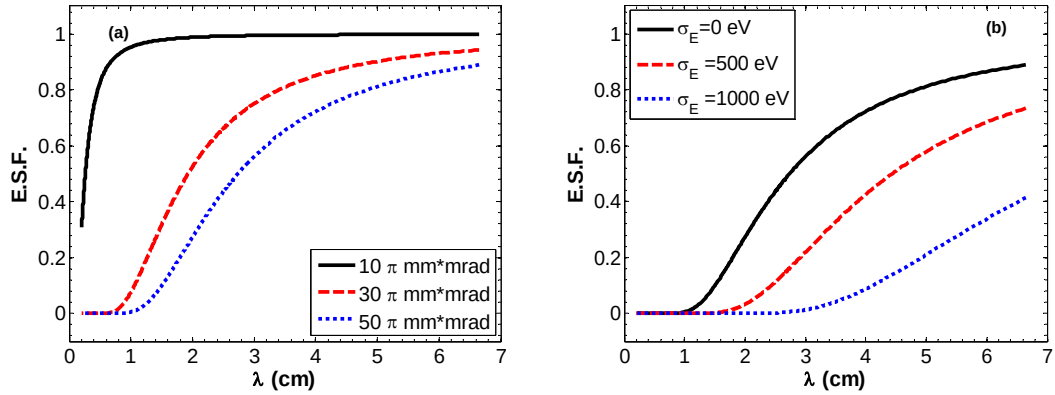

Figure 4.4: The *E.S.F.* at χ=10C_0 for a 1.0 μA, 19.9 *keV* SIR beam. (a) σ_E=0, and variable emittance. (b) $\varepsilon_{x,0}$= 50π mm mrad, and variable σ_E.

The radial-longitudinal coupling matrix elements R_{51} and R_{52} may affect the microwave instability in an isochronous ring in two ways. (a) Eqs. (4.47)-(4.50) show R_{51} and R_{52} may modify the coherent space-charge modified slip factor for a beam with coherent energy deviations and the associated radial centroid offsets. (b) Eq. (4.51) shows, if a coasting beam has finite energy spread and emittance, the incoherent motions of charged

particles under the effects of matrix elements $R_{51,}$ R_{52} and R_{56} may produce a finite spread in the longitudinal motion spectrum around the revolution frequency. The revolution frequency spread can help to smear out the longitudinal charge density modulations and suppress the microwave instability growth rates, especially for the short-wavelength perturbations. This is the origin of the Landau damping effects in the isochronous regime. Since the matrix elements $R_{51,}$ R_{52} and R_{56} may affect the beam instability in such a complicated way, it is difficult to predict how the instability growth rates will change if only one of these elements is increased or decreased.

4.3.3 Relations between the 1D growth rates formula and 2D dispersion relation

In the 2D dispersion relation Eq. (4.41), if we neglect the *E.S.F.* (incoherent motion effects of single particle) and the sinusoidal term in the square bracket of the integrand which originates from the coupling matrix elements $R_{51}(s)$ and $R_{52}(s)$ (coherent betatron motion effects of the local centroids), the 2D dispersion relation is reduced to

$$1 = -\frac{ie\Lambda_0}{\beta\gamma m_{H_2+} cC_0} kZ^{\parallel}_{0,sc}(k)\int_0^{\infty} d\chi e^{-\mu\chi}\left(\frac{1}{\gamma^2_{t,coh}} - \frac{1}{\gamma^2}\right)\chi. \tag{4.52}$$

With Eq. (4.42) and the equality of

$$\int_0^{\infty} dse^{-\mu s} s = \frac{1}{\mu^2}, \tag{4.53}$$

the simplified 2D dispersion relation Eq. (4.52) can be reduced further as

$$\tau^{-1}(k) = \mu\beta c = \omega_0\sqrt{-i\frac{\eta_{coh} eI_0 kRZ^{\parallel}_{0,sc}}{2\pi\beta^2 E}}. \tag{4.54}$$

Eq. (4.54) is just the Eq. (4.1) for a 1D monoenergetic beam.

Though the model and the 1D dispersion relation in Ref. [16] can predict the fastest-growing wavelength, the predicted growth rates are not proportional to the unperturbed beam intensity I_0. In Ref. [16], the longitudinal line density is $N(z)=N_k\cos(kz)$, and the radial coherent space charge field factor α calculated in Eq. (12) of Ref. [16] is proportional to $N(z)$. In Eq. (23) of Ref. [16], the constant parameter is proportional to the unperturbed line density N_0 which is from Eq. (18) for the longitudinal beam dynamics. Considering Eq. (24) of the same paper, since the instability growth rates ω_i predicted by Eq. (23) are proportional to $[N_0N_k(z)]^{1/2}$ instead of N_0 or I_0, then the predicted instability growth rates of this model and theory violate the scaling law with respect to the unperturbed beam intensity I_0 observed in our experiments and simulations. In reality, the longitudinal line density should be $N(z)=N_0+N_k\cos(kz)$, the above discrepancy results from the missing of N_0 in the model in calculation of the radial space charge field factor α. Note that the parameter $\chi_2(k)$ in Eqs. (17) and (23) of Ref. [16] has a similar behavior to $1-kr_0\cdot K_1(kr_0)$ plotted in Fig. 5 of Ref. [15], which peaks at wavelength $\lambda=0$ and decreases monotonically with λ. If N_0 were included in this model, this model would be similar to the one in Refs. [14, 15]. It can neither explain the suppression of the short-wavelength perturbations nor predict the fastest-growing wavelengths properly.

4.4 Simulation study of the microwave instability in SIR

4.4.1 Simulated growth rates of microwave instability

In this section, we will study the simulated spectral evolutions of the microwave

instability using the fast Fourier transform (FFT) technique and compare with the theoretical calculations. Studies of the long-term microwave instability are carried out by running CYCO up to 100 turns for a macro-particle bunch to mimic a real H_2^+ bunch in SIR. The bunch has an initial beam intensity I_0 =1.0 μA, monoenergetic kinetic energy E_{k0}=19.9 keV, radial and vertical emittance $\varepsilon_{x,0}=\varepsilon_{y,0}=50\pi$ mm mrad. The initial distributions are uniform in both the 4-D transverse phase space (x, x', y, y') and the longitudinal charge density. A total of 300000 macroparticles are used in the simulation. Considering both the curvature effects on the space charge fields when a long bunch enters the bending magnets, and the edge field effects of a short bunch, a bunch length of τ_b =300 *ns* ($L_b \approx$40 cm) is selected in the simulation. Due to the strong nonlinear edge effects in the bunch head and tail, only the beam profiles of the central part of the bunch with longitudinal coordinates -10 cm $\leq z \leq$ 10 cm are analyzed by FFT. At each turn, the density profiles of the coasting bunch with coordinates of -10 cm $\leq z \leq$ 10 cm are sliced into 512 small bins along z-coordinate, the number of macroparticles in each bin is counted, and the 512-point FFT analysis is performed with respect to z. The microwave instability of SIR beam is a phenomenon of line charge density perturbations with typical wavelengths of only several centimeters. The full chamber height is about 4.8 cm, which gives the approximate upper limit of the perturbation wavelengths in the simulation study. According to the Nyquist-Shannon sampling theorem, the shortest wavelength which can be analyzed by the 512-point FFT is 2×20 cm/512≈0.078 cm. Since the beam diameter is about 1.0 cm, the simulation results for the shorter wavelengths of λ =1.0 cm, 0.5 cm and 0.25 cm may give us some insights on the instabilities of short wavelengths comparable to or less than the transverse beam size. A series of mode number of 4, 5, 7, 10, 20, 40

and 80 are selected for the 20-cm-long beam profiles, which give the corresponding line charge density perturbation wavelengths of λ=5 cm, 4 cm, 2.857 cm, 2 cm, 1 cm, 0.5 cm and 0.25 cm. The growth rates of these wavelengths are fitted numerically and studied in the analysis. In order to minimize the effects of randomness in the initial beam micro-distribution on the simulation results, for each setting of beam parameters, the code CYCO is run five times for five different initial micro-distributions, and the average growth rates of the five runs for each given perturbation wavelength are used as the simulated growth rates in the analysis work.

Figures 4.5- 4.7 show the simulated beam profiles and line density spectra at turn 0, turn 60, and turn 100 for a single run of CYCO, respectively. In each of these figures, the left graph displays the top view of the beam distributions (blue dots) superimposed by the number of macroparticles per bin (red curve); the right graph displays the spectrum of the line charge density analyzed by FFT. We can see the line density modulation amplitudes increase with turn numbers, and the peaks of the line density spectra shift to the frequencies around $1/\lambda \approx 0.5$ cm^{-1} or the wavelength $\lambda \approx 2.0$ cm at large turn number.

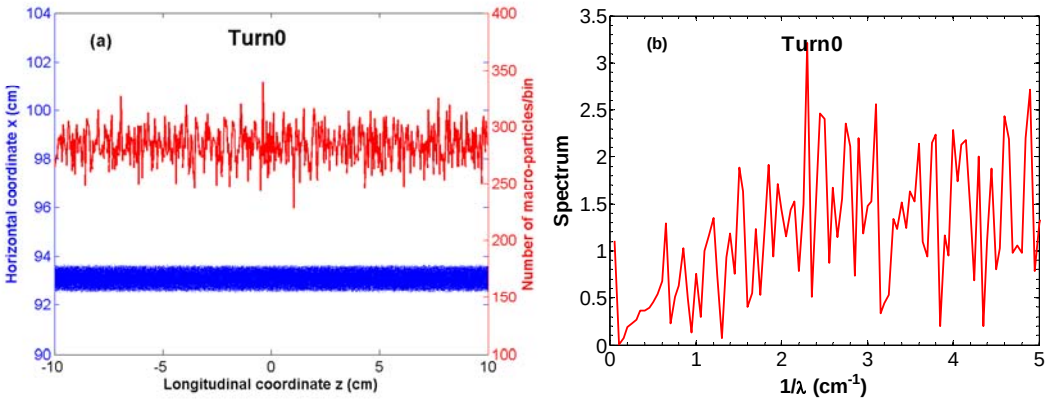

Figure 4.5: (a) Beam profiles and (b) line density spectrum at turn 0.

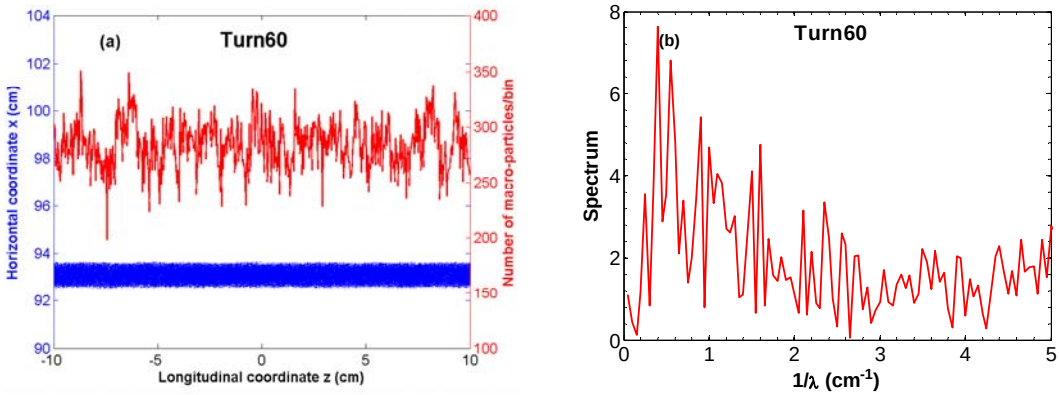

Figure 4.6: (a) Beam profiles and (b) line density spectrum at turn 60.

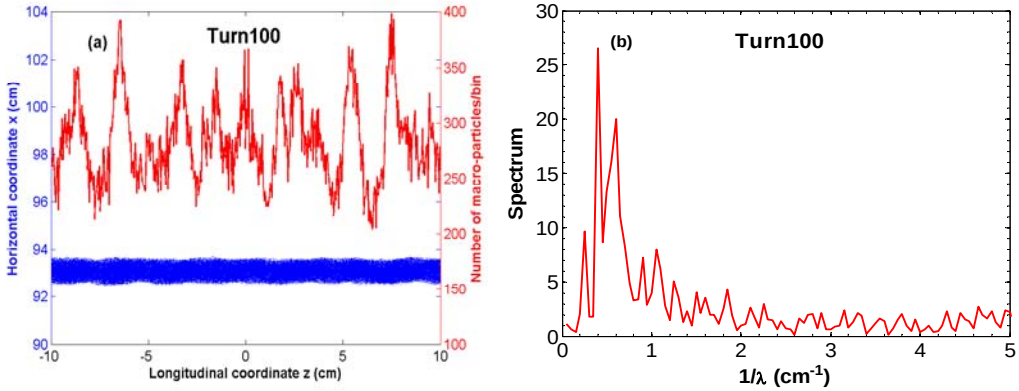

Figure 4.7: (a) Beam profiles and (b) line density spectrum at turn 100.

Figure 4.8 shows the FFT analysis results of the temporal evolutions of the normalized line charge densities $\hat{\Lambda}_k / \Lambda_0$ for the seven chosen line charge density perturbation wavelengths λ up to turn 100 for a single run of CYCO. We can see there are some oscillations superimposed on the exponential growth curves.

Figure 4.9 shows the temporal evolutions of the normalized line charge densities spectra of six given wavelengths and the fitting results using proper fitting functions.

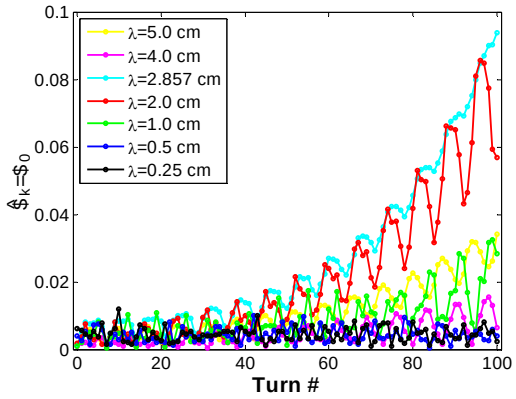

Figure 4.8: Evolutions of harmonic amplitudes of the normalized line charge densities.

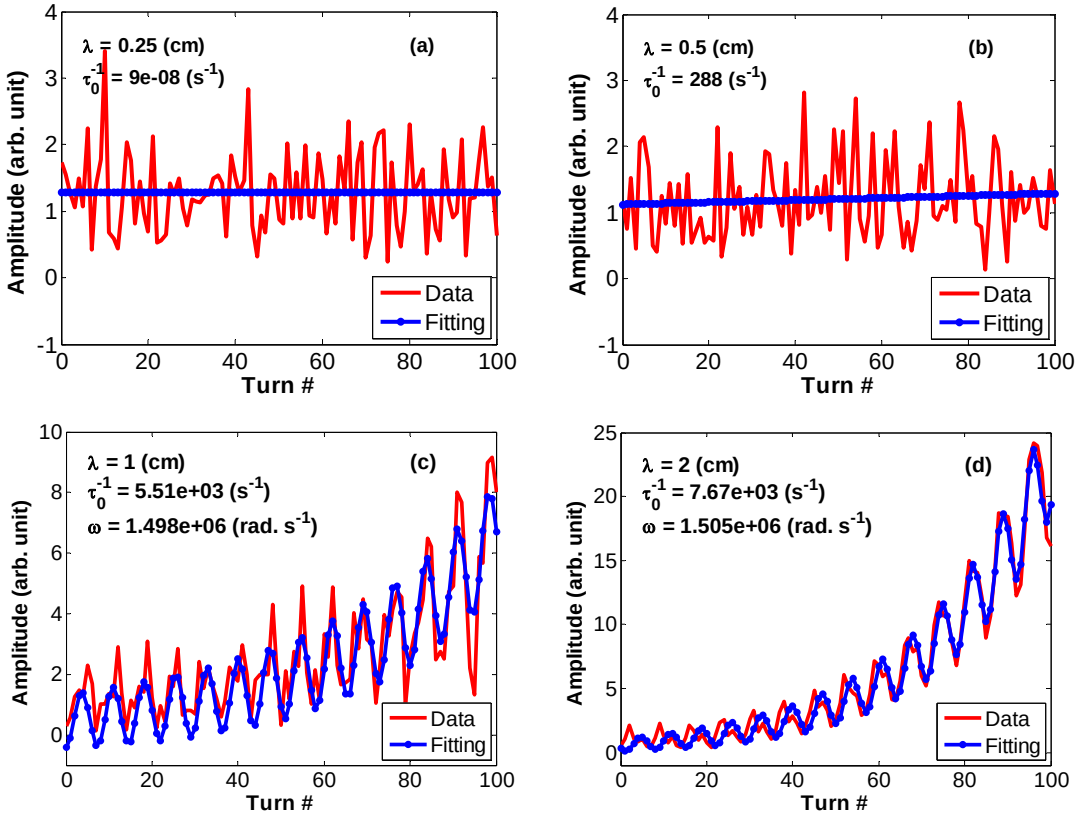

Figure 4.9: Curve fitting results for the growth rates of the normalized line charge densities for a single run of CYCO. (a) λ = 0.25 cm; (b) λ = 0.5 cm; (c) λ = 1.0 cm; (d) λ = 2.0 cm; (e) λ = 2.857 cm; (f) λ = 5.0 cm.

Figure 4.9 (cont'd)

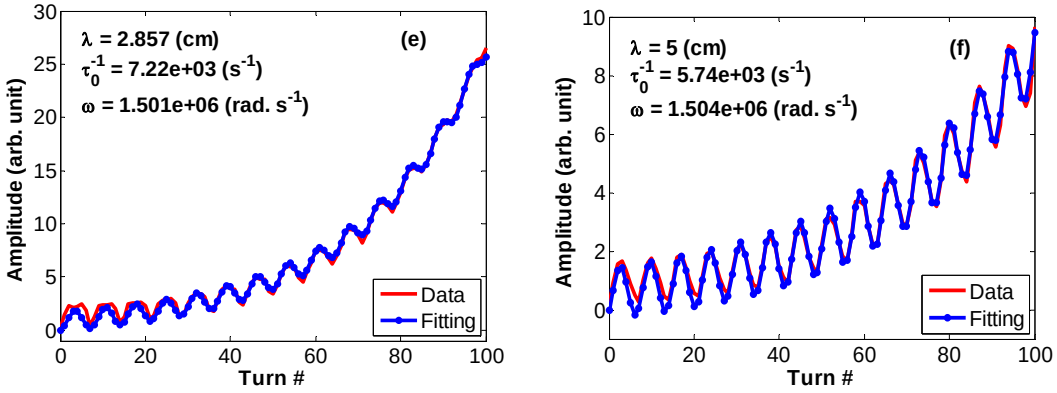

For the cases of λ=0.25 cm and λ=0.5 cm, since the oscillations are irregular, we choose the fitting function as

$$|\Lambda_1(t)| \approx \hat{\Lambda} e^{\frac{t}{\tau_0}}. \tag{4.55}$$

For the cases of λ =1 cm, 2 cm, 2.857 cm, 4 cm, and 5 cm, since there are obvious sinusoidal oscillations in line charge densities superimposed on exponential growths, we choose the fitting function as

$$|\Lambda_1(t)| \approx \hat{\Lambda} e^{\frac{t}{\tau_0}} + P e^{Qt/T_0} \cos(\omega t + \Phi), \tag{4.56}$$

where $\hat{\Lambda}$, P, Q, ω, Φ, and τ_0 are the fit coefficients, T_0 is the revolution period of H_2^+ ion, $t=N_t T_0$, N_t is the turn number, τ_0^{-1} is just the long-term instability growth rate. Note for beam energy of 19.9 keV, the nominal angular betatron frequency is ω_β=1.499×10^6 rad/s. The fitting results show the oscillations in the curves for λ =1.0 cm, 2.0 cm, 2.857 cm, and 5.0 cm are just the betatron oscillations, they are the dipole modes in the longitudinal structure of the beam due to dipole moment of the centroid offsets [20].

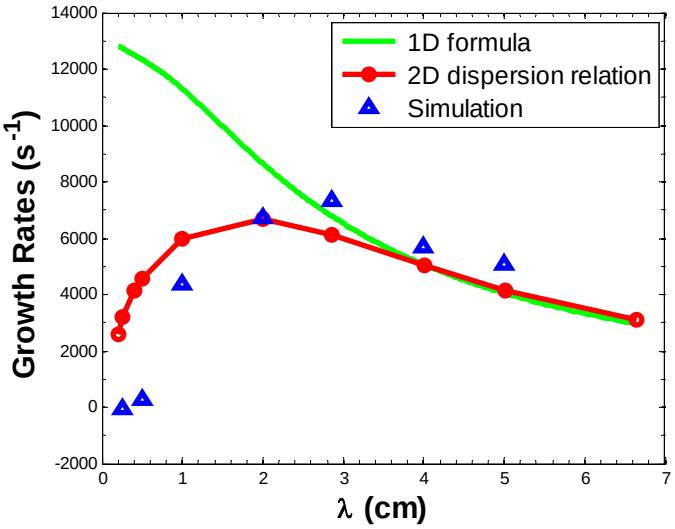

Figure 4.10: Comparison of the instability growth rates between theory and simulations for five runs of CYCO.

Figure 4.10 shows the comparison of the microwave instability growth rates between the theoretical values and the average simulation results for five runs of CYCO. Note that the theoretical values are predicted by the 1D formula of Eq. (4.1) with the slip factor expressed in Eq. (4.4) plus η_0, and the 2D dispersion relation of Eq. (4.41) with the space-charge modified tunes and transition gammas expressed in Eqs. (4.13)-(4.16). For both the 1D and 2D formalisms, the LSC impedances are calculated by Eq. (4.3), and the beam radii r_0 are calculated from the solution to the algebraic matched-beam envelope Eqs. (4.93) of Ref. [47]. Note that in Figure 4.10, the 1D formalism used in Refs. [14, 15] and the 2D dispersion relation have similar performance in prediction of the growth rates of the long-wavelength perturbations ($\lambda \geq 4$ cm), which are all consistent with the simulation results. For $\lambda < 2$ cm, the 1D formalism significantly overestimates the instability growth rates as $\lambda \to 0$ and cannot predict the fastest-growing wavelength ($\lambda \approx 2$ cm) correctly, because Eq. (4.1) neglects the Landau damping effects of finite emittance and energy spread; while the 2D dispersion relation, with the Landau damping effects

taken into account, has a much better performance than the conventional 1D formula in prediction of instability growth rates in the short-wavelength limits (λ<2 cm) and the fastest-growing wavelength, though there still exist some bigger discrepancies between the simulations and theory for very short wavelength λ<1 cm. Therefore we can see the Landau damping is a necessary mechanism to explain the low instability growth rates of the short-wavelength perturbations (λ is less than or comparable to r_0), which cannot be explained by the conventional 1D formalisms. Only at larger wavelengths ($\lambda >> r_0$) will the 1D and 2D dispersion relations have the similar performance.

4.4.2 Growth rates of instability with variable beam intensities

In order to study the dependence of microwave instability growth rates on initial beam intensities, simulations using CYCO are carried out for SIR beams with E_{k0} = 19.9 keV, σ_E= 0 eV, τ_b = 300 *ns* ($L_b \approx$40 cm), $\varepsilon_{x,0}=\varepsilon_{y,0}=50\pi$ mm mrad, I_0 =0.1, 0.3, 0.5, 5.0, and 20 μA, respectively. The initial distributions are uniform in both the 4-D transverse phase space (x, x', y, y') and the longitudinal charge density. The simulation for each intensity level is performed five times using five different initial micro-distributions, and the average simulated growth rates of the selected perturbation wavelengths of the five runs are used in analysis. For I_0 >20 μA, due to fast development of beam instability, the beam dynamics may enter the nonlinear regime only after several turns of coasting. This makes the fitting work difficult and inaccurate, therefore the simulation results for the intensities of I_0 >20 μA are not available in this paper.

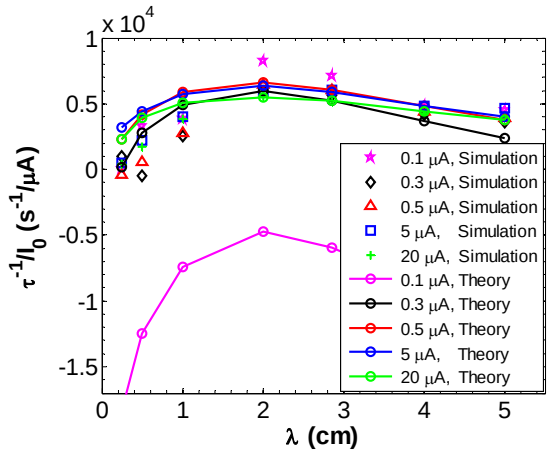

Figure 4.11: Comparisons between the simulated and theoretical normalized instability growth rates for different beam intensities.

Figure 4.11 shows the comparisons between the simulated and theoretical normalized instability growth rates for beam intensities ranging from 0.1 μA to 20 μA. We can see, except for I_0=0.1 μA, the theoretical normalized growth rate curves roughly overlap each other within a region. The theory and simulations are roughly consistent to each other for λ >2 cm and 0.3 μA$\leq I_0 \leq$ 20 μA. For λ < 2 cm, the discrepancies between the simulation and theory become bigger.

4.4.3 Growth rates of instability with variable beam emittance

In order to study the dependence of microwave instability growth rates on initial beam emittance, simulations using CYCO are carried out for SIR beams with E_{k0}=19.9 keV, σ_E=0 eV, τ_b=300 *ns* ($L_b \approx$ 40 cm), I_0=1.0 μA, $\varepsilon_{x,0}=\varepsilon_{y,0}=30\pi$ mm mrad, 50π mm mrad and 100π mm mrad, respectively. The code CYCO is run up to 100 turns and the growth rates are fitted by proper functions. For each initial emittance, the average growth rates of five runs with different initial micro-distributions are used in the analysis. Figure 4.12 shows the comparisons of growth rates between theory and simulations. We can see for λ>1.0

cm, the simulated and theoretical instability growth rates are consistent with each other, the larger emittance may help to suppress the instability growth rates. While for λ<1.0 cm, the discrepancies between the simulation and theory become bigger.

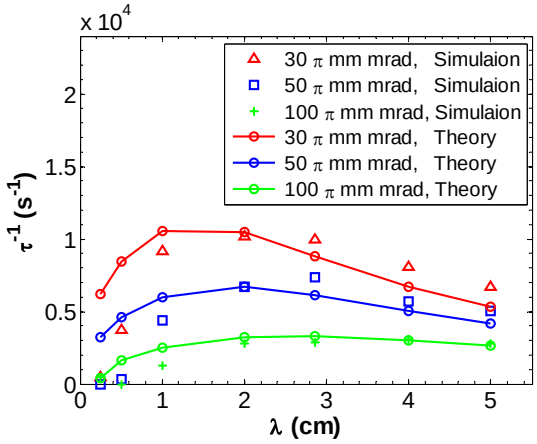

Figure 4.12: Comparisons of microwave instability growth rates between theory and simulations for variable initial emittance.

4.4.4 Growth rates of instability with variable beam energy spread

Figure 4.13 shows the comparisons of growth rates between theory and simulations for SIR beams with E_{k0}=19.9 keV, τ_b=300 *ns* (L_b≈40 cm), I_0=1.0 μA, $\varepsilon_{x,0}$=$\varepsilon_{y,0}$=50 mm mrad, σ_E=0, 50, and 75 eV, respectively. The code CYCO is run up to 100 turns and the growth rates are fitted by proper functions. For each initial RMS energy spread σ_E, the average growth rates of five runs with different initial micro-distributions are used in the analysis. We can see for λ>2.0 cm, the simulated and theoretical instability growth rates are consistent with each other, the larger energy spread may help to suppress the instability growth rates. While for λ<2.0 cm, the discrepancies between the simulation and theory become bigger.

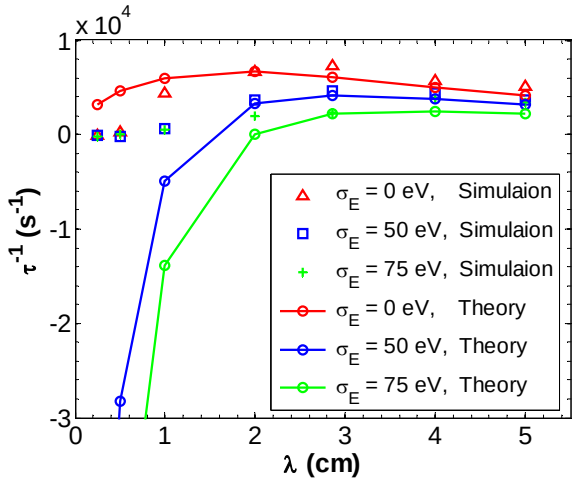

Figure 4.13: Comparisons of microwave instability growth rates between theory and simulations for variable uncorrelated RMS energy spread.

4.4.5 Possible reasons for the discrepancies between simulations and theory in the short-wavelength limits

Figures 4.10- 4.13 show there exist bigger discrepancies between the theoretical and simulated instability growth rates in the short-wavelength limits (especially for $\lambda \leq 1.0$ cm), they may be caused by one or some of the following reasons:

(a) Deviation from the beam model.

The 2D dispersion relations Eqs. (4.30) and (4.41) are derived from the unperturbed Gaussian beam distribution described in Eqs. (4.17) and (4.18), which can be rewritten as product of three Gaussian distribution functions

$$f_0 = \frac{n_b}{(2\pi)^{\frac{3}{2}}\varepsilon_{x,0}\sigma_\delta}\exp(-\frac{x_0^{\ 2}}{2\varepsilon_{x,0}\hat{\beta}_0})\exp[-\frac{(x_0')^2}{2\frac{\varepsilon_{x,0}}{\hat{\beta}_0}}]\exp[-\frac{(\delta+\hat{u}z_0)^2}{2\sigma_\delta^2}]. \qquad (4.57)$$

The model assumes the transverse phase space (x_0, x_0') is centered at ($\langle x_0\rangle$=0, $\langle x_0'\rangle$=0). For storage rings, the assumption of the linear chirp factor $\hat{u}=0$, the compression factor $C(s)$=1 are also used in the derivations. Therefore the coherent fractional momentum

deviation $<\delta_0>=<\delta+\hat{u}z_0>=<\delta>=0,$ and there is no correlation between the transverse and longitudinal distributions. The initial unperturbed distribution function described in Eq. (4.57) is just the product of three normal distribution functions with zero-mean. While as the beam coasts in the ring, there will be local centroid offset $<x_0>$ induced by the coherent fractional momentum deviation $<\delta_0>$ due to dispersion function D:

$$< x_0 >= \mathrm{D} < \delta_0 > . \tag{4.58}$$

In addition, when sinusoidal centroid wiggling takes place due to space charge force, the correlated fractional moment deviation $\hat{u}z_0$ should be replaced by a sinusoidal function of z_0, then the compression factor $C(s)\neq 1$ and will be dependent on s or t. The non-zero $<x_0>$, $<\delta_0>$ and non-constant, s-dependent compression factor $C(s)$ will shift the centers of beam distributions in the longitudinal and transverse phase space, produce a radial-longitudinal correlation in distribution function. Consequently, the 2D dispersion relations (4.30) and (4.41) will be modified, the amplitude of perturbed harmonic line density $|n_{1,k}(z,t)|=|g_k(t)|$ described in Eq. (4.34) should be replaced by $|n_{1,k}(z,t)|=|C(t)g_k(t)|$ too. This may cause the bigger discrepancies between the theoretical and simulated instability growth rates in the short-wavelength limits.

(b) Curvature effects

The LSC impedance, space-charge modified betatron tunes and transition gammas are all derived for an infinite long, straight beam model, while the SIR consists of four 90^o bending magnets which account for about 43% of the ring circumference. When the beam enters these bends, the curvature effects on the longitudinal and transverse beam dynamics are not taken into account in the theoretical analysis.

(c) LSC fields of the dipole mode

The centroid wiggling may induce the LSC fields of the dipole mode which are neglected in the theoretical analysis.

(d) Spectral leakages

In the data analysis, the line charge density perturbations around the fastest-growing wavelength ($\lambda \approx 2.0$ cm) have larger amplitudes comparing to the modes with smaller growth rates, and the FFT analysis is applied to a bunch with finite length using rectangular window. The fastest-growing modes may inevitably create the new frequency components (false spectrum) spreading in the whole frequency domain, namely, the so-called spectral leakages. The leaked spectra from the faster-growing modes may mix with and mask the real spectra of the slower-growing modes, therefore lower the resolutions of the FFT analysis results.

(e) Initial distribution

In Figures 4.12 and 4.13, because the beams with uniform longitudinal charge density are used in the simulations, their residual line charge modulation amplitudes are vanishingly small (theoretically speaking, they should be 0 in ideal conditions). When the growth rates in short-wavelength limits are negative due to larger beam emittance and energy spread, they can hardly be detected since the initial density modulation amplitudes have reached minima already.

In summary, the bigger discrepancies between the theoretical and simulated instability growth rates in the short-wavelength limits may be caused by various reasons. Due to complexity of the problem, for the time being, further discussions are not available in this dissertation.

4.5 Conclusions

Due to space charge effects and radial-longitudinal coupling, an ideally isochronous ring becomes a quasi-isochronous ring, which may result in the microwave instability and a finite revolution frequency spread. The relative motions among particles along the azimuthal direction are not frozen completely. The Landau damping mechanism still takes effect and may suppress the microwave instability in the isochronous regime.

A modified 2D dispersion relation is introduced to discuss the Landau damping effects for a coasting beam in the isochronous regime. The radial-longitudinal coupling transfer matrix elements R_{51} and R_{52} are included in the 2D dispersion relation. These elements can modify the coherent slip factor, together with $R_{56,}$ they also provide an exponential suppression for the instability growth rates of a beam with finite energy spread and emittance by Landau damping effects. The 2D dispersion relation is benchmarked by simulation code CYCO for bunches with variable initial beam intensities, energy spread and emittance. The theory agrees well with the numerical simulations for perturbation wavelengths of λ>2.0 cm. While for λ<2.0 cm, the discrepancies between simulations and theoretical predictions become larger. The possible reasons for the discrepancies are pointed out and discussed. By comparisons, the 2D dispersion relation has a better performance than the conventional 1D growth rate formula; the latter significantly overestimates the growth rates in the short–wavelength limit $\lambda \to 0$ and is incapable of predicting the correct fastest-growing wavelength.

In summary, the Landau damping effect is a necessary and important mechanism for an accurate prediction of the instability growth rates of the short-wavelength perturbations and the fastest-growing wavelength.

Chapter 5

DESIGN AND TEST OF ENERGY ANALYZER[3]

5.1 Introduction

Due to the repulsive space charge force, an initially monoenergetic bunch will develop energy spread among the beam particles when the bunch coasts in a storage ring. For the evolutions of the microwave instability and beam distribution, the development of the energy spread plays an important role and need to be measured accurately. For this purpose, SIR Lab has constructed a compact, high resolution electrostatic retarding field energy analyzer (RFA) with rectangular electrodes and a large entrance slit. This chapter will present the design and test of the energy analyzer.

5.2 Working principles and design considerations of the RFA

Because of the simple structure and high signal-to-noise ratios, an electrostatic RFA was chosen as the energy measurement device for the low energy SIR beam. The working principles of the generic electrostatic RFAs are simple: there is an electrode biased to a variable retarding voltage inside the analyzer (see Figure 5.1(a)), if the longitudinal component of the kinetic energy of an incident particle is no less than the peak of the retarding potential barrier, the particle can overcome the barrier and reach the current collector to form collector current. The energy profiles within the beam can be deciphered by analyzing the collector current as a function of the scanning retarding voltages V_1.

[3] The contents related to design and testing of energy analyzer of this chapter is written based on Ref. [19].

There are several types of RFA which are commonly used in the energy measurements, for example, the parallel-plate analyzer, spherical condenser, Faraday cage, etc., for which Ref. [48] provided an excellent review.

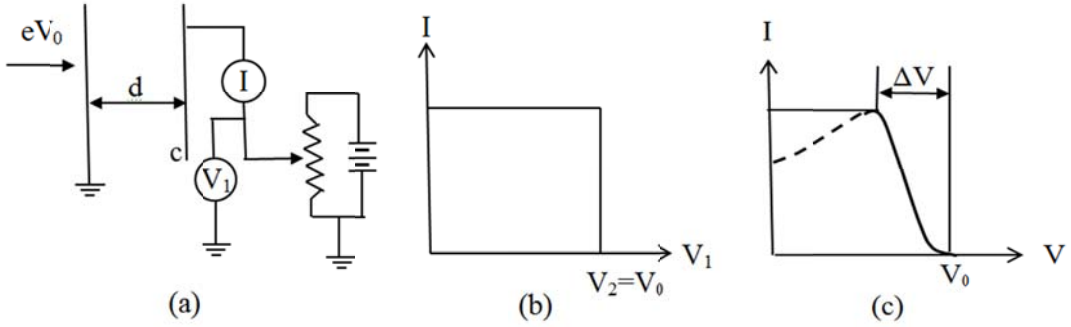

Figure 5.1: (a) Schematic of a basic parallel-plate RFA. (b) Ideal *I-V* characteristic curve with $V_2=V_0$ for monoenergetic particles (c) Usual *I-V* characteristic cutoff curve. The slope between $V=V_0-\Delta V$ and $V=V_0$ is due to the trajectory effect. The effect of secondary electron emission is shown in the dotted curve. (Note: the figure is reproduced from Ref. [48]).

In the design and operation of a RFA, special attention needs to be paid to some effects which may affect its resolution.

(a) Aperture lens effect

Let us assume a beam enters a decelerating field through an entrance aperture. The charge and kinetic energy of a single beam particle are e and eV_0, respectively. Due to the different field strengths before and after the aperture, the electric field lines in the vicinity of the aperture are bent towards the aperture. The particle with a radial offset with respect to the aperture axis sees a radial focusing force before the aperture and a defocusing one after the aperture. Since the particle's energy after the aperture is smaller than that before the aperture, the net effect is defocusing resulting in an increase of the divergence angle. This *aperture lens effect* can be characterized by a focal power [48] as

$$1/f = (E_2 - E_1)/4V_0, \tag{5.1}$$

where E_1 and E_2 are the field strength before and after the entrance aperture. Ref. [47] provides a detailed derivation for Eq. (5.1).

(b) Trajectory effect

Only the longitudinal component of the kinetic energy is effective to overcome the retarding potential. For example, among the existing analyzers, the simplest one is the primitive two-element parallel-plate analyzer (see Figure 5.1(a)). This type of RFA has a good resolution only when the trajectories of the beam are parallel to the analyzer axis. In this case, for a monoenergetic beam with initial kinetic energy eV_0, the ideal *I-V* (current signal v.s regarding voltage) characteristic curve of the analyzer is similar to a step function with a sharp cutoff at V_2=V_0 (see Figure 5.1(b)). In reality, due to the initial beam emittance, the aperture lens effect, space charge effect and misalignment, the moving directions of the particles inside the analyzer usually have finite nonzero slopes with respect to the analyzer axis. Then the actual *I-V* curve for a monoenergetic beam may look like that in Figure 5.1(c), where the curve begins to drop at V=V_0-ΔV. This may result in a poor resolution of the parallel-plate analyzer $\Delta V/V_0$ typically in the range of 10^{-3}-10^{-2}. In order to suppress this *trajectory effect* and expansion of beamlet due to space charge effect, a focusing electrode is usually introduced in the analyzer between the entrance aperture and the retarding electrode; another option is to choose a special multifunctional retarding/focusing electrode that can decelerate and focus the sampled beamlet at the same time.

(c) Secondary electron emission

When the charged particles bombard the metal current collector, a fraction of the

kinetic energy of the incident particles will transfer to the electrons of the collector surface. Hence, some electrons will be knocked out of the metal surface. This phenomenon is termed *secondary electron emission*. This effect may cause a deformation of the plateau of *I-V* characteristic curve as shown by the dotted line in Figure 5.1(c), if the primary particles are negatively charged. For positive primary particles, the ascending dotted curve in Figure 5.1(c) should be replaced by a descending one. These secondary electrons may yield false current signals and resolution degradation, thus must be suppressed. According to Ref. [49], when a positive ion with mass M and kinetic energy eV hits a metal surface of work function ϕ, the maximum kinetic energy of the secondary electron is

$$\mathrm{E}_{\max} = e[(4m/M)4V + V_i - \phi], \tag{5.2}$$

where V_i is the ionization potential of the neutral atom of the ion species. Usually the initial kinetic energy of the secondary electrons is low. Hence, introduction of an electron suppressor biased to a low voltage can suppress the secondary electron emission effectively.

(d) Elastic reflection

Even if the kinetic energy of the beam particles hitting the collector is high, not all of them can be captured by the collector to form current signals. After collisions with the metal surface, some 'naughty' particles will be reflected backward elastically with almost the same energies as those of the primary particles. These rebounded particles usually have a cosine angular distribution about the normal direction of the collector surface. In order to suppress this effect, a Faraday cage or a *C*-shaped collector with an opening

facing the incident particles can be adopted in the design. The rebounded particles may experience several collisions on the collector surface with grazing incidence and reflection before final capture.

(e) Space charge effect

When the intensity of the sampled negative (positive) particles inside the analyzer is higher than a critical value, the induced space charge effect is so strong that a potential dip (bump) can be formed which can reflect the incident particles. The measured energy spectrum will have a long tail at the higher energy side with the mean energy shifting toward the low energy side. This effect is shown in Figure 5.2 for the energy measurement results of electron beamlets with different currents obtained at the University of Maryland Electron Ring (UMER) [50]. In order to avoid this *space charge effect*, the energy measurement should always be performed below the critical intensity.

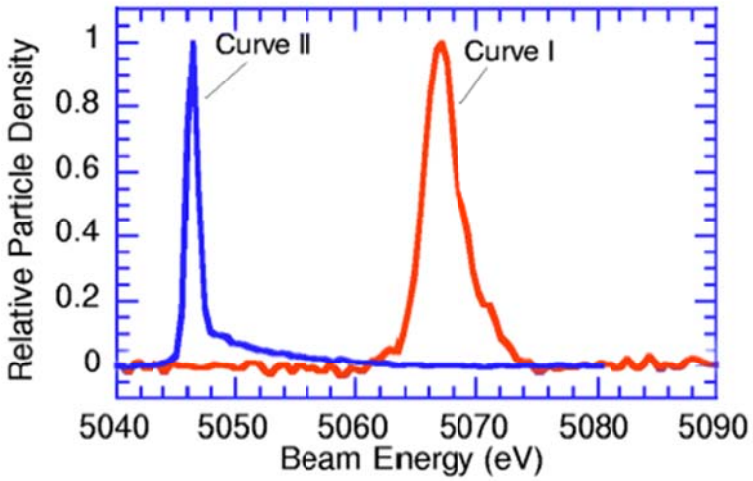

Figure 5.2: Comparison of the measured energy spectra for electron beamlet with two different currents inside the analyzer. Curve I is for the current of 0.2 mA, the RMS energy spread is 2.2 eV; Curve II is for the current of 2.6 mA, the RMS energy spread is 3.2 eV. (Note: the figure is cited from Ref. [50]).

5.3 Design requirements for the SIR energy analyzer

The SIR energy analyzer is required to be able to scan across the beam horizontally (radially), so that the radial distribution of the energy spread of a deflected bunch at a chosen number of turns after injection can be measured. It is installed under the median plane in the Extraction Box or Measurement Box (see Figure 5.3) to replace the Sector Fast Faraday Cup. The entrance plate of the analyzer is tilted at an angle (about 10^{o}) with respect to the vertical plane to align the analyzer axis parallel to that of the deflected beam. The design parameters of the SIR energy analyzer are shown in Table 5.1.

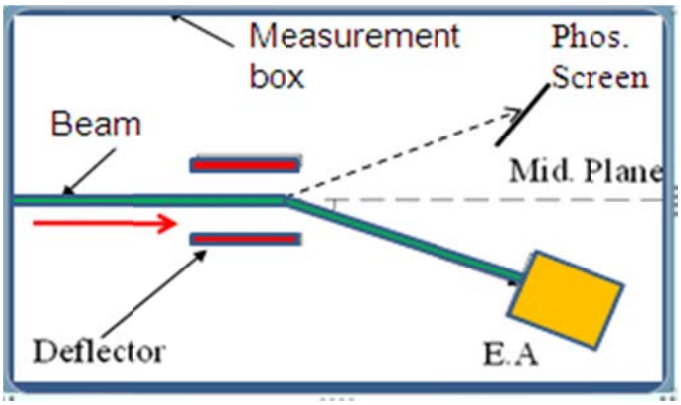

Figure 5.3: A Schematic of the Measurement Box. 'Phos. Screen', 'E. A' and 'Med. Plane' stand for the 'Phosphor Screen', 'Energy Analyzer' and 'Median Plane', respectively.

Table 5.1: Design parameters of the SIR Energy Analyzer

Ion species	H_2^+
Beam energy	20 keV
Beam current	0-30μA
Beam emittance	10π mm*mrad
Energy change (due to space charge)/turn	7-8 eV
Beam radius	5 mm

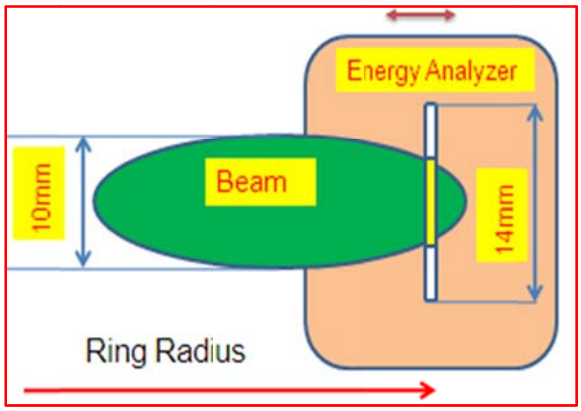

Figure 5.4: A schematic of the SIR energy analyzer with a horizontally (radially) expanded beam. The beam (green oval) is moving towards the analyzer (into the paper). The analyzer can scan back and forth along the ring radius. The thin yellow rectangle in the middle of the analyzer depicts a sampled beam slice or beamlet.

Figure 5.4 depicts the schematic of the SIR energy analyzer. A horizontally (radially) expanded beam (green oval) due to space charge effect and dispersion function is also shown in the plot. The beam is moving into the paper. This figure shows a scenario of the spatial relation between the energy analyzer and the beam in the measurement, if we follow behind the beam and watch along its moving direction towards the analyzer. The beam size of SIR is about 10 mm in diameter and the beam peak current is only on about 10 μA level (outside the analyzer for a DC beam). In order to sample as much beam as possible, we adopted a 14 mm (vertical) $\times$ 1 mm (horizontal) rectangular slit as the entrance aperture instead of a conventional small hole (Figure 5.4). This asymmetric, large entrance aperture makes the design work more challenging.

5.4 A brief introduction to the UMER analyzer

The University of Maryland has designed the 2^{nd} and 3^{rd} generation compact, high resolution cylindrical RFAs to measure the energy spread of the electron beam in UMER.

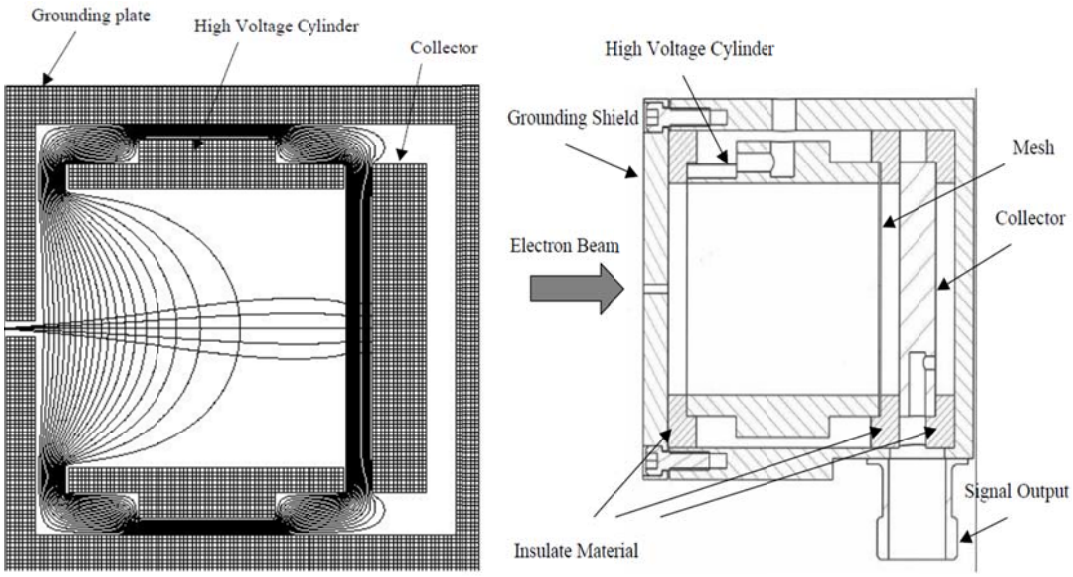

Figure 5.5: Schematic of the 2nd generation UMER energy analyzer. (a) Field model and simulated trajectories (left). (b) Mechanical structure (right). (Note: the figures are cited from Ref. [51]).

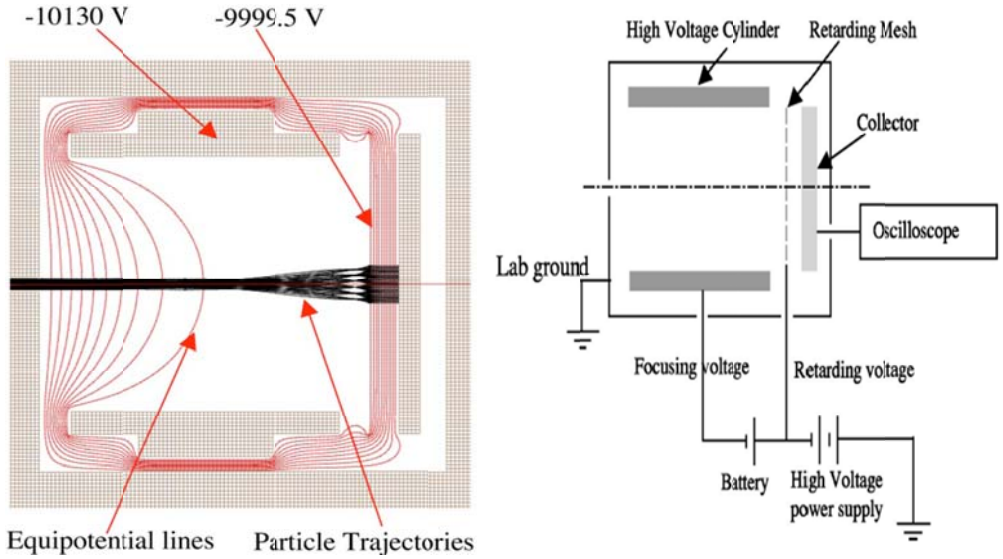

Figure 5.6: Schematic of the 3rd generation UMER energy analyzer. (a) Field model and simulated trajectories (left). (b) Electronic circuit (right). (Note: the figures are cited from Ref. [52]).

Figure 5.5 illustrates the diagram of the 2nd generation UMER analyzer [51]. The left plot shows the field model, equipotential lines, and beam trajectories simulated by the code SIMION [53]; the right plot depicts its mechanical structure. Figure 5.6 illustrates the diagram of the 3rd generation UMER analyzer [52]. The left plot shows the field model, equipotential lines, and beam trajectories simulated by the code SIMION; the right plot depicts its electronic circuit. Both analyzers have cylindrical housing tube, entrance plate with a circular entrance hole, focusing cylinder, retarding mesh, and current collector in common. The only difference is that in the 2nd generation analyzer, the retarding fine mesh is soldered to the focusing cylinder and they always keep the same retarding voltage; while in the 3rd generation analyzer, the retarding mesh is shifted away from the focusing cylinder's end plane by several millimeters, and an extra low voltage power supply is employed to produce a variable focusing voltage between them.

The working principles of the two analyzers are similar: if an electron beam enters the analyzer through the entrance aperture, it will be decelerated and focused by the retarding field produced by the focusing cylinder and the retarding mesh. The curved equipotential lines can decelerate and focus the beamlet at the same time. Only those electrons whose kinetic energies are higher than the retarding voltage can pass through the retarding mesh to form current on the collector. By changing the retarding voltage on the mesh and analyzing the change of collector current as a function of retarding voltage, the energy profile of the primary beam can be obtained. The 3rd generation analyzer has a better resolution, because it can minimize the coherent errors further by providing an extra focusing for the electrons in the vicinity of the retarding mesh, where they have exhausted most of their kinetic energies. Note that in the 2nd generation UMER analyzer,

for an ideal retarding mesh consisting of infinitely thin wires with an infinitely large wire density (number of wires in a unit length) and 100% transmission rate, the retarding point (position where the retarding potential has maximum magnitude) of the analyzer should be on the plane of the retarding mesh; while in reality, due to the finite wire density and the difference of the longitudinal potential gradients in the vicinity of the mesh plane, the potential distribution on the mesh plane is not uniform. The potentials in the void region enclosed by the mesh wires are different from the retarding voltages applied on the wires. Therefore, the actual resolution of the 2^{nd} generation UMER analyzer should be dependent on the wire density. While for the 3^{rd} generation UMER analyzer, due to the low focusing voltage applied between the focusing cylinder and the retarding mesh, the retarding point is located at several millimeters before the mesh plane. Hence, the actual resolution of the 3^{rd} generation analyzer is not sensitive to the wire density. For the UMER analyzers, because the electric field between the retarding mesh and the collector is a natural decelerating field for the possible secondary electrons emitting from the collector, it is not necessary to adopt the secondary electron suppressors.

5.5 Design of the SIR energy analyzer

A thin 14 mm × 1 mm rectangular slit has been chosen as the entrance aperture for the SIR analyzer for the sake of better signal-to-noise ratio. Due to the large aspect ratio of the beamlet sampled by the SIR analyzer, it is impossible to apply an extra focusing voltage between the retarding/focusing tube and the retarding mesh to fine-tune the focusing strength in both the horizontal and vertical planes at the same time like the 3^{rd} generation UMER analyzer. In the end, we use the 2^{nd} generation UMER analyzer as the

main design reference for the SIR analyzer.

From emittance measurement, the divergence angles of the primary SIR beam in the horizontal and vertical planes are found to be roughly the same. In order to focus the particles at the edges of the sampled beamlet inside the analyzer with the same focusing strength in both planes for optimum resolution, the contour of the equipotential lines in any planes normal to the analyzer axis must be a family of concentric rectangles, of which the aspect ratios should be similar to that of the sampled beamlet in the retarding/focusing region. This requires both the retarding/focusing electrodes and the housing of SIR analyzer must have rectangular cross-section.

Due to the much higher particle energy (which is equal to the retarding/focusing voltage times unit charge), and the much larger vertical dimensions of the beamlet sampled by the SIR analyzer than those of the electron beamlet sampled by the UMER analyzer, the distance between the retarding mesh and the entrance plate of the SIR analyzer must be much shorter than that of the UMER analyzer to get a proper focusing for the SIR beamlet, otherwise the particles will be over-focused yielding poor resolution. In addition, in the SIR analyzer, since the electric field between the retarding mesh and the collector is an accelerating field for the possible secondary electrons escaping from the collector surface, a secondary electron suppressor which is biased to a negative voltage should be introduced between the retarding mesh and the collector. For the above reasons, the longitudinal potential gradient between the retarding mesh and entrance plate of the SIR analyzer is much higher than that of the UMER analyzer, especially in the vicinity of the retarding mesh plane. This makes the resulting analyzer resolution highly dependent on the mesh wire density. Considering both the transmission rates and wire

density, finally, we choose a Nickel mesh with 1000 lines per inch (LPI=1000) and 50% transparency rate in our design.

Though the working principles of the SIR and UMER analyzers (2^{nd} generation) are similar to each other, they differ on many aspects as summarized in Table 5.2.

Table 5.2: Comparisons between the UMER (2^{nd} generation) and SIR Analyzers

	UMER Analyzer	**SIR Analyzer**
Extraction	Single pass	Variable turns
Particles	e^-	H_2^+
Beam energy	up to 10 keV	up to 20 keV
Entrance aperture	1-mm hole	14mm×1mm slit
Electrodes	Cylindrical tubes	Rectangular tubes
Secondary e^- suppressors	No	Yes
Working mode	Static	Scanning
Beam current	mA	nA

Due to the complicated 3D electric field inside the analyzer and the large height of the beamlet in the vertical plane, it is impossible to perform the theoretical design calculation accurately using the theory of paraxial beam optics. The physical design of the analyzer can only be carried out by the numerical methods. We choose to use SIMION 8.0 [53], an electric field design and simulation code, in our design work.

The SIR analyzer mainly consists of the following parts: (1) a housing box with an entrance slit on the front plate. (2) retarding/focusing tube and fine mesh. (3) secondary electron suppressor. (4) current collector. (5) four ceramic insulators between the above electrodes and housing.

The resolution of the SIR analyzer is highly dependent upon the exact potential

distribution on and near the retarding mesh plane, which is nonuniform due to the finite wire density. Because of the high calculation workload, it is impossible to set up a mesh model containing all the wires of the entire piece of retarding mesh in the simulation. To deal with this problem, a small sample of the real mesh model with high resolution is set up as shown in the left plot of Figure 5.7.

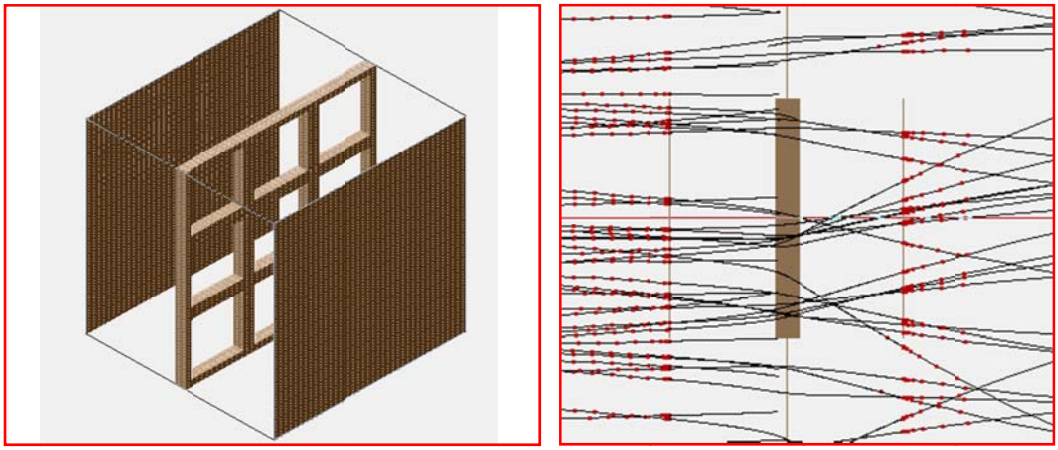

Figure 5.7: The movable small mesh model (left) and simulated particle trajectories (right).

The small mesh model consists of eight crossing wire segments placed midway between two plane boundaries with proper potentials calculated in advance. The two plane boundaries are separated by a short distance *d*. When an ion approaches the retarding mesh plane at a distance which is close to *d*/2, a short script written in the programming language Lua [54] embedded in SIMION can predict the possible impaction point and move the small mesh model there, so that the particle can pass though the small mesh model containing an accurate field distribution. In the trajectory simulation, a group of ions are shot towards the retarding mesh one by one. The small mesh sample moves along the whole retarding plane back and forth, so that the particles

can pass through it one by one (right plot of Figure 5.7). By this way, the trajectories near the whole real mesh can be simulated with a good resolution.

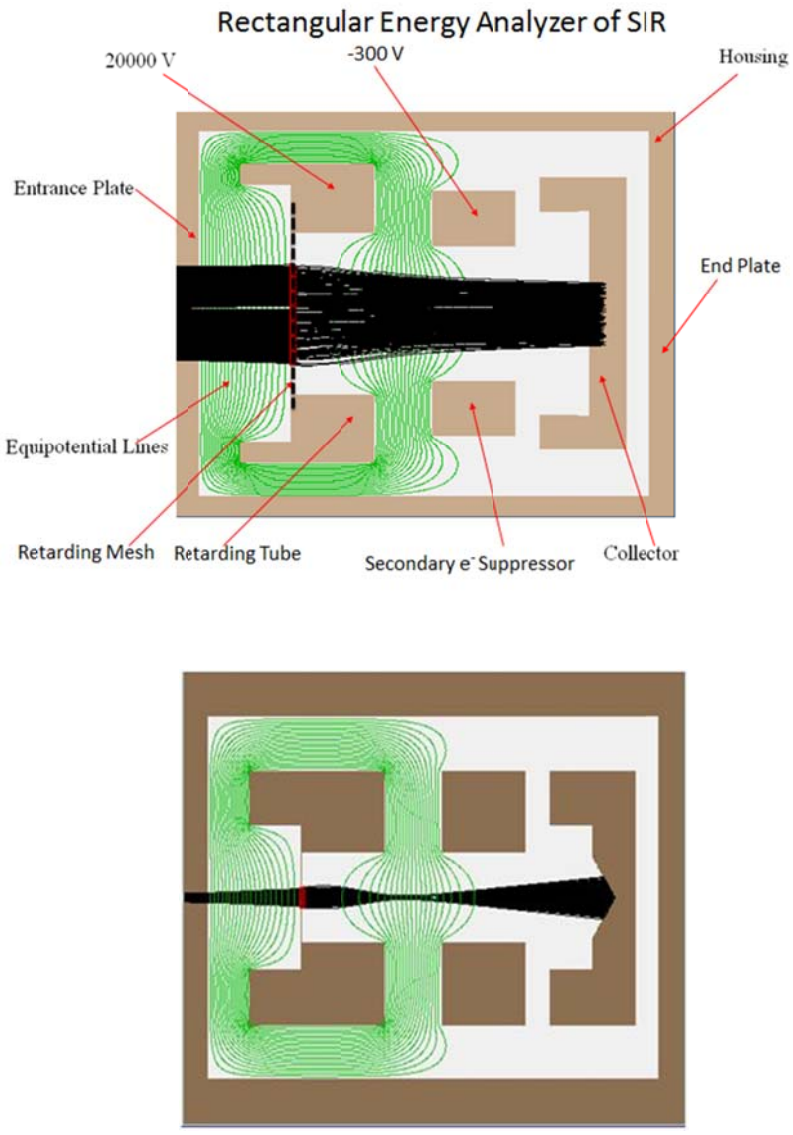

Figure 5.8: Two schematics of the SIR energy analyzer and particle trajectories simulated by SIMIOM, where the beam energy is 20.01 keV, the voltages of the regarding mesh and suppressor are $V_{retarding}$=20 kV and $V_{suppressor}$=-300V, respectively.

The electrodes, equipotential lines (green lines), and the trajectories (black lines) of some typical ions in the SIR analyzer simulated by SIMION are shown in Figure 5.8.

The retarding mesh is soldered to the multifunctional retarding/focusing tube. The electric field formed between the retarding/focusing tube and the entrance plate can focus and decelerate the beamlet; the thick part of the retarding/focusing tube behind the retarding plane is designed for two purposes: (a) improve the analyzer resolution by improving the uniformity of potentials in the vicinity of and right behind the retarding mesh. (b) focus the beam to counteract the defocusing effects induced by the secondary electron suppressor downstream, otherwise the transverse beam size will be too big to be accommodated by the collector. According to Eq. (5.2), the estimated maximum kinetic energy of the secondary electrons for a 20 keV H_2^+ beam is only several tens of eV. A suppressor biased to -300 V is enough to repel these electrons back to the collector. The current collector is a *C*-shaped stainless steel electrode with a *V*-shaped grove in the middle, which is designed to reduce the current loss due to the elastic head-on collisions between the ions and the collector.

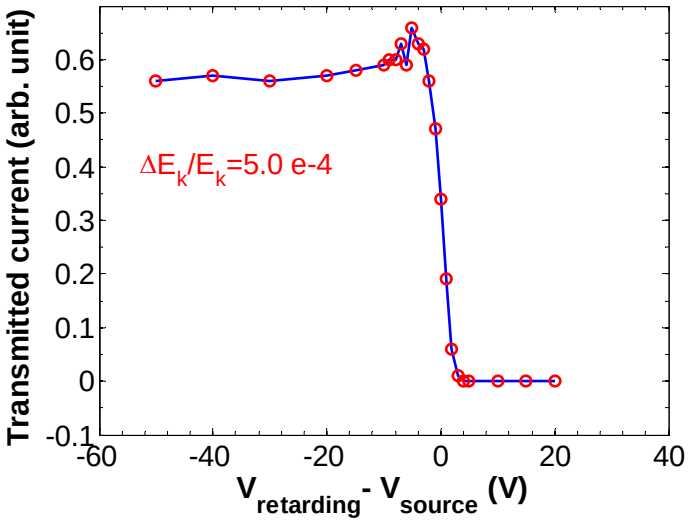

Figure 5.9: Performance of the SIR analyzer simulated by SIMION 8.0 for a fixed retarding potential $V_{retarding}$ =20 kV and variable source voltage V_{source}.

In the performance test by simulation, it is assumed that the beam particles are

monoenergetic and have uniform distribution at the entrance slit, and the initial moving directions of the ions have a uniform distribution within a cone with half angle of 10 mrad. The retarding voltage is fixed to 20 kV, while the source voltage (or kinetic energy of beam) is variable. The simulation results in Figure 5.9 demonstrate that the simulated relative energy error or resolution is about 5.0×10^{-4}.

We also solve the sheet beam envelope equation [27] to study the resolution of the analyzer further. The calculation results indicate that the changes of beam current and emittance inside the analyzer have little effects on the analyzer resolution; this guarantees an almost constant resolution during the energy measurement.

Figure 5.10 shows the photos of the SIR analyzer with its parts. The analyzer is a 60 mm×60 mm×50 mm box, limited by the space available in the Extraction Box. The four white pieces are the ceramic insulators.

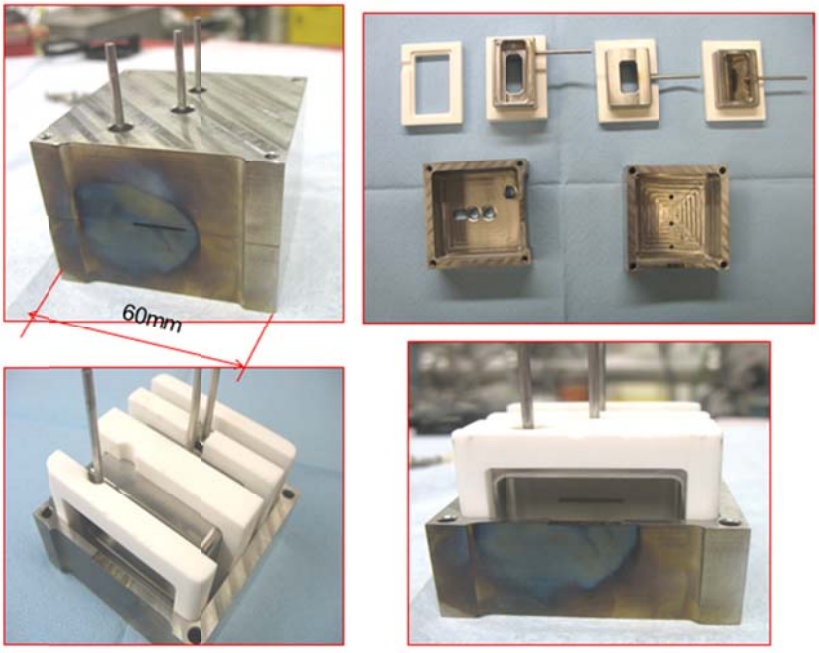

Figure 5.10: The photos of the SIR energy analyzer.

5.6 Experimental test of the SIR energy analyzer

We tested the performance of the SIR analyzer by using it to measure the beam energy at the ARTEMIS-B electron cyclotron resonance (ECR) ion source [55] beam line (see Figure 5.11) and SIR (DC beam, half a turn from injection to extraction) at NSCL.

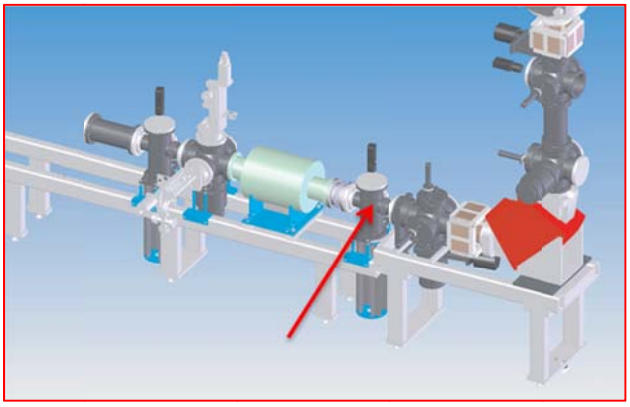

Figure 5.11: Schematic of the ARTEMIS-B Ion Source beam line. The performance test of the SIR analyzer was carried out in the diagnostic chamber indicated by the red arrow.

The resolution is estimated as the spread in retarding potential to go from 95% to 5% transmission. The experimental results indicate the overall relative energy errors tested at the ARTEMIS-B ECR ion source and SIR, including the alignment errors, energy spread of beam and resolution of the analyzer, are 1.0×10^{-3} and 1.3×10^{-3} respectively (see Figure 5.12 and Figure 5.13). The performance of analyzer meets our requirements for the future energy measurement. When we tested the analyzer by using pulsed beam of SIR (necessary to follow the temporal evolution of the energy spread), we found the signal-to-noise ratio is very low. The noise mainly originates from the high-speed, high-voltage switches used to control the different choppers, inflectors and deflectors. Finally we decided to use the integrated current signal to measure the energy spread of

SIR beam, which will be discussed in details in the next chapter.

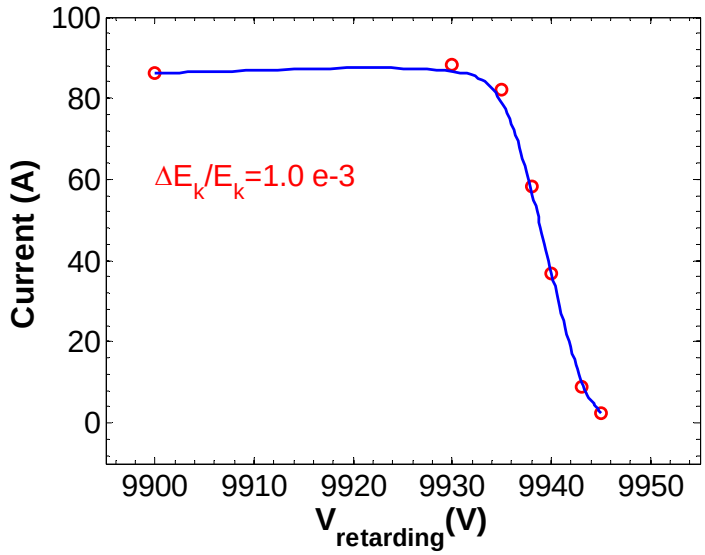

Figure 5.12: Performance of the SIR energy analyzer tested at ARTEMIS-B ECR ion source.

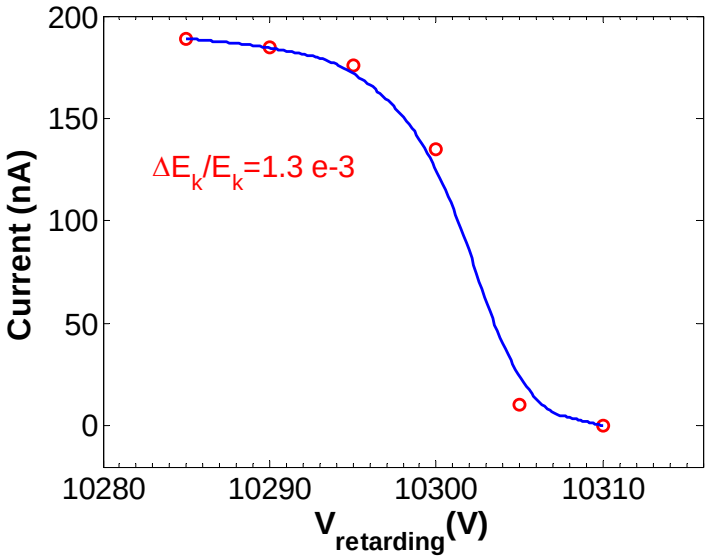

Figure 5.13: Performance of the SIR energy analyzer tested at SIR by DC beam.

5.7 Conclusions

A compact, high resolution retarding field energy analyzer has been designed and tested for SIR of NSCL at MSU to further study the beam instability. Experimental results indicate the performance of the analyzer meets the requirements for our future measurement and research work.

Chapter 6

NONLINEAR BEAM DYNAMICS OF SIR BEAM[4]

6.1 Introduction

When a high intensity uniform long H_2^+ bunch with a finite length is injected into the SIR, the nonlinear space charge forces in the beam head and tail are strong and may deform the beam shape. In addition, as the perturbation amplitude of the line charge density increases due to microwave instability, the beam dynamics of the central part of the beam also enters the nonlinear regime soon after injection. The bunch may break up into many small clusters longitudinally only after several turns of coasting [12, 13]. This chapter mainly discusses the nonlinear beam dynamics in these cases, including the study on evolution of energy spread, vortex motion, and merging of cluster pairs by experimental, simulation and analytical methods.

6.2 Measurement of the energy spread

Among the various beam parameters which govern the evolution of the bunched beam profiles, the energy spread induced by the space charge field plays an important role in both the linear and nonlinear regime of beam instability. It may help to suppress the microwave instability in the linear beam dynamics; in addition, it is also one of the important measures of the asymptotic bunch behavior in the nonlinear beam dynamics. For this reason, an accurate knowledge of the energy spread distribution and evolution of

[4] The contents regarding energy spread measurement and simulation is excerpted from Y. Li, L. Wang, F. Lin, Nuclear Instruments and Methods in Physics Research A 763, 674 (2014).

the bunched SIR beam becomes necessary. This section presents the experimental and simulation results of the energy spread of the SIR bunch and comparisons between them.

6.2.1 Energy spread measurement system

SIR lab has designed a compact electrostatic retarding field energy analyzer (RFA) which is introduced in Chapter 5. The schematic diagram of the energy spread measurement system is shown in Figure 6.1. It mainly consists of (a) energy analyzer with power supplies for the retarding mesh and secondary electron suppressor, (b) step motor and motor controller, (c) Preamplifier (model: TENNELEC TC-171), (d) Amplifier (model: TENNELEC TC-241S), (e) oscilloscope (model: LECROY LC684DXL). Figures 6.2-6.5 show the photos of the components of the measurement system.

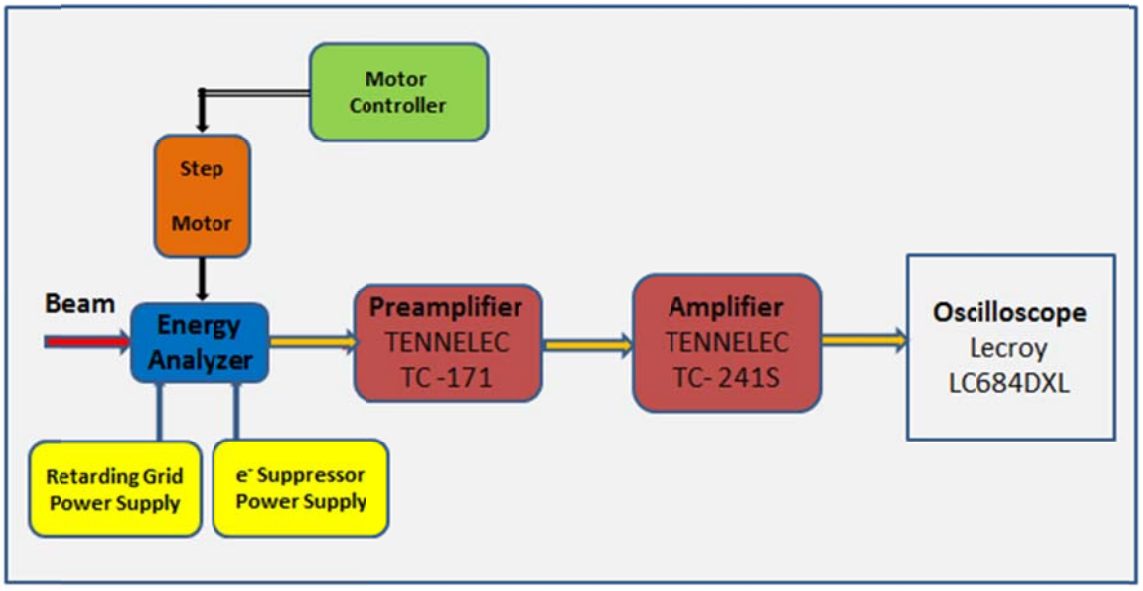

Figure 6.1: Schematic of the energy spread measurement system.

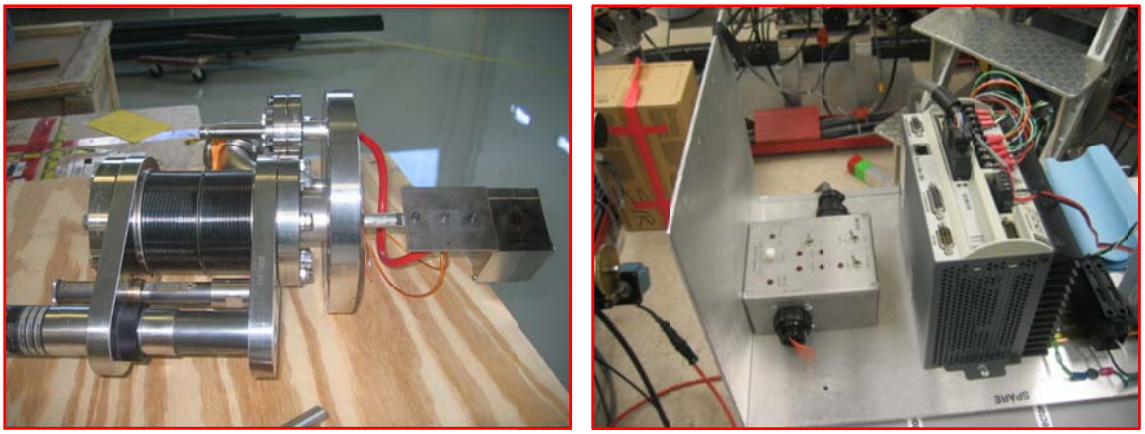

Figure 6.2: Energy analyzer assembly including the supporting rod, flange, and motor drive (left) and motor controller (right).

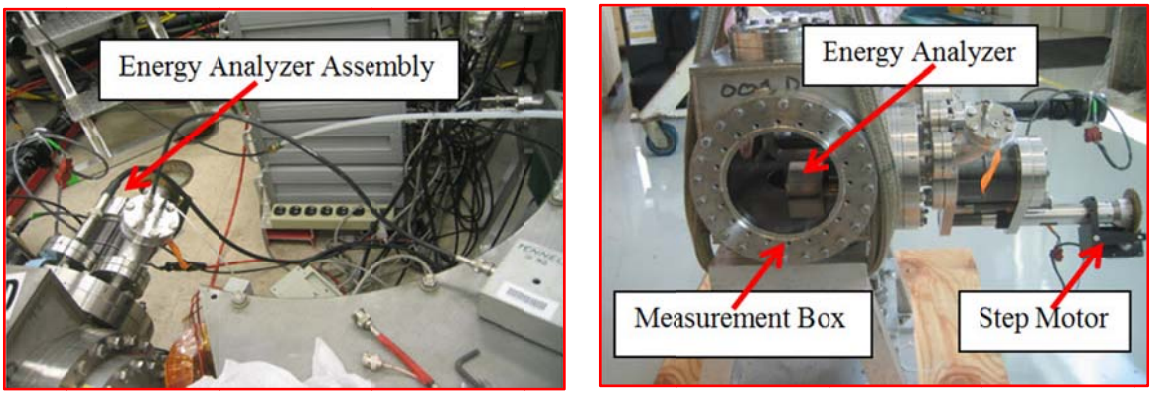

Figure 6.3: Energy analyzer assembly in the SIR (left) and a side view with the Extraction Box (right).

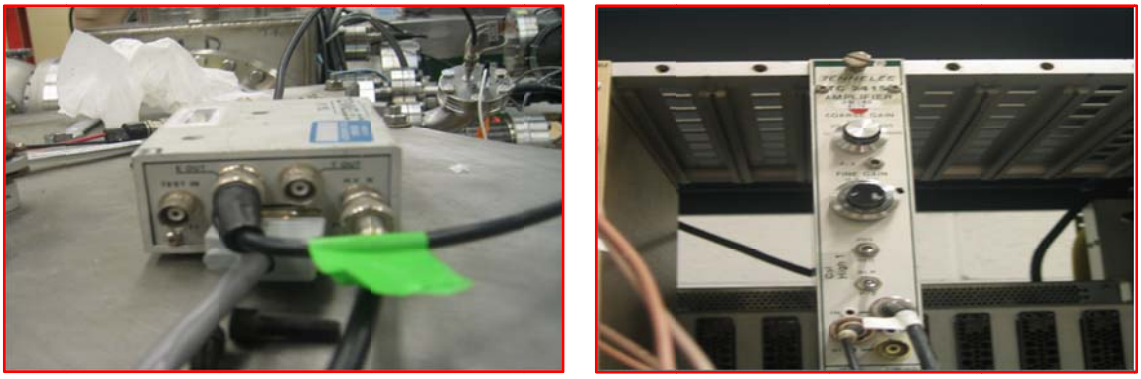

Figure 6.4: Preamplifier (TENNELEC TC-171) (left) and Amplifier (TENNELEC TC-241S) (right).

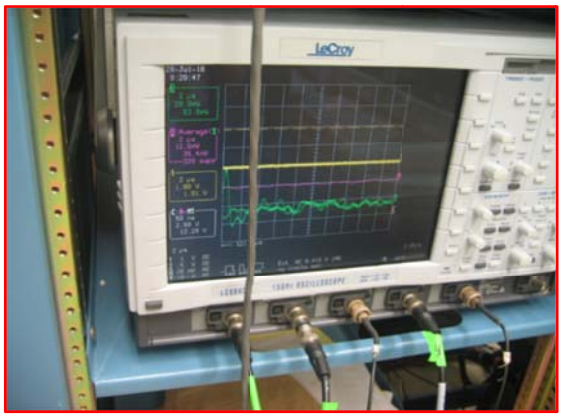

Figure 6.5: High voltage power supply (BERTAN 225) for the retarding grid (left) and oscilloscope (LeCroy LC684DXL) (right).

The energy analyzer is installed below the median ring plane in the Extraction Box (Measurement Box), and a pair of high-voltage pulsed electrostatic deflectors in the Extraction Box is used to kick the coasting beam down to the energy analyzer at a chosen turn number. The entrance plate of the analyzer is tilted at an angle (about 10^{o}) with respect to the vertical plane to align the analyzer axis parallel to the deflected beam (see Figure 6.3). Before the measurement of energy spread, we need to know the transverse beam profiles. The motor controller and step motor can drive the energy analyzer to scan across the beam transversely in the horizontal plane. By setting the retarding voltage of the analyzer to zero or a low value, most ions of the sampled beamlet can pass through the retarding mesh to reach the collector. The radial density profiles of the matched SIR bunch can be obtained. Usually the beam profile scanning is performed from turn 0 to turn 70 with an interval of five or ten turns. The energy spread measurement is carried out at three radial positions (measurement points): one is at the location of the peak beam current, and the other two are close to the beam core edges on each side. During the experiment, for each fixed radial position (measurement point) of the analyzer, the

retarding voltage is varied within a range in the vicinity of the nominal beam energy. The current signals on the current collector of the analyzer are amplified by the Preamplifier (TENNELEC TC-171) and Amplifier (TENNELEC TC-241S) consecutively. The amplified signals are sent to the oscilloscope (LeCroy LC684DXL), where the waveforms and strengths of the signals (in voltages) can be observed and read. After offline data analysis, the energy spread information of the beam can be obtained.

6.2.2 Data analysis of the energy spread

A H_2^+ ion bunch with the length 600 mm, peak current 8.0 μA, kinetic energy 10.3 keV is used in the energy spread measurements. The measured emittance is about 30π mm mrad. From the measurement, the raw *S*-*V* curves at the three radial positions (measurement points) and various turn numbers are obtained. Here *S* and *V* denote the signal strength and the retarding voltage, respectively. The top graph of Figure 6.6 shows an example of the measured raw *S*-*V* curve. For each fixed radial measurement point and turn number, the data analysis for the energy spread measurement is performed by the following procedure:

1. Subtract the residual noise signal from the raw *S*-*V* curve and normalize the adjusted *S*-*V* curve to 1. This procedure yields a transmission rate curve (*T*-*V* curve) ranging from 0 to 1.
2. Assuming the energy spread has a Gaussian distribution with deviation σ_E and mean energy of <*E*>,

$$P(E) = \frac{1}{\sqrt{2\pi}\sigma_E} e^{-\frac{(E-<E>)^2}{2\sigma_E^2}}, \tag{6.1}$$

then the transmission rate $T(V)$ at a given retarding voltage V is equal to the integral of $P(E)$ integrated for $E \geq V$, i.e.,

$$T(V) = \frac{1}{\sqrt{2\pi}\sigma_E}\int_V^{\infty} dE' e^{-\frac{(E'-<E>)^2}{2\sigma_E^2}} = \frac{1}{2}[1 - erf(\frac{V-<E>}{\sqrt{2}\sigma_E})], \quad (6.2)$$

where $erf(x) = \frac{2}{\sqrt{\pi}}\int_0^x e^{-t^2}\,dt$ is the error function. If the transmission rate curve is fitted to Eq. (6.2), the mean energy <E>, root mean square (RMS) energy spread σ_E and full width at half maximum FWHM=$2\sqrt{2ln2}\sigma_E \approx 2.355\sigma_E$ of the energy spread can be obtained.

3. Using the fitted parameters of <E> and σ_E, reconstruct the S-V curve and compare with the raw S-V curve, plot the fitted Gaussian curve of energy distribution.

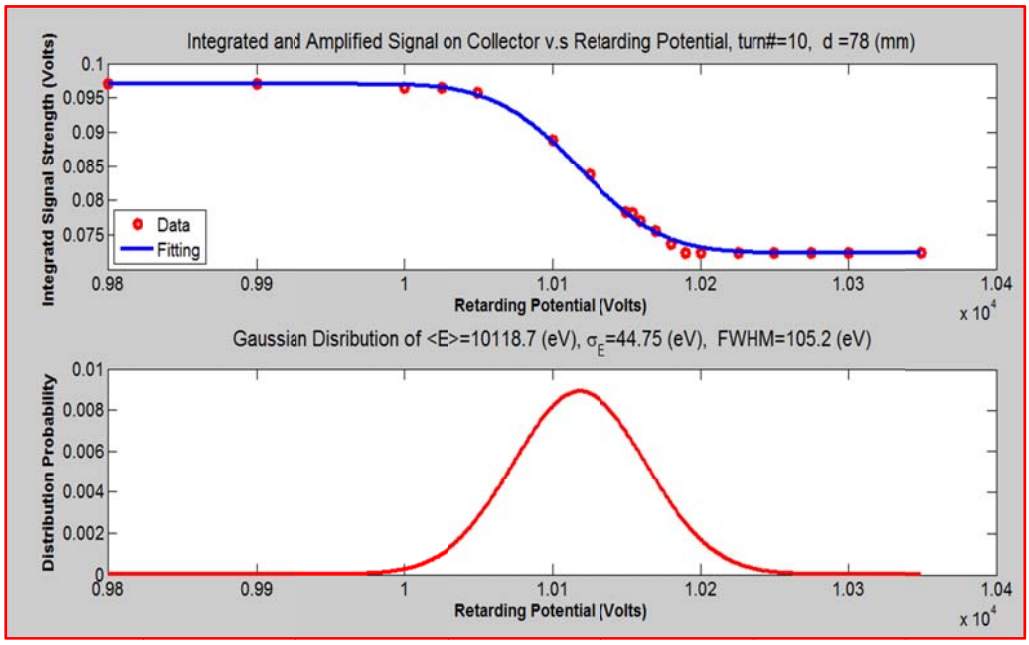

Figure 6.6: A sample of the energy spread analysis at turn 10. The upper graph shows the comparison between the original and reconstructed S-V curves. The lower graph displays the fitted Gaussian distribution of beam energy. The mean kinetic energy, RMS and FWHM energy spreads are 10118.7 eV, 44.75 eV and 105.2 eV, respectively.

Note that the conventional method of energy spread analysis usually involves differentiation of the *S*-*V* curve d*S*/d*V* and fitting it to a Gaussian function. While due to the discreteness originating from the smaller number of data points in the vicinity of the mean energy, the data points of d*S*/d*V* scatter around the Gaussian function with big deviation. This makes the fitting work difficult and inaccurate. That is why an integral of Gaussian function in Eq. (6.2) instead of the Gaussian function itself is chosen as the curve fitting function in our energy spread analysis.

Figure 6.6 demonstrates a sample of the energy spread analysis results for the SIR bunch measured at x= -6 mm (beam core edge) and turn 10. The mean kinetic energy, RMS and FWHM energy spreads are 10118.7 eV, 44.75 eV and 105.2 eV, respectively.

6.2.3 Measurement results and comparisons with simulation

A 600 mm, 8.0 μA, 10.3 keV, 30π mm mrad (same parameters as those in measurements) monoenergetic macroparticle bunch is also used in the simulation study by the code CYCO. The bunch has a uniform initial distribution in both the longitudinal line charge density and the 4D transverse phase space. In the analysis of simulation results, the beam region is cut into several 1-mm-wide thin vertical slices which are parallel to the design orbit, each thin slice has a fixed radial coordinate. The number of macroparticles, mean kinetic energy and RMS energy spread in each slice are calculated and compared with the experimental values.

Figure 6.7 shows the simulated and experimental radial slice beam densities. Figure 6.8 illustrates the simulated top views and slice RMS energy spread at turn 4 and turn 30, respectively. Figure 6.9 displays the simulated slice RMS energy spread up to turn 8.

Figure 6.10 depicts the comparison of slice RMS energy spread between simulations and experiments. Note that in this chapter, the slice energy spread and slice density denote all the slices are cut parallel to the longitudinal *z*-coordinate instead of the radial coordinate, which is conventionally used in free-electron lasers (FELs). The long bunch is a chaotic system, a small difference in the initial beam distribution may cause a huge beam profile deviation at large turn numbers. We can see that the simulated radial beam density profiles and slice RMS energy spread match the experimental values within an acceptable range.

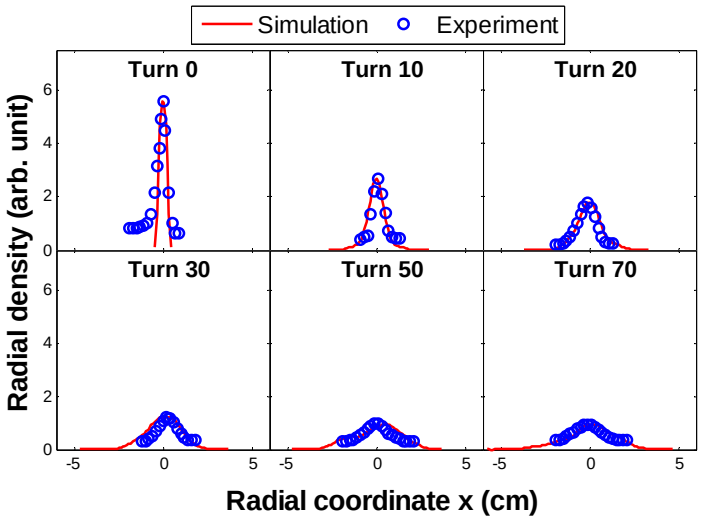

Figure 6.7: Evolutions of the radial beam density.

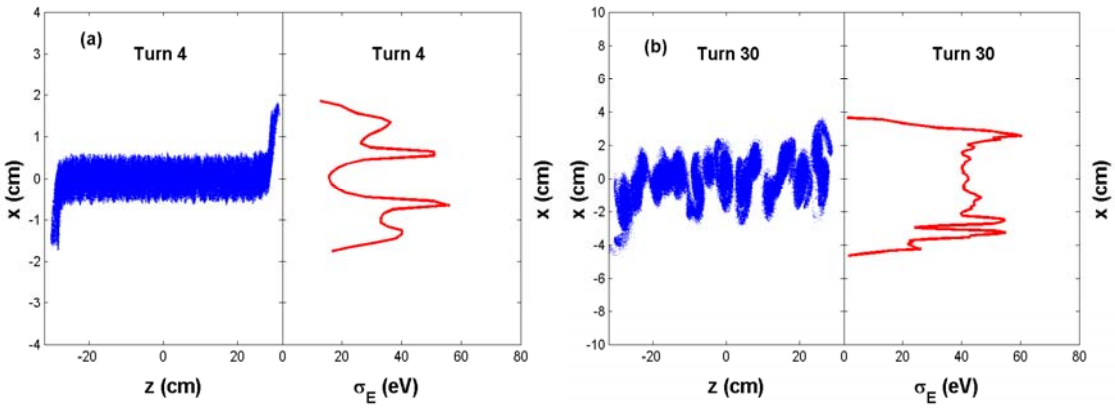

Figure 6.8: Simulated top views and slice RMS energy spread at (a) turn 4 (b) turn 30.

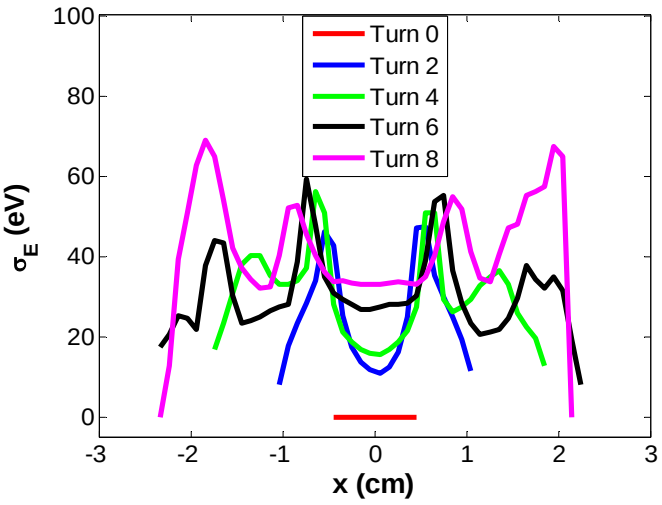

Figure 6.9: Simulated slice RMS energy spread at turns 0-8.

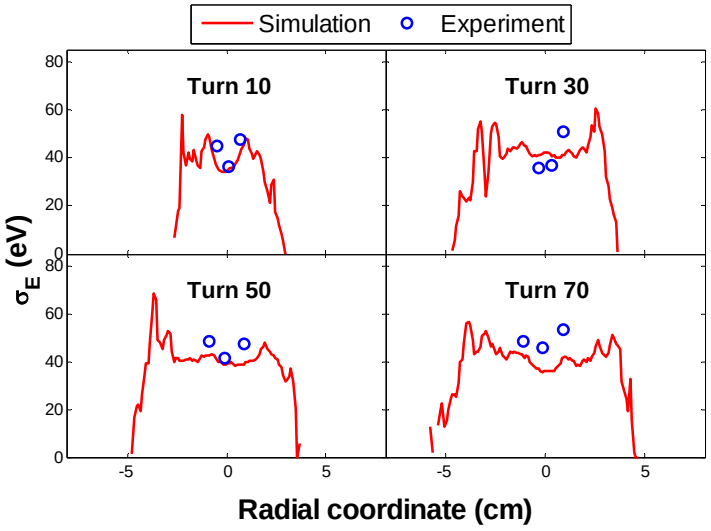

Figure 6.10: Comparisons of slice RMS energy spread between simulations and experiments.

Figures 6.8–6.10 show that the space charge fields induce the longitudinal density modulations and energy spread in an initially monoenergetic and straight coasting bunch in the isochronous ring. At smaller turn numbers, the energy spread in the beam head and tail is much greater than that of the beam core around the beam axis. As the turn number increases, the radial slice RMS energy spread distribution tends to become uniform and changes slowly. At the same time, the radial beam size increases, and the beam centroids deviate from the design orbit. The beam centroid wiggling may also cause the differences in the betatron oscillation phases between the beam clusters (slices). If the beam is long enough, the distribution of the radial centroid offsets of different clusters (slices) may be regarded as randomly uniform around the design orbit. The measured slice RMS energy spread at different radial coordinates is the density-weighted mean slice RMS energy spread of the beam core of any individual cluster (slice), which is independent of the radial coordinates. This can be explained below in Figure 6.11.

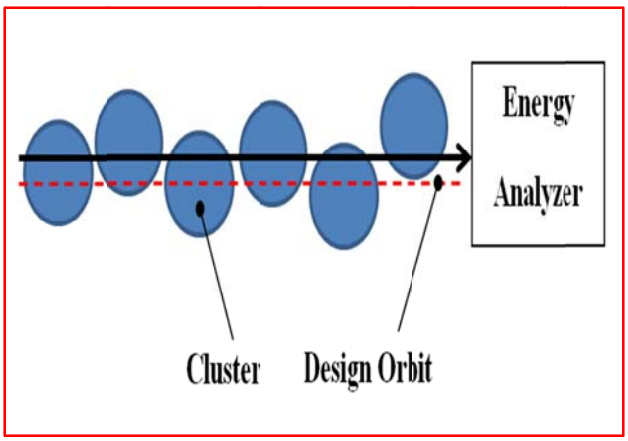

Figure 6.11 Sketch of clusters and energy analyzer.

Figure 6.11 shows at a given large turn number, the long bunch has broken up into many small clusters (the blue ovals) whose centroids distribute randomly and uniformly around the design orbit (the red dashed line). If we measure the slice RMS energy spread at a radial position as indicated by the solid black line with arrow, the analyzer will sample slices of different clusters. Assume there are N_c clusters in the whole bunch that are tagged by ID# 1, 2, 3,....N_c, and each cluster has the same number of particles and radial charge distribution profiles. Assume the slice sampled by the analyzer in each cluster contains n_i (i = 1, 2, 3,....N_c) charged particles and its RMS energy spread is σ_i, the mean kinetic energy of all slices at a fixed x is the same as $<E(x)>$ at large turn numbers, where x is the radial coordinate of the black solid line with respect to the red dashed line in Figure 6.11. Then the RMS energy spread in the i^{th} beam slice is:

$$\sigma_i = \sqrt{\frac{1}{n_i}\sum_{j=1}^{n_i}[E_j - < E(x) >]^2} \quad , \qquad i=1,\ 2,\ 3,\ \ldots\ldots\ N_c\ . \tag{6.3}$$

The sum of square of Eq. (6.3) gives:

$$\frac{n_1\sigma_1^{\ 2} + n_2\sigma_2^2 + \ldots\ldots n_{N_c}\sigma_{N_c}^2}{n_1 + n_2 + \ldots.. n_{N_c}} = < E_i^{\ 2} > - < E(x) >^2 = \sigma_E^2(x), \tag{6.4}$$

$$\sigma_E(x) = [\frac{n_1\sigma_1^{\ 2} + n_2\sigma_2^2 + ...n_{N_c}\sigma_{N_c}^2}{n_1 + n_2 + ...n_{N_c}}]^{\frac{1}{2}}. \tag{6.5}$$

If the number of clusters is large enough and the radial centroid offsets of all the clusters are randomly and uniformly distributed around the design orbit, the RHS of Eq. (6.5) is the density-weighted mean RMS energy spread of the sampled beam slices of different cluster cores at a fixed radial coordinate x. The $\sigma_E(x)$ of Eq. (6.5) is actually equal to the density-weighed mean slice RMS energy spread of any given single cluster core and is independent of the coordinate x. In real measurements, the above ideal preconditions are not satisfied completely; hence, there are always small energy spread fluctuations among different radial measurement points.

The equilibrium value of the kinetic energy deviation $\Delta E_{eq}(x)=E_{eq}(x)-E_{k0}$ and the radial coordinate x of an off-momentum particle satisfy the relation

$$\Delta E_{eq}(x) = \frac{2E_{k0}}{R}x, \tag{6.6}$$

where $E_{eq}(x)$ is the equilibrium kinetic energy and is equal to $<E(x)>$ of the beam slices centered at x at large turn numbers. For simplicity, it is assumed that the radial beam density distribution is uniform. Then the RMS energy spread of the equilibrium particles measured by the SIR energy analyzer with an entrance slit of width Γ = 1 mm centered at x can be estimated as:

$$\sigma_{\Delta E_{eq}} = [\frac{1}{\Gamma}\int_{x-\frac{\Gamma}{2}}^{x+\frac{\Gamma}{2}}[\frac{2E_{k0}}{R}(x'-x)]^2 dx']^{\frac{1}{2}} = \frac{E_{k0}\Gamma}{\sqrt{3}R} \approx 5.7eV. \tag{6.7}$$

This value is proportional to the slit width Γ and is independent of x. In addition, it is much less than the asymptotic energy spread which is about 50 eV at large turn numbers. This indicates that the number of particles at equilibrium energy only accounts for a small

fraction of the total particles in a beam slice.

The saturation of the slice RMS energy spread of clusters in the SIR beam is an indication of formation of the nonlinear advection of the beam in the $\vec{E} \times \vec{B}$ velocity field [10]. Assuming an ideal disk-shaped cluster coasts in an isochronous ring with an effective uniform magnetic field $\vec{B}_{eff}$, the $\vec{E}_{sc} \times \vec{B}_{eff}$ velocity field at any point on the median plane inside the cluster is along the azimuthal direction in the rest frame of the cluster. This will result in no particles staying at the beam head (tail) forever. Accordingly, the energy spread within a given beam slice of 1-mm width at any coordinate *x* will not build up with time significantly. During the binary cluster merging process, the total charge and size of the new clusters grow at the same time. Hence, the mean charge density of a single cluster does not change considerably, which may result in the saturation of the mean slice RMS energy spread averaged over the radial coordinate.

6.3 Corotation of cluster pair in the $\vec{E} \times \vec{B}$ field

In the simulated long-term evolution of the space-charge dominated SIR beam, first, the bunch may break up into many small clusters along *z*-coordinate. Later, the neighboring cluster pairs orbit each other in their center of mass frame, which is the so-called corotation. Finally, the cluster pairs merge together after some turns of corotation. This section is devoted to study the mechanism of corotation of cluster pair, which is a characteristic phenomenon of the long-term evolution of beam profiles in the isochronous regime.

Figure 6.12 illustrates the top views of the relative position of a pair of macroparticles coasting in the SIR at turns 0, 5, 11, 22, 34, and 46 simulated by code CYCO. The red

and blue dots stand for the macroparticle pair, each of which has the same charge Q=8.0 $\times 10^{-14}$ Coulomb and kinetic energy E_0=10.3 keV. At turn 0, they are separated by an initial distance d_0=1.5 cm and both are moving along the design orbit. The red macroparticle is the leading one. Figure 6.12 indicates that the macroparticle pair performs corotation with a period of about 46 turns. This phenomenon can be explained and predicted by Cerfon's theory of the motion in the $\vec{E} \times \vec{B}$ field [10].

Assuming two identical macroparticles with the same charge Q and mass m coast in the SIR with mean radius R, their trajectories are complicated cycloid-like curves and not closed. In addition, the distance $d(t)$ between them changes with time. By smooth approximation, i.e., the magnetic field is regarded as uniform along the ring with an

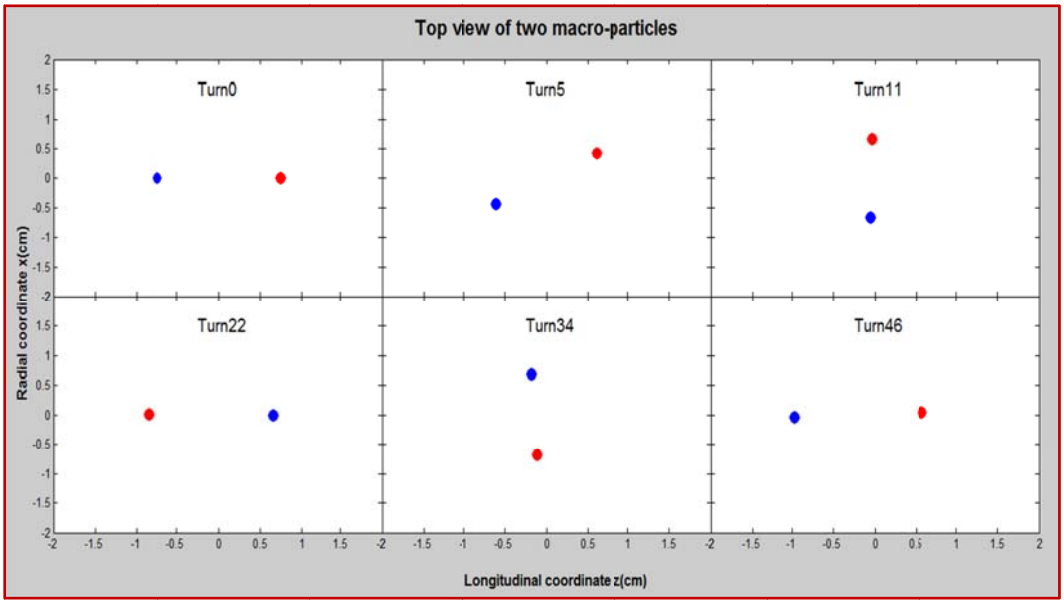

Figure 6.12: Corotation of two macroparticles with Q=8×10^{-14} Coulomb, E_0 = 10.3 keV, and d_0=1.5 cm.

effective strength B_{eff}, and average distance $<d(t)>=(d_{max}+d_{min})/2$ in one period of corotation (it is valid if d_{max}/d_{min} does not deviate too much from 1), then the amplitudes

of $\vec{\boldsymbol{B}}_{eff}$ and space charge field $\vec{\boldsymbol{E}}_{sc}$ can be estimated as

$$B_{eff} = \frac{mv_0}{eR}, \qquad E_{sc} = \frac{Q}{4\pi\varepsilon_0 < d(t) >^2}, \tag{6.8}$$

where e, and v_0 stand for the charge and velocity of each macroparticle, respectively.

Since $\vec{\boldsymbol{B}}_{eff}$ and $\vec{\boldsymbol{E}}_{sc}$ are perpendicular to each other, each macroparticle has a drift velocity

$$V_{drift} = \mid \vec{V}_{drift} \mid = \mid \frac{\vec{E}_{sc} \times \vec{B}_{eff}}{B_{eff}^2} \mid = \frac{E_{sc}}{B_{eff}} = \frac{Q}{4\pi\varepsilon_0 B_{eff} < d(t) >^2}. \tag{6.9}$$

The mean corotation frequency is

$$\omega_{corot.} = \frac{V_{drift}}{\frac{< d >}{2}} = \frac{Q}{2\pi\varepsilon_0 B_{eff} < d >^3}. \tag{6.10}$$

The left graph of Figure 6.13 shows the simulated distance $d(t)$ between the macroparticle pair in the first period of corotation. The right graph displays the simulated corotation angle of a line connecting the macroparticle pair with respect to +z-coordinate; the corotation frequency is fitted and compares with the theoretical estimation predicted by Eq. (6.10). We can see the simulation and theory match well.

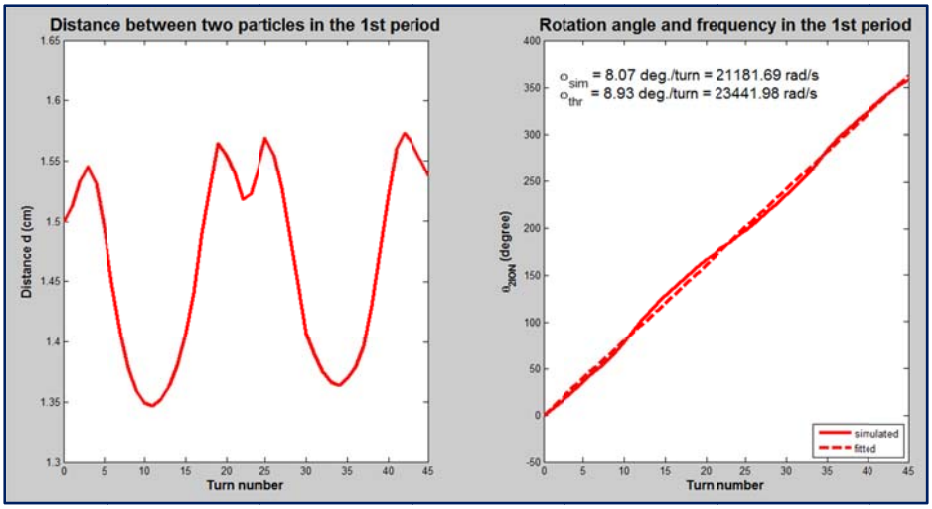

Figure 6.13: Simulated distance between the two particles (left) and their corotation angle with respect to the +z-coordinate (right) in the first corotation period. The simulated corotation frequency ω_{sim} can be fitted from the angle-turn number curve. The theoretical corotation frequency ω_{thr} predicted by Eq. (6.10) is also plotted for comparison.

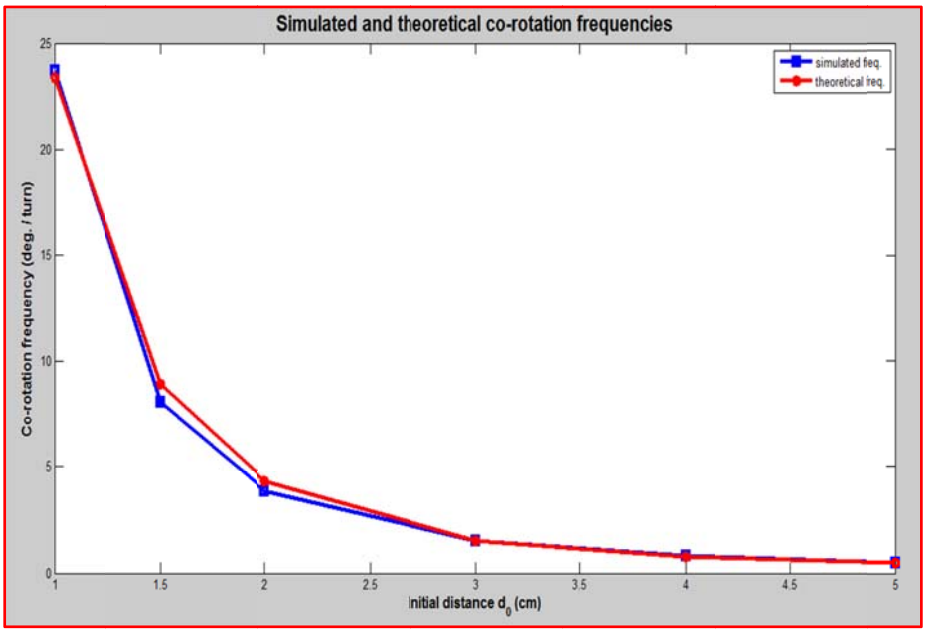

Figure 6.14: Simulated corotation frequencies of two macroparticles with different initial distance d_0.

Figure 6.14 displays the good agreement between the simulated and theoretical corotation frequencies of macroparticle pair with different initial distance d_0.

Next, at turn 0, the two macroparticles are replaced by two monoenergetic macroparticle bunches of 10.3 keV kinetic energy separated by d_0 =1.5 cm. Each bunch is 10 ns long in time scale (about 1 cm) and has a charge of 8×10^{-14} Coulomb. The evolution of their beam profiles in the first 15 turns is shown in Figure 6.15. The left graph of Figure 6.16 shows the simulated distance $d(t)$ between the centroids of the two short bunches in the first 1/4 period of corotation; the right graph displays the simulated corotation frequency and comparison with the theoretical estimation predicted by Eq. (6.10). We can see the simulation and theory match roughly. Unlike the dimensionless macroparticles, the short bunches have finite dimension with a certain beam distribution. They have some new properties which a single macroparticle does not have, for example, angular momentum of self-spin. When the distance between the bunch centroids is less than or comparable to the bunch length, the interaction between the bunches is highly nonlinear, which results in filamentation and cluster merging.

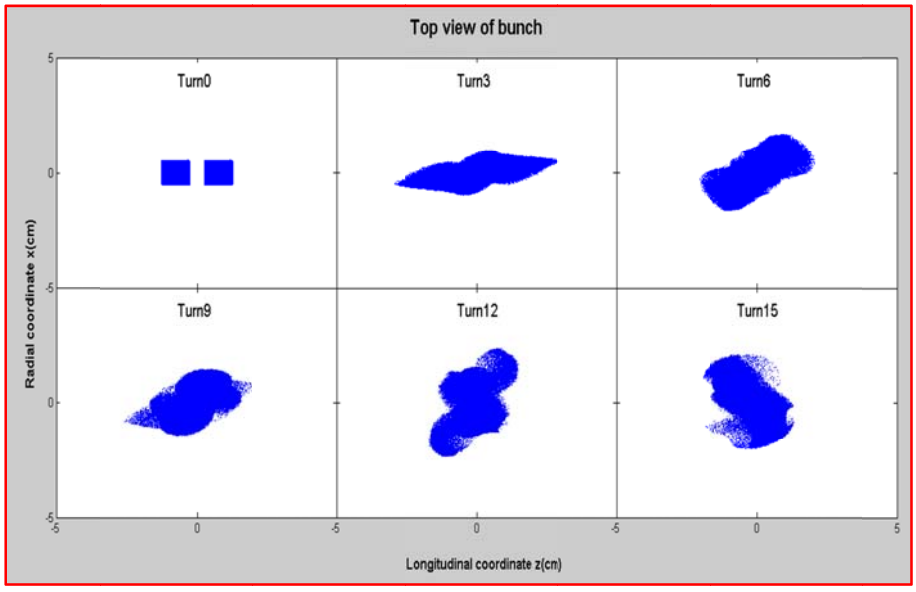

Figure 6.15: Corotation of two short bunches with τ_b=10 ns, I_0=8.0 uA, Q=8×10^{-14} Coulomb, d_0=1.5 cm, and E_0 = 10.3 keV.

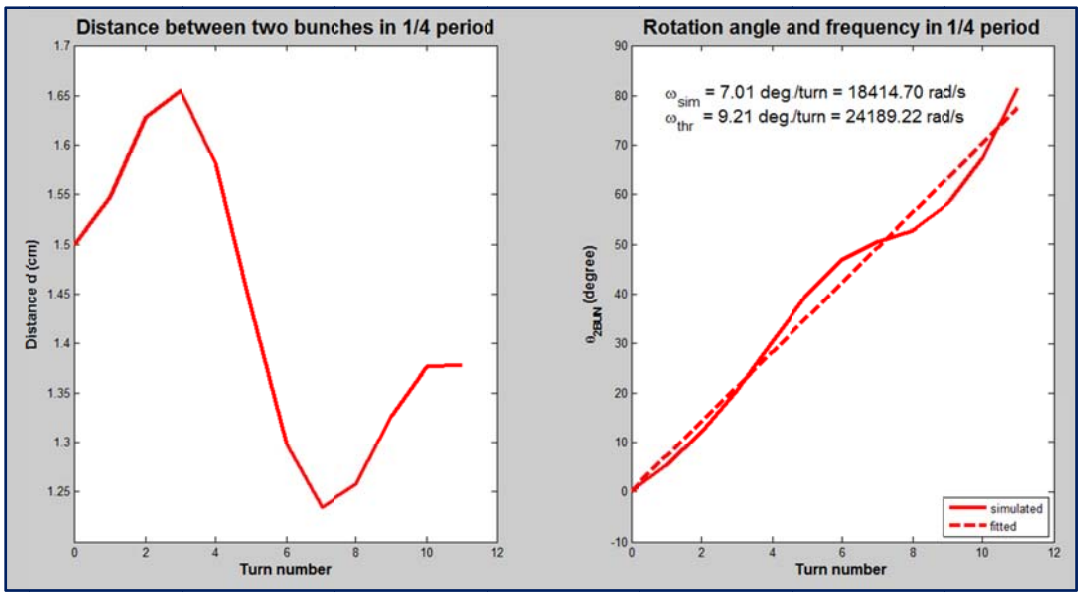

Figure 6.16: Simulated distance between the centroids of two short bunches (left) and their angle with respect to the *z*-coordinate (right) in the first 1/4 corotation period. The simulated corotation frequency ω_{sim} and the theoretical value ω_{thr} predicted by Eq. (6.10) are also provided in the right graph.

In summary, the good agreement between the simulation and theory in Figures 6.13, 6.14 and 6.16 provides a numerical verification for Cerfon's theory of drift motion in the $\vec{\boldsymbol{E}} \times \vec{\boldsymbol{B}}$ field.

6.4 Binary merging of 2D short bunches

This section focuses on the simulation study of the binary cluster merging in the isochronous ring. Two 2D short sheet bunches lying on the median ring plane are created and employed in the simulation study. Compared with the conventional 3D bunch pair, the binary merging process of 2D bunch pair is easier to be observed and understood, because the macroparticles do not have vertical distribution and motion. Figure 6.17 shows the top view (projection in the *z*-*x* plane) and side view (projection in *z*-*y* plane) of the 2D bunch pair. The beam parameters of each 2D bunch are τ_b=10 ns (about 1 cm),

I_0=8.0 uA, Q=8×10^{-14} Coulomb, and E_0=10.3 keV. Each bunch has uniform distribution in both the x-z plane and the x-x' phase space. At turn 0, the two bunches coast along the +z-coordinate with an initial separation of d_0=1.5 cm.

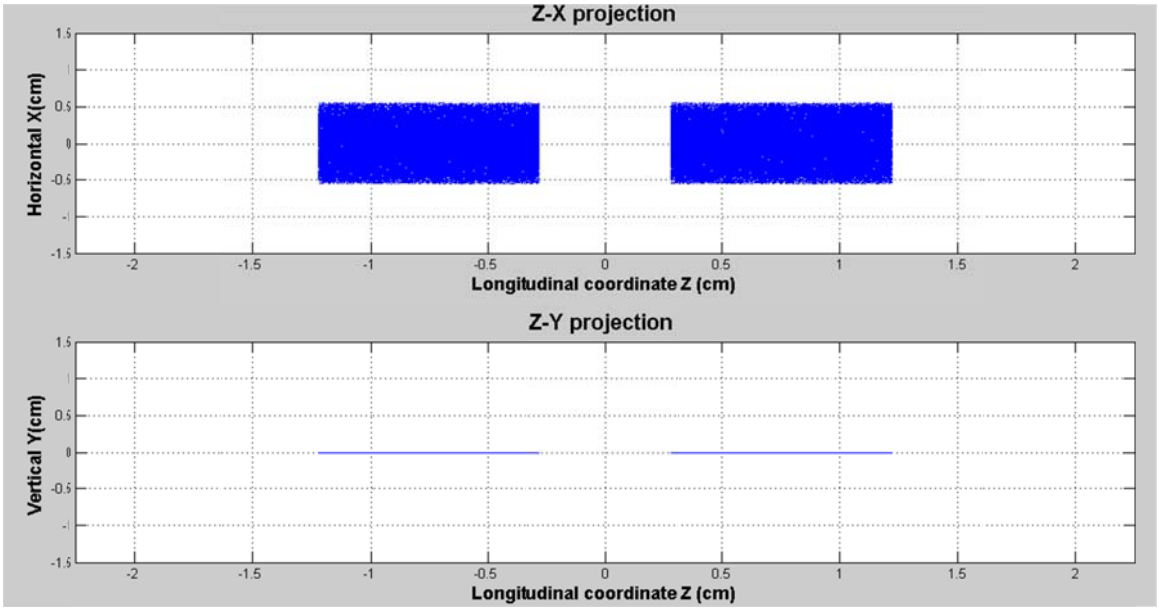

Figure 6.17: Initial distribution of 2D bunch pair with τ_b=10 ns, I_0=8.0 uA, Q=8×10^{-14} Coulomb, E_0=10.3 keV and d_0=1.5 cm. The upper graph shows the top view of the beam profile in z-x plane; the lower graph shows the side view of the beam in z-y plane.

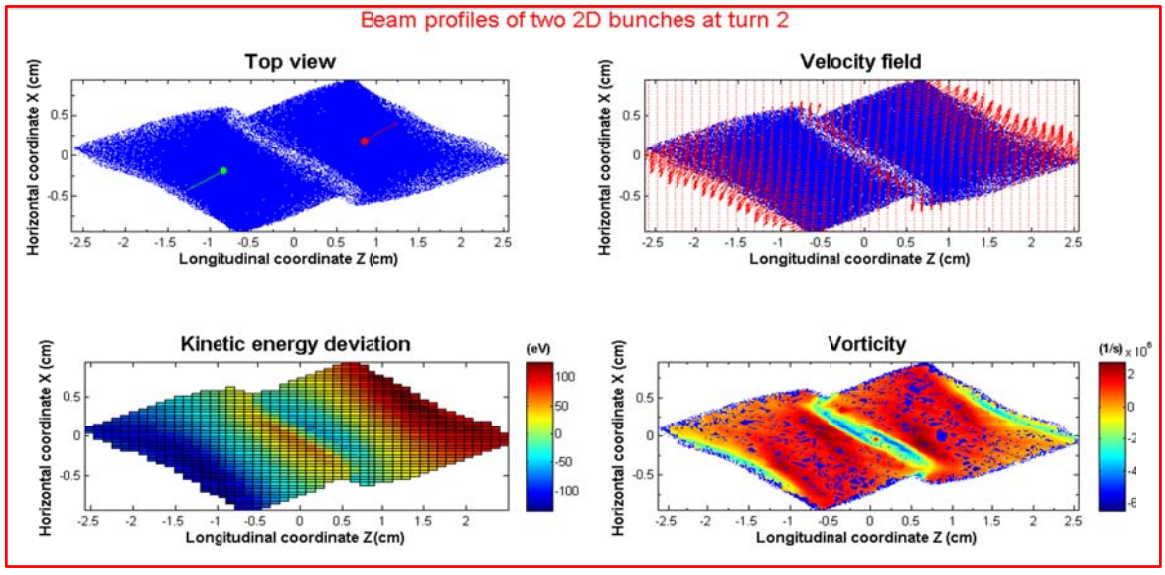

Figure 6.18: Beam profiles of 2D bunch pair in the center of mass frame at turn 2.

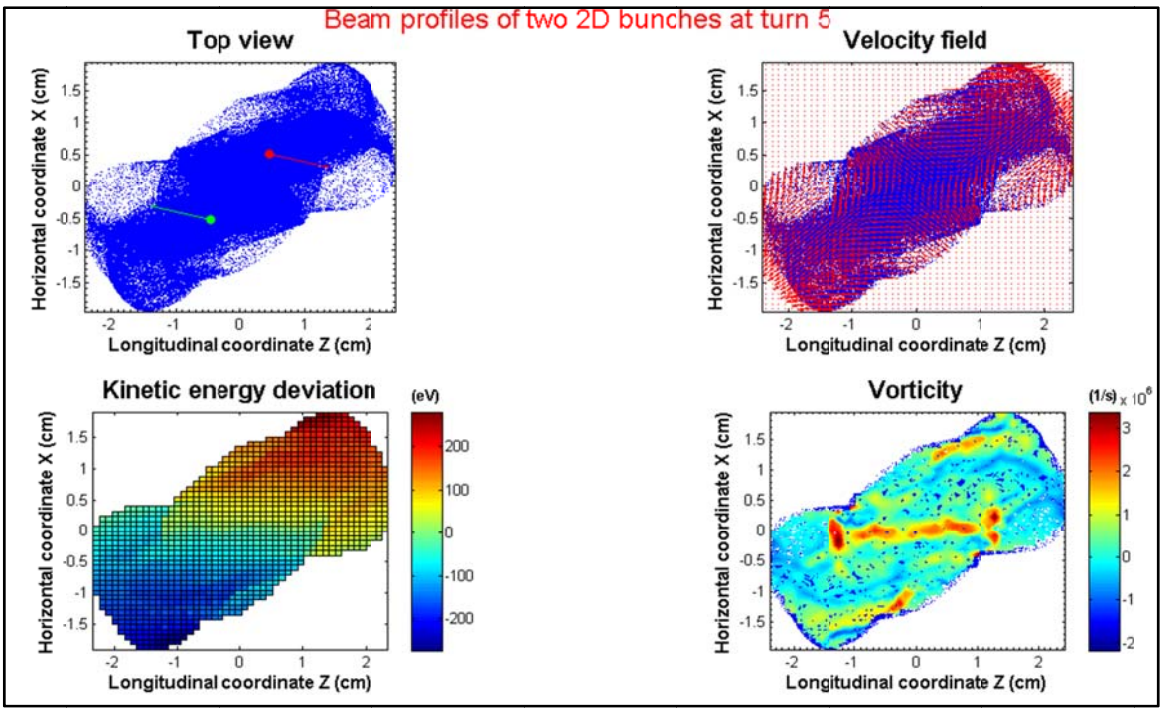

Figure 6.19: Beam profiles of 2D bunch pair in the center of mass frame at turn 5.

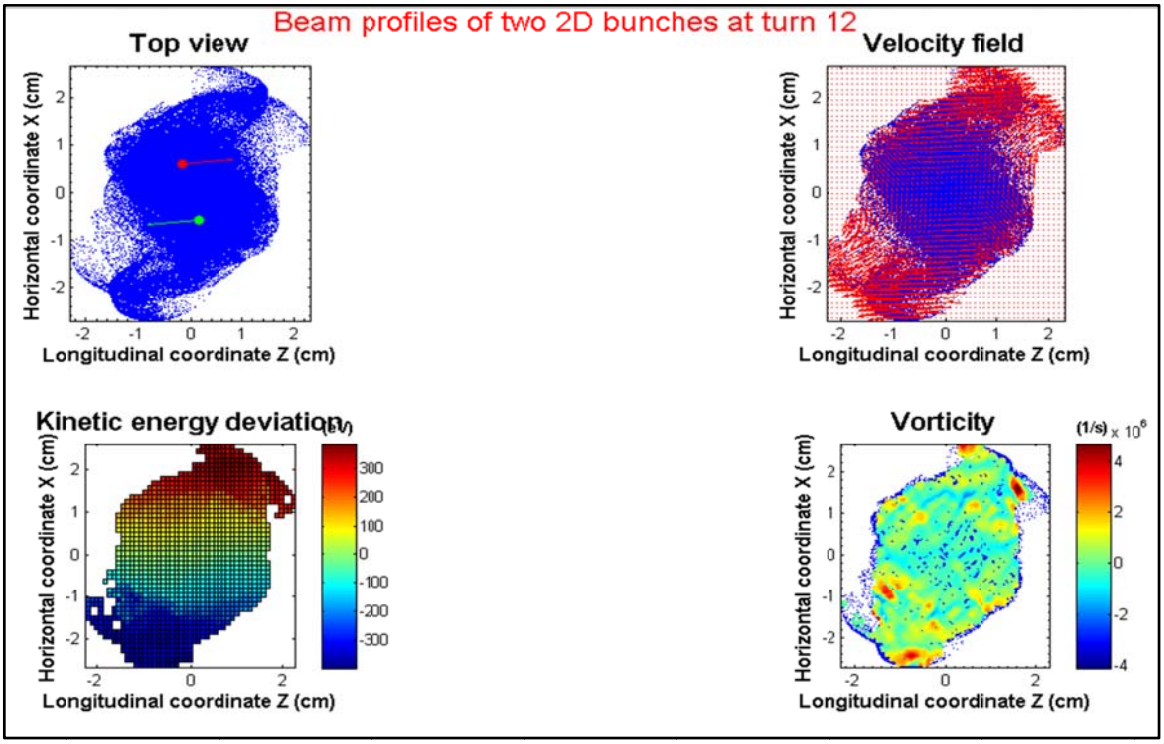

Figure 6.20: Beam profiles of 2D bunch pair in the center of mass frame at turn 12.

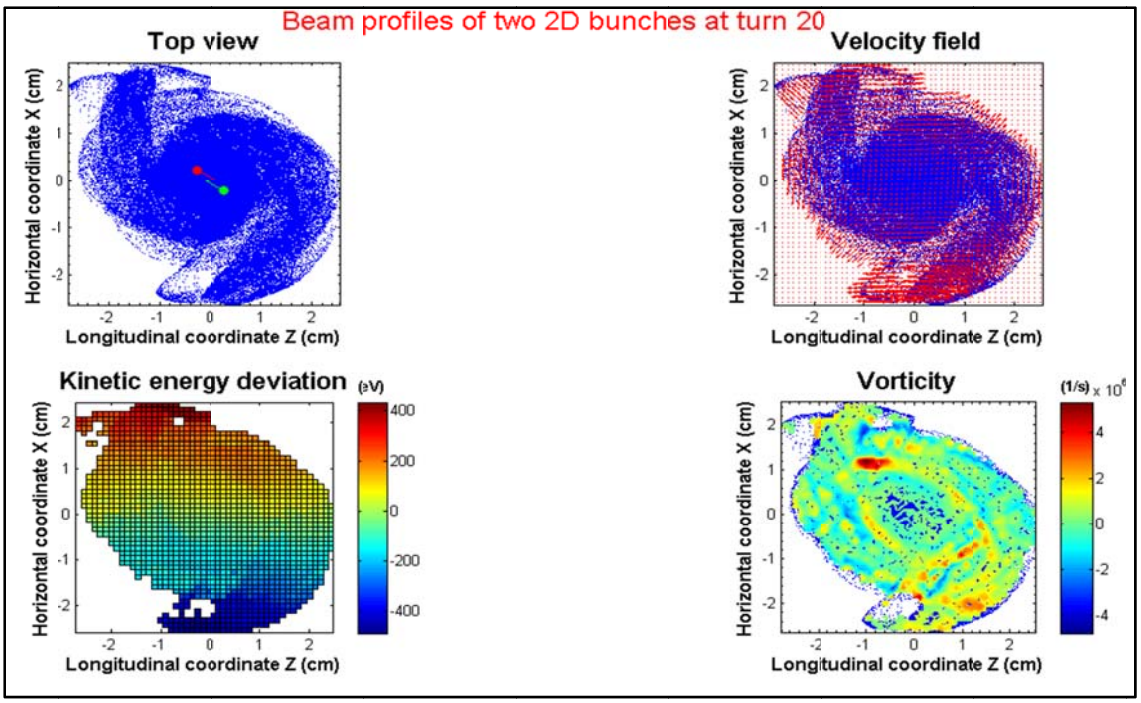

Figure 6.21: Beam profiles of 2D bunch pair in the center of mass frame at turn 20.

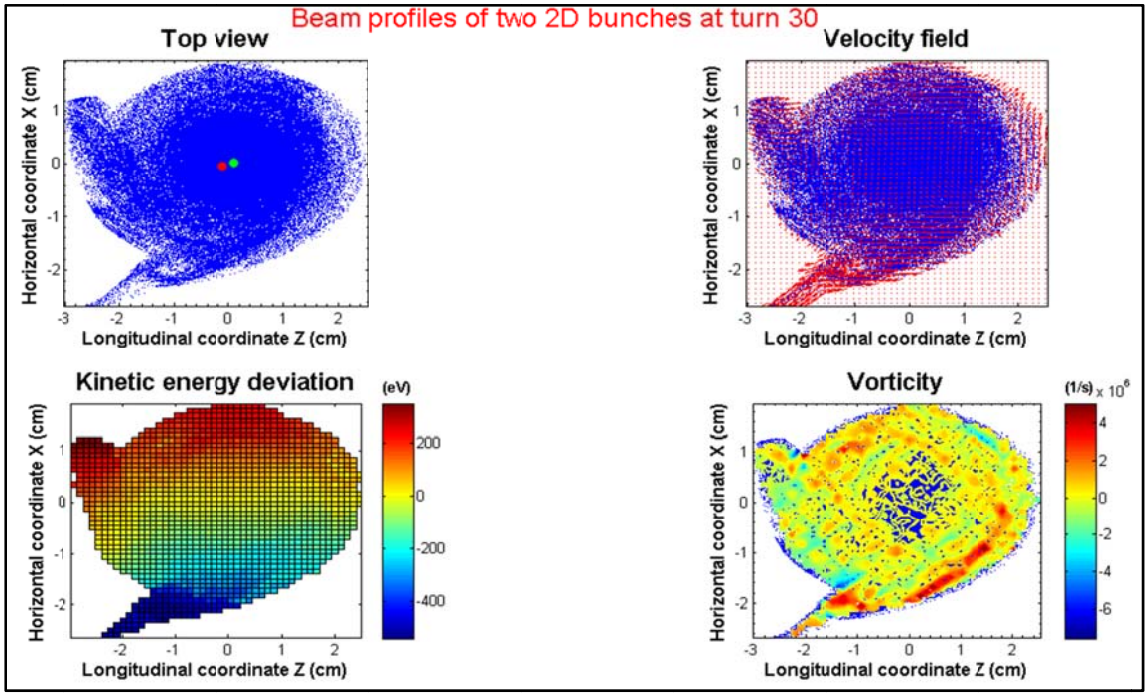

Figure 6.22: Beam profiles of the 2D bunch pair in the center of mass frame at turn 30.

Figures 6.18-6.22 illustrate the evolution of the beam density, energy deviation distribution, velocity field and vorticity of the two short 2D bunches at turns 2, 5, 12, 20 and 30. Each figure consists of four graphs: the upper left graph shows the top view of the beam density distribution on the median ring plane, the red and blue dots with arrows stand for the centroids of the bunches and their velocity vectors in the center of mass frame; the upper right graph displays the velocity field in the center of mass frame; the lower left graph demonstrates the distribution of energy deviation of the 2D bunches; the lower right graph depicts the distribution of vorticity, which is defined as the curl of the speed vector $\vec{u}$ in the center of mass frame:

$$\vec{\Omega}(\vec{x},t) = \nabla \times \vec{u}. \tag{6.13}$$

During the merging process, the two bunches are highly deformed and two filament tails appear. The two beam cores approach, overlap and collide; at first, the two centroids corotate in the counter clockwise direction just like two macroparticles. But the repulsive Coulomb force between two bunches causes dynamical friction, which decreases the kinetic energy of the two centroids. The relative motion between the two centroids is suppressed. This is completely different from the two macroparticle model in which each macroparticle is dimensionless; the dynamic friction between the two macroparticle is negligible, and the corotation motion can last forever. We can also use the theory of drift motion in $\vec{\boldsymbol{E}} \times \vec{\boldsymbol{B}}$ field to explain the merging process. When the two bunch cores overlap partly, the space charge force on the overlapping parts is cancelled significantly. In consequence, the drift motion in the $\vec{\boldsymbol{E}} \times \vec{\boldsymbol{B}}$ field will be suppressed considerably. The overlapping parts of the two bunches will become the cradle of a new beam core.

6.5 Conclusions

The measured slice RMS energy spread and radial density profiles of a long coasting bunch agree with the simulation results. At large turn numbers, the randomly distributed cluster centroid offsets tend to make the radial energy spread distribution of the whole bunch uniform. The measured energy spread is the density-weighted mean slice RMS energy spread of any single cluster core. Its saturation behavior indicates the formation of the nonlinear advection of the particles due to the $\vec{E} \times \vec{B}$ velocity field in each cluster.

The simulation study of corotation of cluster pair by macroparticle pair model and short bunch pair model verifies the theory of drift motion in the $\vec{E} \times \vec{B}$ field. The corotation and merging of cluster pair in the long-term evolution of beam profiles is a natural consequence of the drift motion of clusters in the $\vec{E} \times \vec{B}$ field.

Chapter 7

CONCLUSIONS AND FUTURE WORKS

7.1 Conclusions

This dissertation focuses on the mechanism and evolution of microwave instability of coasting beams with space charge in the isochronous regime.

Several theoretical LSC impedance models with different cross-sections of the beam and chamber are studied. The derived LSC impedances are in good agreement with the numerical simulations. They can be used in instability analysis induced by the LSC field at any perturbation wavelength λ. In particular, for λ<5cm, the LSC impedance of SIR beam can be approximated by that of a round beam in free space.

For a beam with finite energy spread, due to the non-zero transfer matrix element $R_{56}(s)$, the particles with the same radial coordinates (x, x') in the radial phase space but with deferent energies may have different path length difference Δz; In addition, due to the betatron oscillation and radial-longitudinal coupling effect, the particles with the same energy deviation but with different radial coordinates (x, x') in the radial phase space also have different path length difference Δz via the transfer matrix elements R_{51}(s) and R_{52}(s). These path length differences are the important source of Landau damping for coasting beam with finite emittance and energy spread in the isochronous ring. The path length deviation contributed from the betatron motion in the isochronous rings is also an important effect that should be considered to realize the coherent terahertz synchrotron radiation (CSR) [56], in which case the length of an extremely short electron bunch needs

to be preserved precisely. A 2D dispersion relation taking into account the Landau damping effects originating from the energy spread and emittance is derived in Chapter 4. Compared with the conventional 1D growth rate formula, the 2D dispersion relation provides a more accurate approach to predict the instability growth rates, especially in the short wavelength limits.

A compact retarding field energy analyzer (RFA) with large entrance slit was designed, tested and employed in the energy spread measurement. The performance of the RFA meets our requirement for the experimental study of microwave instability.

The energy spread measurement results of a coasting SIR beam match the simulation results in the long term evolution of microwave instability. The measured and simulated saturation of the radial distribution of energy spread at large turn number is caused by the formation of vortex motion in the bunches' rest frames. The study using the two-macroparticle model and the two-bunch model also validate the theory of vortex motion in the $\vec{E} \times \vec{B}$ field.

7.2 Future works

Some new research study may be performed in the future, such as:

- In Chapter 4, there exist bigger discrepancies between the theoretical and simulated instability growth rates for λ<1 cm. Further research study is needed to explain the reason for the discrepancies.
- In recent years, a 3D PIC object-oriented parallel simulation code OPAL-CYCL has been successfully developed by PSI [17]. Being a parallel code, it can simulate beam dynamics in high intensity cyclotrons including neighboring

bunch effects. Some interesting results have been obtained by the PSI researchers [18, 57]. In comparison, CYCO is incapable of parallel computation at present. If possible, CYCO can be modified to be compatible with parallel computation in the future. This may greatly enhance its efficiency and functionality.

- After years of successful operation with fruitful results, the Small Isochronous Ring (SIR) was dismantled in 2010. If possible, it may be reassembled and upgraded in the future (e.g., introduction of RF cavity, flat-top cavity, and new energy spread measurement system, etc.). After upgrade, more research studies regarding the space charger effects in isochronous regime can be carried out.

APPENDICES

APPENDIX A

FORMALISM OF THE STANDARD TRANSFER MATRIX FOR SIR

This note presents the linear beam optics of SIR lattice (hard-edge model) using the *standard* transfer matrix formalism.

A.1 Brief review of the standard transfer matrix

The coordinates of a particle in the 6D phase space can be described by a 6-element vector $(x(s),\ x'(s),\ y(s),\ y'(s),\ z(s),\ \delta(s))^{T}$ [58-60], where x, y and z are the radial (horizontal), vertical and longitudinal coordinates with respect to a hypothetical on-momentum particle traveling along the design orbit; $x'(s)=dx/ds$ and $y'(s)=dy/ds$ are the radial (horizontal) and vertical slopes of velocity; $\delta=\Delta p/p$ is the fractional momentum deviation compared with the on-momentum particle, the superscript 'T' stands for the transpose of vector or matrix. If there is no electric field and x-y coupling, the standard transfer matrix $M(s)$ mapping the initial coordinates of a particle $(x(0),\ x'(0),\ y(0),\ y'(0),\ z(0),\ \delta(0))^{T}$ in the 6D phase space at $s=0$ to the current ones $(x(s),\ x'(s),\ y(s),\ y'(s),\ z(s),\ \delta(s))^{T}$ at s is [58-60]

$$M(s)=\begin{bmatrix} \frac{\partial x}{\partial x(0)} & \frac{\partial x}{\partial x'(0)} & \frac{\partial x}{\partial y(0)} & \frac{\partial x}{\partial y'(0)} & \frac{\partial x}{\partial z(0)} & \frac{\partial x}{\partial \delta(0)} \\ \frac{\partial x'}{\partial x(0)} & \frac{\partial x'}{\partial x'(0)} & \frac{\partial x'}{\partial y(0)} & \frac{\partial x'}{\partial y'(0)} & \frac{\partial x'}{\partial z(0)} & \frac{\partial x'}{\partial \delta(0)} \\ \frac{\partial y}{\partial x(0)} & \frac{\partial y}{\partial x'(0)} & \frac{\partial y}{\partial y(0)} & \frac{\partial y}{\partial y'(0)} & \frac{\partial y}{\partial z(0)} & \frac{\partial y}{\partial \delta(0)} \\ \frac{\partial y'}{\partial x(0)} & \frac{\partial y'}{\partial' x(0)} & \frac{\partial y'}{\partial y(0)} & \frac{\partial y'}{y'(0)} & \frac{\partial y'}{\partial z(0)} & \frac{\partial y'}{\partial \delta(0)} \\ \frac{\partial z}{\partial x(0)} & \frac{\partial z}{\partial x'(0)} & \frac{\partial z}{\partial y(0)} & \frac{\partial z}{\partial y'(0)} & \frac{\partial z}{\partial z(0)} & \frac{\partial z}{\partial \delta(0)} \\ \frac{\partial \delta}{\partial x(0)} & \frac{\partial \delta}{\partial x'(0)} & \frac{\partial \delta}{\partial y(0)} & \frac{\partial \delta}{\partial y'(0)} & \frac{\partial \delta}{\partial z(0)} & \frac{\partial \delta}{\partial \delta(0)} \end{bmatrix}=\begin{bmatrix} M_{11} & M_{12} & 0 & 0 & 0 & M_{16} \\ M_{21} & M_{22} & 0 & 0 & 0 & M_{26} \\ 0 & 0 & M_{33} & M_{34} & 0 & 0 \\ 0 & 0 & M_{43} & M_{44} & 0 & 0 \\ M_{51} & M_{52} & 0 & 0 & 1 & M_{56} \\ 0 & 0 & 0 & 0 & 0 & 1 \end{bmatrix}. \quad \text{(A.1)}$$

The matrix $M(s)$ satisfies the symplectic condition $M^{\mathrm{T}}SM=S$, where S is a 6×6 antisymmetric matrix

$$S=\begin{bmatrix} 0 & 1 & 0 & 0 & 0 & 0 \\ -1 & 0 & 0 & 0 & 0 & 0 \\ 0 & 0 & 0 & 1 & 0 & 0 \\ 0 & 0 & -1 & 0 & 0 & 0 \\ 0 & 0 & 0 & 0 & 0 & 1 \\ 0 & 0 & 0 & 0 & -1 & 0 \end{bmatrix}, \quad \text{(A.2)}$$

The determinant of matrix $M(s)$ is unity, e.g., $\det(M)=1$, which is required by Liouville's theorem. Some elements of the standard matrix $M(s)$ satisfy the following relations [8, 60, 61]:

$$M_{16}(s)=M_{12}(s)\int_0^s \frac{M_{11}(s')}{\rho(s')}ds'-M_{11}(s)\int_0^s \frac{M_{12}(s')}{\rho(s')}ds', \quad \text{(A.3)}$$

$$M_{26}(s)=M_{22}(s)\int_0^s \frac{M_{11}(s')}{\rho(s')}ds'-M_{21}(s)\int_0^s \frac{M_{12}(s')}{\rho(s')}ds', \quad \text{(A.4)}$$

$$M_{51}=M_{16}M_{21}-M_{26}M_{11}, \quad \text{(A.5)}$$

$$M_{52}=M_{16}M_{22}-M_{26}M_{12}, \quad \text{(A.6)}$$

where $\rho(s)$ is the local radius of curvature of the orbit.

A.2 Standard transfer matrices for elements of SIR

The four-fold symmetric SIR lattice mainly consists of four 90^{o} bending magnets with edge focusing connected by four drifts in between. By thin lens approximation, the bending magnets with tilted pole faces can be treated as a sector magnet (without pole face rotation) to which magnetic wedges with edge focusing are attached [8]. According to the theory of liner beam optics, the transfer matrices $M(s)$ are [58]:

(a) Drift

$$M_{Drift} = \begin{bmatrix} 1 & l & 0 & 0 & 0 & 0 \\ 0 & 1 & 0 & 0 & 0 & 0 \\ 0 & 0 & 1 & l & 0 & 0 \\ 0 & 0 & 0 & 1 & 0 & 0 \\ 0 & 0 & 0 & 0 & 1 & \frac{l}{\gamma^2} \\ 0 & 0 & 0 & 0 & 0 & 1 \end{bmatrix}, \tag{A.7}$$

with l being the length of the drift.

(b) Sector bending magnet

$$M_{SBend} = \begin{bmatrix} \cos(\theta) & \rho_0 \sin(\theta) & 0 & 0 & 0 & \rho_0[1-\cos(\theta)] \\ -\frac{1}{\rho_0}\sin(\theta) & \cos(\theta) & 0 & 0 & 0 & \sin(\theta) \\ 0 & 0 & 1 & \rho_0\theta & 0 & 0 \\ 0 & 0 & 0 & 1 & 0 & 0 \\ -\sin(\theta) & -\rho_0[1-\cos(\theta)] & 0 & 0 & 1 & \frac{\rho_0\theta}{\gamma^2} - \rho_0\theta + \rho_0\sin(\theta) \\ 0 & 0 & 0 & 0 & 0 & 1 \end{bmatrix}, \tag{A.8}$$

where ρ_0 and θ are the bending radius and angle of the sector bending magnet, respectively.

(c) Magnetic wedge with edge focusing

$$M_{Edge}=\begin{bmatrix} 1 & 0 & 0 & 0 & 0 & 0 \\ \dfrac{\tan(\varphi)}{\rho_0} & 1 & 0 & 0 & 0 & 0 \\ 0 & 0 & 1 & 0 & 0 & 0 \\ 0 & 0 & -\dfrac{\tan(\varphi)}{\rho_0} & 1 & 0 & 0 \\ 0 & 0 & 0 & 0 & 1 & 0 \\ 0 & 0 & 0 & 0 & 0 & 1 \end{bmatrix}, \tag{A.9}$$

with φ being the pole face rotation angle.

A.3 Optic functions of SIR (hard-edge model)

Let us consider the general condition of isochronism of a *relativistic* particle traveling along an *N*-fold symmetric isochronous ring with edge focusing (See Figure A.1). The transfer matrix of 1/2*N* period (half-cell) of the ring lattice is

$$M_{\frac{1}{2}Cell} = M_{SBend} \bullet M_{Edge} \bullet M_{Dfift}. \tag{A.10}$$

Substituting Eqs. (A.7), (A.8) and (A.9) into Eq. (A.10) with $\theta=\pi/N$ yields

$$M_{\frac{1}{2}cell}=\begin{bmatrix} M_{11} & M_{12} & 0 & 0 & 0 & M_{16} \\ M_{21} & M_{22} & 0 & 0 & 0 & M_{26} \\ 0 & 0 & M_{33} & M_{34} & 0 & 0 \\ 0 & 0 & M_{43} & M_{44} & 0 & 0 \\ M_{51} & M_{52} & 0 & 0 & 1 & M_{56} \\ 0 & 0 & 0 & 0 & 0 & 1 \end{bmatrix}, \tag{A.11}$$

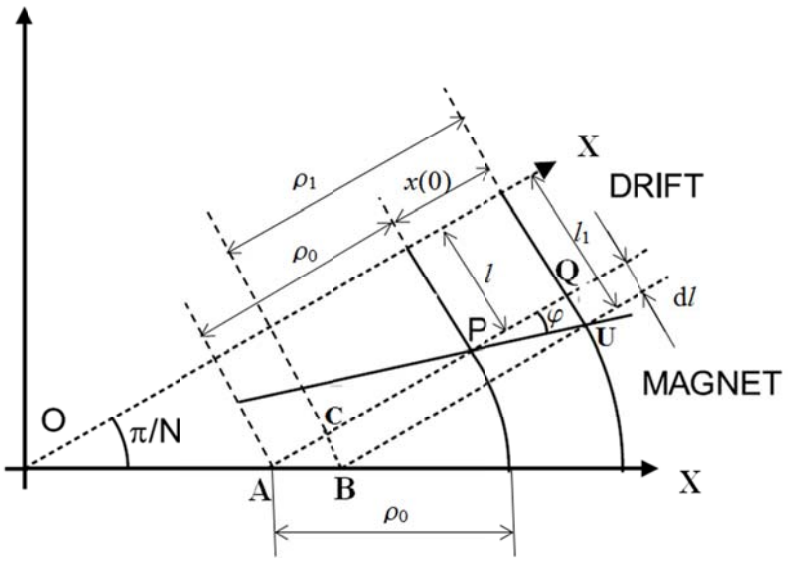

Figure A.1: Schematic of a half cell of an *N*-fold symmetric isochronous ring. The ring center is located at point *O*. ρ_0 and ρ_1 are the bending radii of the on-momentum and off-momentum particles with their centers of gyration located at points *A* and *B*, respectively. The solid line passing points *P* and *U* depicts the titled pole face of the magnet. l and l_1 are the half drift lengths traveled by the on-momentum and off-momentum particles, respectively.

where

$$M_{11} = \cos(\frac{\pi}{N}) + \tan(\varphi)\sin(\frac{\pi}{N}), \tag{A.12}$$

$$M_{12} = \rho_0 \sin(\frac{\pi}{N}) + l[\cos(\frac{\pi}{N}) + \tan(\varphi)\sin(\frac{\pi}{N})], \tag{A.13}$$

$$M_{16} = \rho_0[1 - \cos(\frac{\pi}{N})], \tag{A.14}$$

$$M_{21} = -\frac{1}{\rho_0}[\sin(\frac{\pi}{N}) - \tan(\varphi)\cos(\frac{\pi}{N})], \tag{A.15}$$

$$M_{22} = \cos(\frac{\pi}{N}) - \frac{l}{\rho_0}[\sin(\frac{\pi}{N}) - \tan(\varphi)\cos(\frac{\pi}{N})], \tag{A.16}$$

$$M_{26} = \sin(\frac{\pi}{N}), \tag{A.17}$$

$$M_{33} = 1 - \frac{\pi}{N}\tan(\varphi), \tag{A.18}$$

$$M_{34} = \frac{\pi}{N}\rho_0 + l[1 - \frac{\pi}{\mathrm{N}}\tan(\varphi)], \tag{A.19}$$

$$M_{51} = -\sin(\frac{\pi}{N}) - \tan(\varphi)[1 - \cos(\frac{\pi}{N})], \tag{A.20}$$

$$M_{52} = -l\sin(\frac{\pi}{N}) - [\rho_0 + l\tan(\varphi)][1 - \cos(\frac{\pi}{N})], \tag{A.21}$$

$$M_{56} = \frac{l + \frac{\pi}{N}\rho_0}{\gamma^2} - \frac{\pi}{N}\rho_0 + \rho_0\sin(\frac{\pi}{N}). \tag{A.22}$$

Let us assume that an off-momentum particle located at the center point of a drift has initial coordinates of $(x(0), 0, y(0), y'(0), z(0), \delta)^T$ at s=0 (see Figure A.1). It travels along the drift section of the deviated equilibrium orbit towards the bending magnet. The geometric relationship shown in Figure A.1 gives the bending radius of the off-momentum particle ρ_1 as

$$\rho_1 = \rho_0 + x(0) - AC = \rho_0 + x(0) - \frac{dl}{\tan(\frac{\pi}{N})} = \rho_0 + x(0) - \frac{x(0)\tan(\varphi)}{\tan(\frac{\pi}{N})}. \tag{A.23}$$

Since the bending radius of a particle with charge q and momentum p in a magnetic field with strength B is

$$\rho = \frac{p}{qB} \propto p, \tag{A.24}$$

then

$$\frac{\rho_1 - \rho_0}{\rho_0} = \frac{\Delta\rho}{\rho_0} = \frac{\Delta p}{p} = \delta, \tag{A.25}$$

$$\delta = \frac{x(0)}{\rho_0}[1 - \frac{\tan(\varphi)}{\tan(\frac{\pi}{N})}]. \tag{A.26}$$

According to Eq. (A.11), after traveling a half cell, the longitudinal coordinate of the off-momentum particle becomes

$$z = M_{51}x(0) + M_{52}x'(0) + z(0) + M_{56}\delta. \tag{A.27}$$

If the change of longitudinal coordinate z is 0, e.g.,

$$\Delta z = z - z(0) = M_{51}x(0) + M_{52}x'(0) + M_{56}\delta = 0, \tag{A.28}$$

then the ring will be isochronous. Since x′(0)=0, Eq. (A.28) reduces to

$$\Delta z = z - z(0) = M_{51}x(0) + M_{56}\delta = 0. \tag{A.29}$$

Substituting Eqs. (A.20), (A.22) and (A.26) into Eq. (A.29) gives the isochronous condition

$$\tan(\varphi) = \frac{l - (\gamma^2 - 1)\rho_0 \frac{\pi}{N}}{\gamma^2 \rho_0 + \frac{l - (\gamma^2 - 1)\rho_0 \frac{\pi}{N}}{\tan(\frac{\pi}{N})}}. \tag{A.30}$$

For the *non-relativistic* ions coasting in SIR ($\gamma \approx 1$), if we replace l by $L/2$, Eq. (A.30) reduces to

$$\tan(\varphi) = \frac{L/2}{\rho_0 + \frac{L/2}{\tan(\frac{\pi}{N})}}. \tag{A.31}$$

Eq. (A.31) is exactly the same as Eq. (B.7) of Ref. [12] which is derived directly using the isochronous condition Eq. (2.11) in Chapter 2.

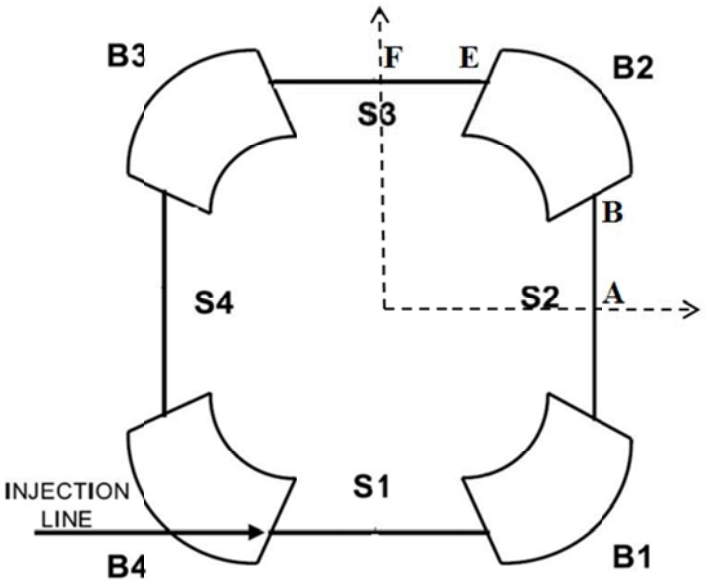

Figure A.2: Schematic of the SIR lattice.

The transfer matrix of a *full* single cell of the SIR lattice between points *A* and *F* (see Figure A.2) can be calculated by multiplication of transfer matrices as

$$M_{Cell} = M_{Drift} \bullet M_{Edge} \bullet M_{SBend} \bullet M_{Edge} \bullet M_{Dfift}. \tag{A.32}$$

For a 20 keV H_2^+ ion (γ=1.0000106264), with the ring lattice parameters (hard-edge model) listed in Table 2.1, e.g., L=0.79714 m, ρ_0=0.45 m, θ=90^o, φ=25.159^o, the transfer matrix of a single cell can be calculated numerically as

$$M_{Cell}=\begin{bmatrix} -2.220625 & 0.54927 & 0 & 0 & 0 & 1.03577 \\ -1.73198 & -0.220625 & 0 & 0 & 0 & 1.46969 \\ 0 & 0 & -0.262868 & 0.706585 & 0 & 0 \\ 0 & 0 & -1.31746 & -2.62868 & 0 & 0 \\ -1.46969 & -1.03577 & 0 & 0 & 1 & 1.24711 \\ 0 & 0 & 0 & 0 & 0 & 1 \end{bmatrix}. \quad \text{(A.33)}$$

For convenience, the upper-left four matrix elements in Eq. (A.33) can be defined as a 2×2 matrix for transfer of the vector $(x, x')^{\mathrm{T}}$ of an on-momentum particle

$$\begin{aligned} M_{Cell,(x,x')} &= \begin{bmatrix} m_{11} & m_{12} \\ m_{21} & m_{22} \end{bmatrix} = \begin{bmatrix} \cos\psi_x + \hat{\alpha}\sin\psi_x & \hat{\beta}\sin\psi_x \\ -\gamma\sin\psi_x & \cos\psi_x - \hat{\alpha}\sin\psi_x \end{bmatrix} \\ &= \begin{bmatrix} -2.220625 & 0.54927 \\ -1.73198 & -0.220625 \end{bmatrix}. \end{aligned} \quad \text{(A.34)}$$

Then the phase advance ψ_x, the Courant-Snyder parameters $\hat{\alpha}_x$, $\hat{\beta}_x$, and $\hat{\gamma}_x$ of the horizontal phase space at points A and F can be obtained easily as: ψ_x=1.79325, $\hat{\alpha}_{x,A} = \hat{\alpha}_{x,F} = 0$, $\hat{\beta}_{x,A} = \hat{\beta}_{x,F} = 0.563146$, $\hat{\gamma}_{x,A} = \hat{\gamma}_{x,F} = 1.775736$. Similarly, using the central four matrix elements in Eq. (A.33), the phase advance ψ_y, the Courant-Snyder parameters $\hat{\alpha}_y$, $\hat{\beta}_y$, and $\hat{\gamma}_y$ of the vertical phase space at points A and F are: ψ_y=1.77574, $\hat{\alpha}_{y,A} = \hat{\alpha}_{y,F} = 0$, $\hat{\beta}_{y,A} = \hat{\beta}_{y,F} = 0.72688$, $\hat{\gamma}_{y,A} = \hat{\gamma}_{y,F} = 1.38564$. The horizontal and vertical betatron tunes are $\nu_x = \frac{4\psi_x}{2\pi} \approx 1.142$, and $\nu_y = \frac{4\psi_y}{2\pi} \approx 1.169$, respectively, which are pretty close to the numerically simulated values of $\nu_x = 1.14$ and $\nu_y = 1.17$ in Table 2.1 (also in Ref. [12]).

Assuming s=0 at the starting point A, through piecewise tracking of the Courant-Snyder parameters using the formula,

$$\begin{pmatrix} \hat{\beta} \\ \hat{\alpha} \\ \hat{\gamma} \end{pmatrix} = \begin{bmatrix} m_{11}^2 & -2m_{11}m_{12} & m_{12}^2 \\ -m_{11}m_{21} & m_{11}m_{22}+m_{12}m_{21} & -m_{22}m_{12} \\ m_{21}^2 & -2m_{22}m_{21} & m_{22}^2 \end{bmatrix} \begin{pmatrix} \hat{\beta}_0 \\ \hat{\alpha}_0 \\ \hat{\gamma}_0 \end{pmatrix}, \tag{A.35}$$

where m_{11}, m_{12}, m_{21}, m_{22} correspond to the matrix elements in Eqs. (A.7), (A.8), and (A.9) for the different lattice elements, the horizontal betatron function of a *half* cell can be calculated as

$$\hat{\beta}_{x,\frac{1}{2}Cell}(s) = \begin{cases} a_1 + a_2 s^2, & 0 \le s \le L/2, \\ a_3 + a_4 \sin[a_5(s - L/2)], & L/2 \le s \le L/2 + \rho_0\pi/4, \end{cases} \tag{A.36}$$

where a_1=0.563147, a_2=1.775736, a_3=0.845237, a_4=0.715490, and a_5=4.444444. Similarly, the vertical betatron function of a *half* cell can be calculated as

$$\hat{\beta}_{y,\frac{1}{2}Cell}(s) = \begin{cases} b_1 + b_2 s^2 & 0 \le s \le L/2, \\ b_3 + b_4(s - L/2) + b_5(s - L/2)^2 & L/2 \le s \le L/2 + \rho_0\pi/4, \end{cases} \tag{A.37}$$

where b_1=0.72688, b_2=1.37574, b_3=0.945428, b_4=-1.130447, and b_5=1.3956406. The horizontal and vertical beta functions in the region of $L/2+\rho_0\pi/4 \le s \le L+\rho_0\pi/2$ can be obtained easily by mirror symmetry about $s=L/2+\rho_0\pi/4$.

The elements $M_{11,}M_{12}$, M_{16}, $M_{21,}M_{22}$, M_{26} of the single cell matrix M_{Cell} of Eq. (A.33) form a 3×3 transfer matrix for dispersion function $D(s)$

$$\begin{pmatrix} D \\ D' \\ 1 \end{pmatrix}_F = \begin{bmatrix} M_{11} & M_{12} & M_{16} \\ M_{21} & M_{22} & M_{26} \\ 0 & 0 & 1 \end{bmatrix} \begin{pmatrix} D \\ D' \\ 1 \end{pmatrix}_A. \tag{A.38}$$

Due to symmetry of lattice, we have

$$\begin{pmatrix} D \\ D' \\ 1 \end{pmatrix}_F = \begin{pmatrix} D \\ D' \\ 1 \end{pmatrix}_A, \quad \text{and} \quad D'_F = D'_A = 0. \tag{A.39}$$

From Eqs. (A.38) and (A.39), it is easy to obtain D_A=D_F=-M_{26}/M_{21}=0.84856. The piecewise tracking of the dispersion function $D(s)$ using the transfer matrices of the accelerator elements yields

$$D_{\frac{1}{2}Cell}(s) = \begin{cases} d_1, & 0 \le s \le L/2, \\ \rho_0 + d_2\{\cos[d_3(s-\frac{L}{2})] + \sin[d_3(s-\frac{L}{2})]\}, & L/2 \le s \le L/2 + \rho_0\pi/4, \end{cases} \tag{A.40}$$

where d_1=D_A=0.84856, d_2=0.39856, and d_3=2.22222. The dispersion function in the region of $L/2+\rho_0\pi/4 \le s \le L+\rho_0\pi/2$ can be obtained easily by mirror symmetry.

Figure A.3 illustrates the calculated optics functions v.s distance S of a single period of the SIR lattice by the above transfer matrix formalism. The calculated optics functions are very similar to the numerically simulated ones by DIMAD shown in Figure 2.3.

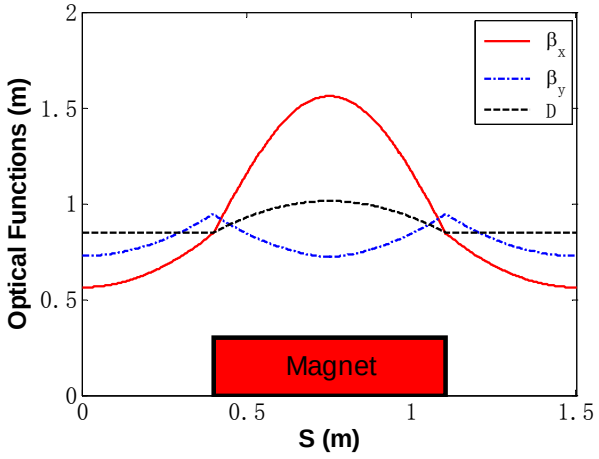

Figure A.3: Schematic of the optics functions v.s distance S of a single period of the SIR lattice calculated using transfer matrices.

Using Eqs. (2.5) and (A.40), the average value of dispersion function inside the bending magnets can be calculated as

$$< D(s) >_{bend} = \frac{1}{2\pi\rho_0}\int_{bend} D(s)ds = \frac{1}{\pi\rho_0 / 4}\int_{bend} D_{\frac{1}{2}Cell}(s)ds = 0.95746. \qquad (A.41)$$

Then Eq. (2.6) gives the momentum compaction factor

$$\alpha = \frac{< D(s) >_{bend}}{R} = \frac{< D(s) >_{bend}}{(4L + 2\pi\rho_0)/2\pi} \approx 0.9999868. \qquad (A.42)$$

Finally, the slip factor can be calculated as

$$\eta_0 = \alpha - \frac{1}{\gamma^2} \approx 8.06\times10^{-6}. \qquad (A.43)$$

In principle, the theoretical value of η_0 of the SIR lattice (hard-edge model) should be 0, the small deviation may originate from the rounding errors and neglect of the relativistic effects in the numerical calculation.

APPENDIX B

TRANSFER MATRIX USED IN CHAPTER 4 AND REF. [42]

The notations of the transfer matrix elements $R_{i,j}$ (i, j=1, 2,…6) adopted in Chapter 4 follow the ones used in Ref. [42], some of which are different from the standard ones $M_{i,j}$ defined in Appendix *A* of this dissertation. This section is devoted to the comparison of the two different notations between the two matrices.

B.1 Relations of R_{51}, R_{52} and R_{56} between two different matrices

According to Ref. [42], the equations of motion of an *ultra-relativistic* electron are:

$$\text{Radial (horizontal):} \qquad \frac{dx}{ds} = x', \quad \frac{dx'}{ds} = -k_x(s)x + \frac{\delta}{R(s)}, \tag{B.1}$$

$$\text{Longitudinal:} \qquad \frac{dz}{ds} = -\frac{x}{R(s)}, \qquad \frac{d\delta}{ds} = 0. \tag{B.2}$$

where $\delta=\Delta p/p$ is the fractional deviation of momentum. The general solution to the above equations is [42]:

$$x = D\delta + \sqrt{\hat{\beta}}\left(\frac{x_0}{\sqrt{\hat{\beta}_0}}\cos\psi + x_0'\sqrt{\hat{\beta}_0}\sin\psi\right), \tag{B.3}$$

$$x' = D'\delta - \frac{\hat{\alpha}}{\hat{\beta}}(x - Dp) - \frac{1}{\sqrt{\hat{\beta}}}\left(\frac{x_0}{\sqrt{\hat{\beta}_0}}\sin\psi - x_0'\sqrt{\hat{\beta}_0}\cos\psi\right), \tag{B.4}$$

$$z = z_0 + R_{56}\delta + R_{51}x_0 + R_{52}x_0'. \tag{B.5}$$

The transfer matrix elements R_{51}, R_{52}, R_{56} can be obtained from the above equations as

$$R_{56}(s) = -\int_0^s \frac{D(s')}{R(s')} ds', \tag{B.6}$$

$$R_{51}(s) = -\frac{1}{\sqrt{\hat{\beta}_0}} \int_0^s \frac{D(s')}{R(s')} \cos\psi(s') ds', \tag{B.7}$$

$$R_{52}(s) = -\sqrt{\hat{\beta}_0} \int_0^s \frac{\sqrt{\hat{\beta}(s')}}{R(s')} \sin\psi(s') ds', \tag{B.8}$$

where
$$\psi(s) = \int_0^s \frac{1}{\hat{\beta}(s')} ds'. \tag{B.9}$$

Ref. [42] defined a 2D Gaussian beam model with an initial equilibrium beam distribution function

$$f_0 = \frac{n_b}{2\pi\varepsilon_{x,0}} \exp[-\frac{x_0^{\ 2} + (\hat{\beta}_0 x_0')^2}{2\varepsilon_{x,0}\hat{\beta}_0}] g(\delta + \hat{u} z_0), \tag{B.10}$$

where
$$g(\delta) = \frac{1}{\sqrt{2\pi}\sigma_\delta} \exp(-\frac{\delta^2}{2\sigma_\delta^{\ 2}}), \tag{B.11}$$

and $\hat{u}$ is the chirp parameter which accounts for the correlation between z and δ.

(a) For transfer line

At s=0, for a transfer line, the initial values of the dispersion function and its derivative are $D(0)$=0, $D'(0)$=0, the phase advance $\psi(0)$=0. From Eqs. (B.3) and (B.4) we have

$$x(0) = x_0, \tag{B.12}$$

$$x'(0) = -x_0 \frac{\hat{\alpha}(0)}{\hat{\beta}(0)} + x_0'. \tag{B.13}$$

The standard transfer matrix $M(s)$ defined in Appendix A gives the transfer of z

$$z = z_0 + M_{56}\delta + M_{51}x(0) + M_{52}x'(0). \tag{B.14}$$

Plugging Eqs. (B.12) and (B.13) into Eq. (B.14) and comparing the coefficients of x_0, x_0', and δ with those of Eq. (B.5) yields the relation

$$R_{56}(s) = M_{56}(s), \quad R_{52}(s) = M_{52}(s), \quad R_{51}(s) = M_{51}(s) - M_{52}\hat{\alpha}(0)/\hat{\beta}(0). \tag{B.15}$$

The relation described in Eq. (B.15) repeats that clarified in the reference list of Ref. [42] for transfer lines.

(b) For storage rings

For the case of storage rings, though Ref. [42] did not explicitly address the difference and relation between the standard transfer matrix elements and the ones defined in that paper, it can be inferred from the formalism and context of the paper. We know that the beam dynamics of storage rings is different from that of the transfer lines. For example, the dispersion function $D(s)$ and its derivative $D'(s)$ of storage rings are periodic functions of s and must satisfy the close orbit condition, e.g., $D(s)=D(s+C_0)$, $D'(s)=D'(s+C_0)$, where C_0 is the ring circumference. Hence, $D(s)$ and $D'(s)$ of storage rings are self-consistent solutions of ring lattice optics required by the periodicity. While $D(s)$ and $D'(s)$ of transfer lines are free from the above restraint.

According to the smooth approximation adopted in Ref. [42] in the derivation of the 2D

dispersion relation (e.g., $\hat{\beta}=R/\nu_x$, $\psi=\nu_x s/R$, $D=R/\nu_x^2$, $\hat{\alpha}=0, D'=0$ and $\varepsilon_{x,0}=\sigma_x^2\nu_x/R$), at s=0, Eqs. (B.3) and (B.4) yield

$$x(0)=x_0+D\delta, \tag{B.16}$$

$$x'(0)=x_0'. \tag{B.17}$$

Eq. (B.16) indicates that x_0 is the initial betatron oscillation amplitude $x_\beta(0)$, which is not equal to the total initial radial offset $x(0)$, the latter includes a dispersion term $D\delta$. Consequently, the first exponential function defined in Eq. (B.10) describes the initial Gaussian distribution of the betatron oscillation amplitudes x_0 and slopes x_0', not $x(0)$ and slopes $x'(0)$; moreover, $\sigma_x=\sqrt{\varepsilon_{x,0}\hat{\beta}}=\sqrt{\varepsilon_{x,0}R/\nu_x}$ is the RMS beam radius which only includes the emittance effect, since the total RMS beam radius with dispersion effect should be $\sigma_{x,total}=\sqrt{\sigma_x^2+(D\sigma_\delta)^2}=\sqrt{\varepsilon_{x,0}R/\nu_x+\left(R\sigma_\delta/\nu_x^2\right)^2}$. Plugging Eqs. (B.16) and (B.17) into Eq. (B.14) and comparing the coefficients of x_0, x_0', and δ with those of Eq. (B.5) yields the relation of different matrix elements for storage rings

$$R_{56}(s)=M_{56}(s)+D(s)M_{51}(s),\quad R_{52}(s)=M_{52}(s),\quad R_{51}(s)=M_{51}(s). \tag{B.18}$$

B.2 One-turn transfer matrices by smooth approximation

By smooth approximation, the longitudinal and radial equations of motion of a particle in SIR can be written as

Radial (horizontal): $$\frac{d^2x}{ds^2}+\frac{\nu_x^2}{R^2}(s)x=\frac{\delta}{R(s)}, \tag{B.19}$$

Longitudinal:
$$\frac{dz}{ds} = -\frac{x}{R}, \qquad \frac{d\delta}{ds} = 0. \tag{B.20}$$

The solutions are

$$x(s) = x(0)\cos(\frac{\nu_x}{R}s) + x'(0)\frac{R}{\nu_x}\sin(\frac{\nu_x}{R}s) + \frac{R}{\nu_x^2}[1-\cos(\frac{\nu_x}{R}s)]\delta,$$

$$= x_0\cos(\frac{\nu_x}{R}s) + x_0'\frac{R}{\nu_x}\sin(\frac{\nu_x}{R}s) + \frac{R}{\nu_x^2}\delta, \tag{B.21}$$

$$x'(s) = -x(0)\frac{\nu_x}{R}\sin(\frac{\nu_x}{R}s) + x'(0)\cos(\frac{\nu_x}{R}s) + \frac{1}{\nu_x}\sin(\frac{\nu_x}{R}s)\delta,$$

$$= -x_0\frac{\nu_x}{R}\sin(\frac{\nu_x}{R}s) + x_0'\cos(\frac{\nu_x}{R}s), \tag{B.22}$$

$$z(s) = -x(0)\frac{1}{\nu_x}\sin(\frac{\nu_x}{R}s) - x'\frac{R}{\nu_x^2}[1-\cos(\frac{\nu_x}{R}s)] + [\frac{R}{\nu_x^3}\sin(\frac{\nu_x}{R}s) - (\frac{1}{\nu_x^2}-\frac{1}{\gamma^2})s]\delta,$$

$$= -x_0\frac{1}{\nu_x}\sin(\frac{\nu_x}{R}s) - x_0'\frac{R}{\nu_x^2}[1-\cos(\frac{\nu_x}{R}s)] - (\frac{1}{\nu_x^2}-\frac{1}{\gamma^2})s\delta, \tag{B.23}$$

From Eqs. (B.21)-(B.23), it is easy to obtain the *1-turn* standard transfer matrix $M_{1\text{-turn}}(s)$ and the non-standard one $R_{1\text{-turn}}(s)$ used in Ref. [42] and Chapter 4 of this dissertation as

$$M_{1\text{-turn}} = \begin{bmatrix} \cos(\frac{\nu_x}{R}s) & \frac{R}{\nu_x}\sin(\frac{\nu_x}{R}s) & 0 & 0 & 0 & \frac{R}{\nu_x^2} \\ -\frac{\nu_x}{R}\sin(\frac{\nu_x}{R}s) & \cos(\frac{\nu_x}{R}s) & 0 & 0 & 0 & \frac{1}{\nu_x}\sin(\frac{\nu_x}{R}s) \\ 0 & 0 & 1 & s & 0 & 0 \\ 0 & 0 & 0 & 1 & 0 & 0 \\ -\frac{1}{\nu_x}\sin(\frac{\nu_x}{R}s) & -\frac{R}{\nu_x^2}[1-\cos(\frac{\nu_x}{R}s)] & 0 & 0 & 1 & -(\frac{1}{\nu_x^2}-\frac{1}{\gamma^2})s + \frac{R}{\nu_x^3}\sin(\frac{\nu_x}{R}s) \\ 0 & 0 & 0 & 0 & 0 & 1 \end{bmatrix}, \tag{B.24}$$

and

$$R_{1-turn}=\begin{bmatrix} \cos(\frac{\nu_x}{R}s) & \frac{R}{\nu_x}\sin(\frac{\nu_x}{R}s) & 0 & 0 & 0 & \frac{R}{\nu_x^2}[1-\cos(\frac{\nu_2}{R}s)] \\ -\frac{\nu_x}{R}\sin(\frac{\nu_x}{R}s) & \cos(\frac{\nu_x}{R}s) & 0 & 0 & 0 & 0 \\ 0 & 0 & 1 & s & 0 & 0 \\ 0 & 0 & 0 & 1 & 0 & 0 \\ -\frac{1}{\nu_x}\sin(\frac{\nu_x}{R}s) & -\frac{R}{\nu_x^2}[1-\cos(\frac{\nu_x}{R}s)] & 0 & 0 & 1 & -(\frac{1}{\nu_x^2}-\frac{1}{\gamma^2})s \\ 0 & 0 & 0 & 0 & 0 & 1 \end{bmatrix}, \tag{B.25}$$

respectively.

According to Ref. [59, 62], the dispersion function $D(s)$ and its derivative $D'(s)$ can be obtained from the standard matrix Eq. (B.24) as

$$D(s)=\frac{M_{16}(1-M_{22})+M_{12}M_{26}}{2-M_{11}-M_{22}}=\frac{R}{\nu_x^2}, \tag{B.26}$$

$$D'(s)=\frac{M_{16}M_{21}+(1-M_{11})M_{26}}{2-M_{11}-M_{22}}=0. \tag{B.27}$$

From Eq. (A.1), the derivative $dz/d\delta$ can be calculated as [60]

$$\frac{dz}{d\delta}=\frac{\partial z}{\partial x(0)}\frac{dx(0)}{d\delta(0)}+\frac{\partial z}{\partial x'(0)}\frac{dx'(0)}{d\delta(0)}+\frac{\partial z}{\partial z(0)}\frac{dz(0)}{d\delta(0)}+\frac{\partial z}{\partial \delta(0)}$$

$$=M_{51}(s)D(s)+M_{52}(s)D'(s)+\frac{dz(0)}{d\delta(0)}+M_{56}(s). \tag{B.28}$$

Since $\delta=\delta(0)$, by moving the term $dz(0)/d\delta(0)$ of Eq. (B.28) to the left hand side, the conventional slip factor (evaluated along the equilibrium orbit neglecting betatron oscillation of trajectory) is [60]

$$\eta=-\frac{p}{C_0}\frac{d\Delta C}{dp}=-\frac{d(z-z(0))}{C_0 d\delta}$$

$$=\frac{1}{C_0}[M_{51}(s)D(s)+M_{52}(s)D'(s)+M_{56}(s)]. \tag{B.29}$$

It should be noted that Eq. (B.29) is a variant form of the original Eq. (6.22) in Ref.

[60], which is the expression for momentum faction factor α in the *ultra-relativistic* limit instead of slip factor η; in addition, there is no negative sign on the right hand side of Eq. (6.22) in Ref. [60], because Ref. [60] uses a different sign convention in definition of slip factor.

With Eqs. (B.24), (B.26) and (B.27) and (B.29), in the end, the slip factor for the one-turn matrix of a storage ring can be obtained as

$$\eta = \frac{1}{\nu_x^2} - \frac{1}{\gamma^2}. \tag{B.30}$$

While for the non-standard *1-turn* transfer matrix $R_{1\text{-}turn}$(s) in Eq. (B.25), the conventional slip factor (neglecting the betatron oscillation effect) is related to the matrix element $R_{56}(s)$ exclusively by

$$\eta = -\frac{R_{56}(s)}{C_0}\Big|_{s=C_0} = \frac{1}{\nu_x^2} - \frac{1}{\gamma^2}. \tag{B.31}$$

Particularly, in the case of isochronous rings, the radial (horizontal) tune ν_x in Eqs. (B.30) and (B.31) should be replaced by transition gamma γ_t.

BIBLIOGRAPHY

BIBLIOGRAPHY

[1] C. Rubbia, et al. “Conceptual design of a fast neutron operated high power energy amplifier” CERN/AT/95-44 (ET).

[2] R. Sheffield, “Utilization of accelerators for transmutation and energy production”, Proc. HB2010, Morschach, Switzerland (2010), p. 1–5.

[3] N. Pogue, et al, “A strong-focusing 800 MeV cyclotron for high-current applications”, AIP Conf. Proc. 1525, pp. 226-229; Application of accelerators in research and industry: Twenty-Second International Conference, Date: 5–10 August 2012, Location: Ft. Worth, TX, USA.

[4] L. Calabretta, et al, “A multi megawatt cyclotron complex to search for CP violation In the neutrino sector”, *Proceedings of CYCLOTRONS 2010*, Lanzhou, China, p. 298-303.

[5] R. J. Barlow, et al, “High power cyclotrons for the neutrino experiments DAEδALUS and ISODAR”. *Proceedings of IPAC2013*, Shanghai, China. p. 446-448.

[6] M. Seidel, “Cyclotrons for high-intensity beams”, CERN-2013-001, p. 17-32.

[7] T. Planche, et al, “Space charge effects in isochronous FFAGS and Cyclotrons”, *Proceedings of HB2012*, Beijing, China, p. 231-234.

[8] P. J. Bryant and K. Johnson, “*The principles of circulars accelerators and storage rings*” (Cambridge University Press, 1993).

[9] M. M. Gordon, *Proceedings of the 5th International conference on Cyclotrons*, Oxford, United Kingdom (1969), p. 305.

[10] A. J. Cerfon, J. P. Freidberg, F. I. Parra, T. A. Antaya, Physical Review Special Topics – Accelerators and Beams **16,** 024202 (2013).

[11] W. J. G. M. Kleeven and Y.K. Batygin, “Momentum analysis of space charge effects in an AVF cyclotron”, Particle Accelerators 24 (1989), p. 187.

[12] E. Pozdeyev, Ph.D. thesis, Michigan State University (2003).

[13] J. A. Rodriguez, Ph.D. thesis, Michigan State University (2004).

[14] E. Pozdeyev, J. A. Rodriguez, F. Marti, R. C. York, *Proceedings of Hadron Beam,* Nashville, Tennessee, U.S.A (2008), WGA30, p. 157.

[15] E. Pozdeyev, J. A. Rodriguez, F. Marti, R.C. York, Physical Review Special Topics – Accelerators and Beams **5**, 054202 (2009).

[16] Y. Bi, T. Zhang, C. Tang, Y. Huang, J. Yang, Journal of Applied Physics, **107**, 063304 (2010).

[17] A. Adelmann et al., "The OPAL (Object Oriented Parallel Accelerator Library) framework, users reference manual", Version 1.2.0, PSI report number PSI-PR-08-02, Paul Scherrer Institut (2008).

[18] J. J. Yang et al., "Beam dynamics in high intensity cyclotrons including neighboring bunch effects: Model, implementation, and application", Physical Review Special Topics – Accelerators and Beams **13**, 064201 (2010).

[19] Y. Li, G. Machicoane, F. Marti, T. P. Wangler, E. Pozdeyev, *Proceedings of the IEEE Particle Accelerator Conference* (Vancouver, Canada, 2009), TU3PBC06, p. 734.

[20] A. W. Chao, *Physics of Collective Beam Instabilities in High Energy Accelerators* (John Wiley & Sons, Inc., New York, 1993).

[21] D. A. Edwards, M. J. Syphers, *An Introduction to the Physics of High Energy Accelerators* (John Wiley & Sons, Inc., New York, 1993).

[22] Z. Huang, M. Borland, P. Emma, J. Wu, C. Limborg, G. Stupakov and J. Welch, Physical Review Special Topics – Accelerators and Beams **7**, 074401 (2004).

[23] J. Rosenzweig, C. Pellegrini, L. Serafini, C. Ternienden and G. Travish, TESLA FEL-Report 1996-15.

[24] M. Venturini, LBNL-63111, 2007.

[25] M. Venturini, Physical Review Special Topics – Accelerators and Beams **11**, 034401 (2008).

[26] J. Qiang, R. D. Ryne, M. Venturini, A. A. Zholents, I. V. Pogorelov, Physical Review Special Topics – Accelerators and Beams **12**, 100702 (2009).

[27] S. Humphries, *Charged Particle Beams* (John Wiley & Sons, Inc., New York, 1990), p. 704.

[28] A. M. Al-khateeb, O. Boine-Frankenheim, Ingo Hofmann, and G. Rumolo, Physical Review E **63**, 026503 (2001).

[29] L. Palumbo, V. G. Vaccaro, G. Wustefeld, IEEE Transactions on Nuclear Science, **31** (1984).

[30] W. R. Smythe, *Static and Dynamic Electricity* (McGraw-Hill Book Company Inc., New York, 1950), p. 85.

[31] C. E. Nelson and A. M. Sessler, Review of Scientific Instruments, 30(02), 1959, p. 80-89.

[32] K.Y. Ng, Particle Accelerators **16** (1984) 63.

[33] B. Zotter, ISR-TH/68-46, 1968.

[34] O. Gröbner and K. Hübner, CERN/ISR-TH-VA/75-27, 1975.

[35] A.V. Smirnov, Nuclear Instruments and Methods in Physics Research A **450** (2000), p. 579-582.

[36] N. Mounet and E. Métral, CERN-ATS-Note-2010-056 Tech, 2010.

[37] R. L. Gluckstern, J. van Zeijts, and B. Zotter, Physical Review E, **47** (1993), p. 656-663.

[38] R. Warnock and R. Ruth, Physical Review Special Topics – Accelerators and Beams **8**, 014402 (2005).

[39] See e.g., J. N. Reddy, *An Introduction to the Finite Element Method* (3rd edition, McGraw-Hill Higher Education, 2006).

[40] X. Lin，Z. Zhang，*Solved Problems in Electrodynamics* (in Chinese), Science Press, Beijing, ISBN 7030071298 (2002), p. 72.

[41] D. Ratner, Ph.D. thesis, Stanford University (2011).

[42] S. Heifets, G. Stupakov, and S. Krinsky, Physical Review Special Topics–

Accelerators and Beams **5**, 064401 (2002).

[43] T. J. M. Boyd, J.J. Sanderson, *The Physics of Plasmas* (Cambridge University Press, Cambridge, 2003), p. 256-260.

[44] P. M. Bellan, *Fundamentals of Plasma Physics* (Cambridge University Press, New York, 2006), p. 182-192.

[45] N. A. Krall, A. W. Trivelpiece, *Principles of Plasma Physics* (McGraw-Hill, Inc., New York, 1973), p. 375-380.

[46] C. N. Lashmore-Davies, CERN-81-13, 1981, p. 30-38.

[47] M. Reiser, *Theory and Design of Charged Particle Beams* (Wiley-VCH Verlag GmbH & Co. KGaA, Weinheim, 2008), p. 190-192.

[48] J. A. Simpson, Review of Scientific Instruments, **32**, 1283 (1961).

[49] E. R. Cawthron, D. L. Cotterell, and M. Oliphant, *Proceedings of the Royal Society of London* A **314**, 39-51, (1969).

[50] Y. Zou, Y. Cui, I. Haber, M. Reiser, and P. G. O'Shea, Physical Review Special Topics-Accelerators and Beams, **6**, 112801 (2003).

[51] Y. Zou, Y. Cui, V. Yun, A. Valfells, R. A. Kishek, S. Bernal, I. Haber, M. Reiser, and P. G. O'Shea, Physical Review Special Topics-Accelerators and Beams, **5**, 000000 (2002).

[52] Y. Cui, Y. Zou, A. Valfells, M. Reiser, M. Walter, I. Haber, R. A. Kishek, S. Bernal, and P. G. O'Shea, Review of Scientific Instruments **75,** Number 8 (2004).

[53] SIMION, Scientific Instrument Services, Inc, http://simion.com/.

[54] Lua, http://www.lua.org/.

[55] G. Machicoane, D. Cole, J. Ottarson, J. Stetson, and P. Zavodszky, Review of Scientific Instruments **77**, 03A322 (2006).

[56] H. Hamma, H. Tanaka, N. Kumagai, M. Kawai, F. Hinode, T. Muto, K. Nanbu, T. Tanaka, K. Kasamsook, K. Akiyama, and M. Yasuda, New Journal of Physics **8** (2006), p. 292.

[57] Y. Bi, et al, "Towards quantitative simulations of high power proton cyclotrons", Physical Review Special Topics – Accelerators and Beams **13**, 054402 (2011).

[58] K. R. Crandall and D. P. Rusthoi, TRACE 3-D Documentation, 3rd edition, LA-UR-97-886, (1997).

[59] M. Conte and W. W. MacKay, *An Introduction to the Physics of Particle Accelerators* (2nd edition, World Scientific Co. Pte. Ltd, Singapore, 2008).

[60] W. W. MacKay and M. Conte, *Accelerator Physics-Example Problems with Solutions* (World Scientific Co. Pte. Ltd, Singapore, 2012).

[61] K. L. Brown, SLAC-Report-75, 1982.

[62] S. Y. Lee, *Accelerator Physics* (2nd Edition, World Scientific Co. Pte. Ltd, Singapore, 2004).